Measurement of the W Boson Transverse Momentum Distribution in 1.8 TeV Proton-Antiproton Collisions

Hiroyuki MINATO

A dissertation submitted to the Doctoral Program
in Physics, the University of Tsukuba
in partial fulfillment of the requirements for the
degree of Doctor of Philosophy (Science)

January, 1999

Abstract

We have measured the W boson transverse momentum (P_T^W) distribution in proton-antiproton collisions at a center-of-mass energy of 1.8 TeV using the Collider Detector at Fermilab (CDF).

The production of the W boson with subsequent decay into an electron and a neutrino in the proton-antiproton collisions provides good tests of the perturbative QCD theory because the event signature is clean. About 90% of the W bosons are produced with $P_T < 20$ GeV/c where soft gluon emission is the dominant contribution. In this region, the fixed-order perturbative calculation breaks down and the gluon resummation is needed for the perturbative QCD calculation. There are two techniques for the gluon resummation calculation. One technique is based on the b-space formalism where b is the impact parameter, which is Fourier conjugate to the P_T. The other is a new technique which allows us to calculate the gluon resummation directly in P_T space. Both formalisms are compared to the CDF data in this study. The next-to-leading order (NLO) calculation is also tested in the range of P_T^W above $\sim$ 80 GeV/c in this study.

In the 110 pb^{-1} of CDF data collected during the 1992–1995 run (Run I), we select W candidates by looking for an isolated high transverse momentum electron and large missing transverse energy, which corresponds to the transverse momentum of the neutrino (P_T^ν). We identify electrons using the CDF central electromagnetic calorimeter and the central tracking chamber which cover the pseudorapidity range from -1.1 to 1.1. We obtain 62165 $W \to e\nu$ candidates. We expect some residual backgrounds from QCD multijet events in the W candidate events. We estimate the size and shape of these background events using independent QCD multijet samples. We find that the

QCD multijet background events are less than 1% of the W candidate events. The fractions of backgrounds from processes such as $W \to \tau\nu \to e\nu\nu\nu$ and $Z \to ee$ in the candidates are determined as a function of P_T^W using a Monte Carlo event generator. The former has both an isolated electron and a missing transverse energy while the latter can survive the selection cut if one leg of Z electrons or a jet escapes from the detector undetected. A mismeasurement of energy of an electron or a jet can also cause large missing transverse energy. We find that the fraction of the backgrounds from $W \to \tau\nu$ and $Z \to ee$ events is $\sim$3% for $P_T^W < 50$ GeV/c and $\sim$15% for $P_T^W > 140$ GeV/c.

We measure the net transverse momentum of all other particles recoiling against a W boson. In a perfect detector, the transverse momentum of the recoil (P_T^{rec}) should balance P_T^W. We estimate the detector resolution on the P_T^{rec} distribution using the $Z \to ee$ events as a control sample. We determine the P_T^{rec} resolution as a function of P_T^W by comparing the distributions of P_T^{ee} and P_T^{rec} in Z events.

In order to compare the data with the theoretical prediction, the theory curves are re-shaped according to the boson backgrounds, the detector resolution, and the detector acceptance. The last item is studied using a Monte Carlo event generator. We find that the NLO plus gluon resummation calculation provides reasonable description of the data in the range $P_T^W \lesssim 120$ GeV/c and that there appears to be a discrepancy at high P_T^W ($120 \lesssim P_T^W \lesssim 200$ GeV/c), though the experimental errors are large.

Acknowledgements

I would like to express my appreciation to Professor Koji Takikawa, my thesis advisor and the representative of the Japanese CDF collaboration, for his guidance and encouragements throughout my graduate career. He has provided me with wonderful surroundings for the study.

I would like to thank Professor Kunitaka Kondo, our former representative, for giving me the opportunity to join the CDF collaboration and for his continuous support.

I would like to thank Professor Shinghong Kim for his constant support and criticisms to the points.

I would like to express my appreciation to Dr. Bob Wagner for his greatest support. He gave me a lot of suggestions throughout this study. His door has been always open to me. I could not finish my study without his encouragement.

Professor Young-Kee Kim is appreciated for her support. It was she who guided me to this study. She gave me a lot of suggestions when I started this study.

I would like to thank Dr. Mark Lancaster for his suggestions. In particular, he gave me information to learn theoretical works.

Dr. Dan Cronin-Hennessy let me use his programs for missing energy calculation. His Ph.D thesis and internal papers guided me to progress my study.

I would like to thank all EWK group members. I enjoyed working as a member of the Test Beam Group and Plug Upgrade Group, I am grateful to Drs. Mike Albrow, Giorgio Apollinari, Yasuo Fukui, Junsuke Iwai, and Willis Sakumoto (He also gave me help in the W study).

Dr. Makoto Shimojima is another EWK member at Tsukuba. He has very readily offered a lot of helpful advice. I am thankful for his advice on W boson analysis, programming, English writing, etc. In particular, I appreciate his reading the entire text in its original form and giving great comments.

Professors Kiyoshi Yasuoka and Yoshihiro Seiya have given me a lot of advice. I had frequently been to their office for advice. I am very thankful to them.

Professors Itsuo Nakano and Kazuhiro Hara has taught me the basics in physics experiments.

Discussions on physics and other various things with Shin Aota, Hirofumi Ikeda, and all Japanese graduate students at Fermilab, were very beneficial for me.

I thank the Fermilab staffs and the technical staffs of the participating institutions for their vital contributions. I thank many CDF collaborators who have developed the detector and other analysis environment.

I wish to thank Carol Picciolo, Kyoko Kunori, Kazuko Kumashiro and Mutsumi Uenishi for their help through their secretary works.

I wish to express my thanks to the friends from Aikido. Their friendship has kept me sane.

Finally, I want to express my great appreciation to my parents, for their help and support.

This work was supported by the Ministry of Education, Science and Culture of Japan; the U.S. Department of Energy and National Science Foundation; the Italian Istituto Nazionale di Fisica Nucleare; the Natural Sciences and Engineering Research Council of Canada; the National Science Council of the Republic of China; and the A.P. Sloan Foundation.

Contents

List of Figures

List of Tables

Chapter 1

Introduction

The Standard Model has successfully described many phenomena in high energy particle physics. In the framework of the Standard Model, interactions between quarks and leptons are described by exchanges of gauge bosons. In the Electroweak Model (EW), $W^{\pm}$, Z^0, and γ mediate the electroweak force between quarks and leptons while in the Quantum Chromodynamics (QCD), it is the gluons that mediate the strong force between quarks.

During the last decade, the Collider Detector at Fermilab (CDF) group has been measuring various physics processes in hadron-hadron collisions at the Tevatron collider, where all of the results showed qualitative agreement with the Standard Model predictions. The W/Z boson production in the hadron collider provides us with good tests of the QCD because of their heavy masses and clean signatures. For example, the cross section of $W +$ jets events was measured precisely and compared with the perturbative QCD; the result is consistent with the theoretical prediction[1]. The measurement of W transverse momentum (P_T) also allows us to test the perturbative QCD. At the Tevatron energy (the center-of-mass energy 1.8 TeV), about ninety percent of the production cross section of the W bosons is in the small P_T region, where $P_T < 20$ GeV/c. In this region, the effect of soft gluon emission is a key issue and thus the gluon resummation calculation is needed in the QCD calculation. By measuring the P_T distribution of the W boson we can test how well the gluon resummation calculation reproduces the reality. The leptonic decay modes of the W boson (e.g., $W \to e\nu$) are very clean and we expect very little background events. Since we have more than 60000 $W \to e\nu$ candidate events, we can also test the fixed-order perturbative calculation in the high P_T region ($P_T > 80$ GeV/c).

1.1 Transverse Momentum Distribution of W Boson

In QCD a W boson acquires transverse momentum by recoiling against one or more partons [2]. Most W bosons are produced with relatively small transverse momentum, *i.e.* $P_T < M_W$, but some are produced with quite large P_T. The relevant mechanisms are the 2→2 processes $q\bar{q} \to Wg$ and $qg \to Wq$. The next-to-leading order (NLO) perturbative corrections, obtained from real emission processes like $q\bar{q} \to Wgg$ and virtual (loop) corrections to the leading-order processes have been calculated [3]. Some examples of Feynman diagrams contributing to W production are shown in Fig. 1.1. The conventional theoretical cross section mentioned above, however, breaks down in low P_T region.

The leading behavior at small P_T comes from the emission of a soft gluon in the process $q\bar{q} \to Wg$. At very small P_T, the intrinsic transverse motion of the quarks and gluons inside the colliding hadrons (k_T) can not be neglected. This non-perturbative contribution has to be combined with the perturbative large P_T.

For $P_T \gg \langle k_T \rangle$ ($\sim$ 760 MeV [2]) a purely perturbative approach is adequate. However, if at the same time $P_T \ll M_W$, higher-order terms in the perturbation series can not be neglected. In particular, the emission of multiple soft gluons becomes important and the leading contributions at each order have the form[2]

$$\frac{1}{\sigma}\frac{d\sigma}{dP_T^2} \simeq \frac{1}{P_T^2}\sum_{j=1}^{\infty} L_j \ , \tag{1.1}$$

$$L_j = A_j \alpha_S^j \ln^{2j-1}\frac{M_W^2}{P_T^2} \tag{1.2}$$

where the A_i are calculable coefficients of order unity and α_S is the QCD coupling constant. In low P_T region ($P_T < 10$–15 GeV/c), L_j terms do not converge so Eq. 1.1 can not be evaluated directly.

The coefficients A_j, however, are not independent and it is possible to resum the series even when L_j is large. This resummation was carried out by Collins and Soper [4, 5] in b-space[1] (b-space formalism):

$$\frac{d\sigma}{dP_T^2 dy} \sim \int_0^{\infty} d^2b\, e^{i\vec{P_T}\cdot\vec{b}} exp\left(-S\left(M_W, b, C_1, C_2\right)\right)\tilde{W}\left(b\right) \ , \tag{1.3}$$

$$S\left(M_W, b, C_1, C_2\right) = \int_{C_1^2/b^2}^{C_2^2/b^2} \frac{d\mu^2}{\mu^2}\left[\ln\left(\frac{C_2^2 M_W^2}{\mu^2}\right)\sum_{j=1}^{\infty} A_j\alpha_S^j\left(\mu\right) + \sum_{j=1}^{\infty} B_j\alpha_S^j\left(\mu\right)\right], \tag{1.4}$$

where the function $\tilde{W}$ is related to a parton distribution, y is the rapidity of W boson. The parameters C_1, C_2 are arbitrary numbers, and the A_j and B_j are calculable coefficients. The above resummation should match with the result of the fixed-order perturbative calculation at large P_T ($\sim M_W$), which was studied by Arnold and Kauffman[6]. In practice, however, a non-perturbative cut-off must be included to make the b integral in Eq. 1.3 converge at large b and to avoid infra-red problems from evaluating α_S and the parton distribution at low scales. Ladinsky and Yuan introduced a non-perturbative form which has parameters determined from experiments[7].

A new technique of the resummation was proposed by Ellis and Veseli in 1998[8]; they perform the resummation directly in q_T-space[2]. We also compare their result to our data.

[1] b is the impact parameter and is Fourier conjugate to the P_T.

[2] In theoretical papers, the transverse momentum is denoted by q_T.

The non-perturbative parts of both formalisms are in the region $P_T \lesssim 5$ GeV/c, where they are very sensitive to the parameters chosen. Theoretical curves by the b-space and q_T-space formalisms are shown in Fig. 1.2. We use the MRS-R2 parton distribution functions [9].

1.2 Previous Measurements

The transverse momentum of W bosons has been measured previously by the UA1 [10], UA2 [11], CDF [12], and DØ [13] collaborations. The UA1 and UA2 collected the data by CERN Sp$\bar{\text{p}}$S collider at $\sqrt{s} = 630$ GeV. The CDF and DØ used the Tevatron accelerator with $\sqrt{s} = 1.8$ TeV. The CDF presented the result using the data collected during the 1988–1989 run. The three results by the UA1, UA2, and CDF reported that they are in agreement with the NLO QCD prediction, but their data samples were small. In 1998, the DØ reported their result whose data came from a sample of about 12 pb^{-1} collected during the 1992–1993 run. Their data are also small in large P_T range ($\sim$ 20 events $P_T > 80$ GeV/c) and the result is in agreement with the b-space formalism prediction.

1.3 Outline of the Thesis

In this thesis we present the result of the measurement of the W boson transverse momentum distribution in proton-antiproton collisions at a center-of-mass energy $\sqrt{s} = 1.8$ TeV. The data were accumulated using the CDF detector. The total integrated luminosity was 110 pb^{-1} during 1992–1995 run. The components of the CDF detector relevant to this analysis are described in Chapter 2. In Chapter 3, we describe the criteria for selecting W events which decay into electrons and neutrinos. Energy corrections for recoil energy are described in Chapter 4. Since we can not measure energy of neutrinos, we measure the recoil transverse momentum distribution in the

W events. Chapter 5 describes how we estimate background events which remain in the data sample. There are two types of the background events: one is QCD multijet events, the other is W decaying into $\tau\ (\rightarrow e\nu\nu)\ \nu$ and Z decaying into ee. Since neither can be removed event by event, total number of events or ratio to the data are estimated. In Chapter 6, we estimate the detector acceptance using Monte Carlo samples. We estimate the detector resolution using $Z \rightarrow ee$ events as a control sample in Chapter 7. The data is compared to the theoretical predictions which are smeared due to the detector resolution in Chapter 8. Finally we conclude in Chapter 9.

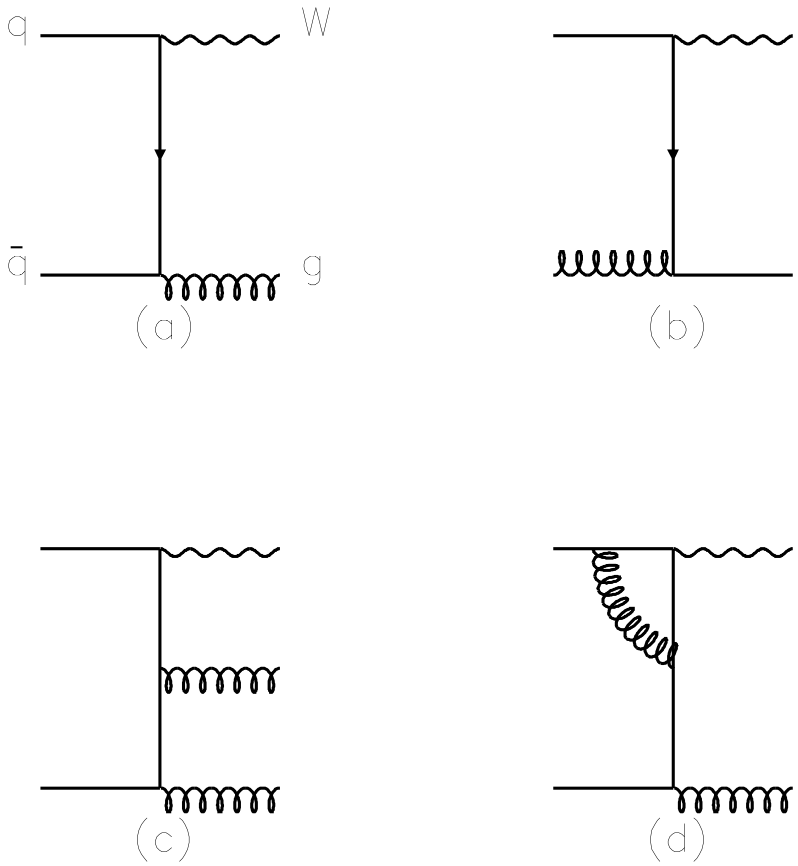

Figure 1.1: Some examples of Feynman diagrams contributing to W production at non-zero P_T; (a,d) $q\bar{q} \to Wg$, (b)$qg \to Wq$, (c) $q\bar{q} \to Wgg$.

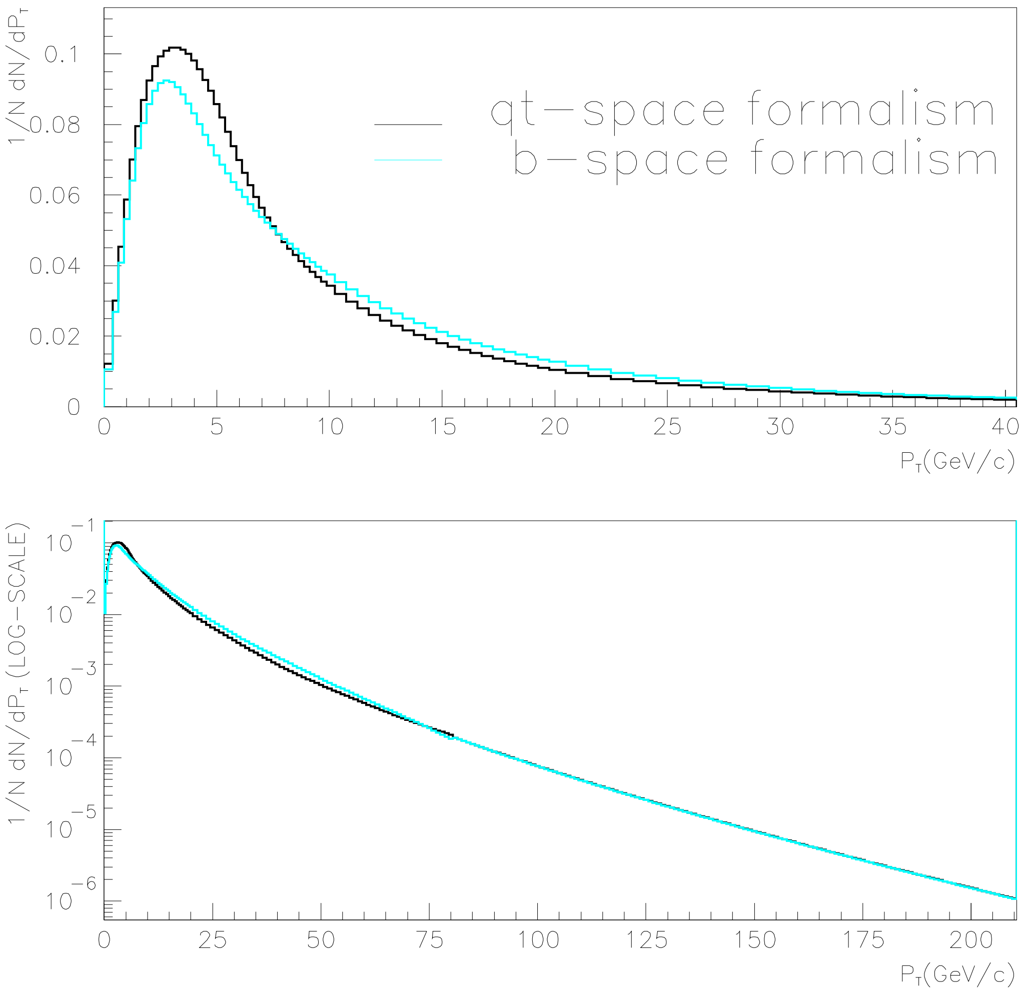

Figure 1.2: Theoretical predictions by the b-space formalism and q_T-space formalism. Both predictions are calculated by the same program. PDF is MRS-R2. The parameters used here are given in [7] (the b-space formalism) and [8] (the q_T-space formalism).

Chapter 2

The Experimental Apparatus

The Collider Detector at Fermilab (CDF) is located at the B0 collision hall in the Fermi National Accelerator Laboratory (FNAL) in Illinois, USA. The CDF detector is a general purpose detector, designed for precision measurements of energy, momentum, and position of particles produced by colliding Tevatron beams. The Tevatron synchrotron accelerator provides the world's highest energy proton-antiproton collisions at a center-of-mass energy of 1.8 TeV.

2.1 The Accelerator

The system of accelerators at FNAL consists of several parts as shown in Fig. 2.1.

The beam is created as ionized hydrogens; in the Cockcroft-Walton, electrons are added to H atoms to form ions. These H^- ions are accelerated to an energy of 750 keV and sent to the next stage, the Linac.

The Linac, a linear accelerator, accelerates H^- ions to 400 MeV. Before entering the third stage, the Booster, the ions pass through a carbon foil which removes the electrons, leaving only the protons.

The Booster is a rapid cycling synchrotron, 151 m in diameter. The protons travel around the Booster about 20,000 times and their energy is raised to 8 GeV.

The next stage is the Main Ring which is a synchrotron accelerator 2 km in diameter. The Main Ring has a dual purpose: it is used to accelerate protons and antiprotons to 150 GeV before the next acceleration by the Tevatron, and it is used to accelerate protons to 120 GeV for the production of antiprotons.

In order to create antiprotons, the protons with an energy of 120 GeV are transported to a target area, and focused on a nickel target. The collisions in the target produce a wide range of secondary particles including many antiprotons. The antiprotons with an energy of about 8 GeV are collected, focused, and transported to the Debuncher ring, where they are debunched and then stochastically cooled. Before these antiprotons are injected into the Main Ring, they are stored in the Accumulator.

The protons and antiprotons with an energy of 150 GeV are finally injected into the Tevatron synchrotron, located directly below the Main Ring. The Tevatron accelerates the protons and antiprotons to their final energy of 900 GeV in the 5.7 T magnetic field of superconducting dipole magnets.

There are 6 bunches of protons and 6 bunches of antiprotons in the Tevatron. The number of particles in a proton bunch is $N_p \sim 2 \times 10^{11}$, while in an antiproton bunch it is $N_{\bar{p}} \sim 6 \times 10^{10}$. A crossing of a proton bunch and an antiproton bunch occurs every 3.5 μs. The quadrupole magnets focus the proton and the antiproton beams to a diameter of ~ 40 μm at the B0 and D0 collision halls, and electrostatic separators prevent collisions at other points during normal running. The bunch length (rms) is ~ 60 cm. The luminosity in the Tevatron is given by the expression:

$$L = \frac{f B N_p N_{\bar{p}}}{4\pi\sigma^2} F\left(\sigma_l/\beta^*\right) \tag{2.1}$$

where f is the revolution frequency, B is the number of bunches in each beam, N_p ($N_{\bar{p}}$) is the number of protons (antiprotons) in a bunch, σ is the beam size at the interaction point, and F is a form factor that depends on the ratio of the bunch length, σ_l, to the beta function at the interaction point, β^*. A typical luminosity at the beginning of a store is $\sim 1.6 \times 10^{31}$ cm^{-2}sec^{-1}.

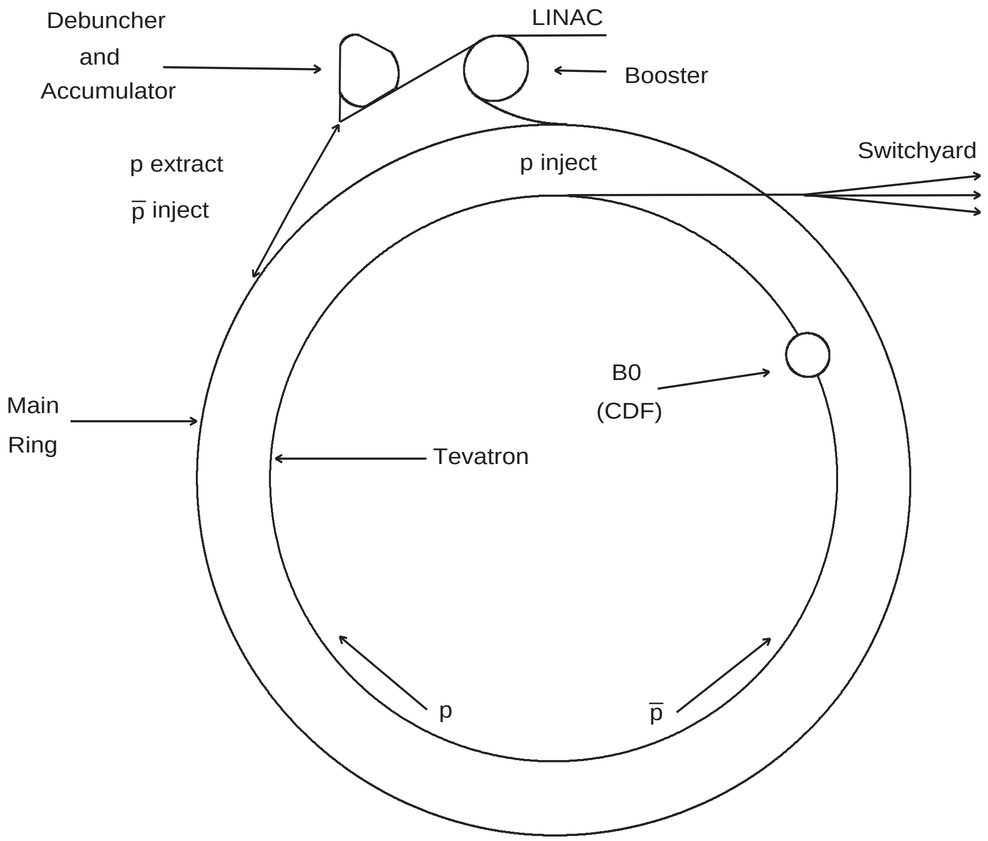

Figure 2.1: Schematic of the Tevatron. The Tevatron is actually the same diameter as the Main Ring but is shown as smaller in the diagram.

2.2 The CDF Detector

The CDF detector is designed for multi purpose and consists of tracking detectors, calorimeters, and muon detectors. The coordinate system of the CDF is defined by a cylindrical system with the z axis along the beamline (the positive z direction is the proton beam direction) , the azimuthal angle,

ϕ, and the polar angle θ (Fig. 2.2). Instead of θ, we use a quantity called pseudorapidity, η, defined by:

$$\eta \equiv -ln\left(tan\frac{\theta}{2}\right) \quad . \tag{2.2}$$

which approximates to the rapidity y ($= \frac{1}{2}ln\left(\frac{E+p_z}{E-p_z}\right)$) for $p \gg m$, where E, p, and m are a particle's energy, momentum, and mass. The pseudorapidity is a convenient variable to use in describing particle collisions in hadron colliders, because the difference in η ($\Delta\eta$) is invariant under Lorentz boost along the z-axis, the boost which is unavoidable in $p\bar{p}$ collisions. The detector is symmetric in ϕ and η. An overview of the components of the detector used in this analysis are described below. A full description of the detector can be found in [14]. Fig. 2.3 shows schematic views of the CDF detector.

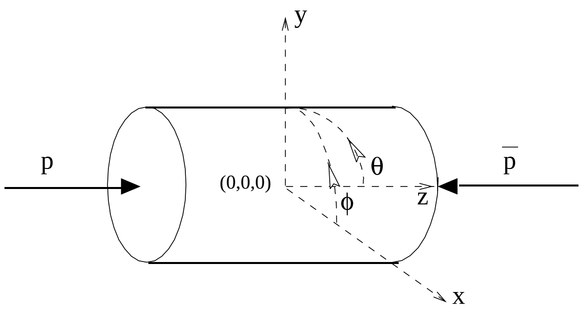

Figure 2.2: The CDF coordinate system

2.2.1 The Central Tracking Chamber

The Central Tracking Chamber (CTC) is a 1.3 m radius, 3.2 m long cylindrical drift chamber which gives precise momentum measurements in the angular region -1.1 $< \eta <$ 1.1. The CTC is surrounded by a superconducting solenoid producing a 1.4 T magnetic field, which allows the precise momentum analysis of charged particles. The chamber contains 84 layers of sense wires grouped into 9 "superlayers". Five of the superlayers consist of 12 axial sense wires; four stereo superlayers consist of 6 sense wires tilted by $\pm 3°$

relative to the beam direction. Fig. 2.4 shows an endplate of the chamber displaying the 45° tilt of the superlayers to the radial direction to correct for the Lorentz angle of the electron drift in the magnetic field. Tracking information in the r-ϕ space is given by the 9 superlayers and the r-z view is provided by the stereo superlayers. The resolution for momentum measurements is a function of the curvature of the track and thus of the transverse momentum of the charged particle, p_T (GeV/c) :

$$\frac{\delta p_T}{p_T} < 0.002 \cdot p_T \quad . \tag{2.3}$$

2.2.2 The Vertex Time Projection Chamber

The vertex time projection chamber (VTX) is located inside the CTC. The VTX is used to reconstruct the z position of $p\bar{p}$ interactions along the beam line. The VTX consists of 28 time projection chamber modules along the z direction and has a good track reconstruction capability in r-z plane. The resolution of the z vertex measurement is about 3 mm.

2.2.3 The Calorimeters

The calorimeters are arranged in towers which project back to the geometric center. The calorimeters, the electromagnetic (EM) calorimeters and the hadronic calorimeters, are divided into the central, plug, and forward regions. The segmentation and coverage of the calorimeters are shown in Fig. 2.5. The calorimeters utilize lead as an absorber for the EM sections and iron for the hadronic sections. The active sampling medium is either scintillator in the central region, or gas proportional chambers in the plug and the forward regions.

The Central Electromagnetic Calorimeter

The central electromagnetic calorimeter (CEM) covers the region $|\eta| < 1.1$. The CEM consists of 48 "wedge" modules. A modules has 10 towers, each of which covers 15° in ϕ and 0.1 in η (Fig. 2.6). The CEM has 31 scintillator layers and 30 lead layers, corresponding to a total amount of materials of 16 radiation lengths (X_0). A typical size of a tower cell is 46 cm in the ϕ direction and 24 cm along the beam direction z. This is larger than the typical size of electromagnetic showers, which is only a few cm's wide laterally. The light from each tower is collected by sheets of acrylic wavelength shifter at both azimuthal tower boundaries and guided to two photomultiplier tubes per tower. The energy resolution of the CEM is

$$\frac{\delta E}{E} = \frac{0.135}{\sqrt{E \cdot sin\theta}} \tag{2.4}$$

where E is in GeV.

The central electromagnetic strip chamber (CES) is located at a depth of 5.9 X_0 (including the coil) to help identify electrons via energy shower profile as well as better position resolution. The CES is a multi-wire gas proportional chamber with anode wires (64 channels / module) along the beam direction for the r-ϕ view of the showers and cathode strips (128 channels / module) perpendicular to the wires for z view. The position resolution of a few mm's is achieved for electromagnetic showers. We use the local coordinates in the CES module to define the fiducial volume of each CES module. A schematic drawing of the CES local coordinate is shown in Fig. 2.7

The Plug and Forward Electromagnetic Calorimeters

Two modules of the end plug electromagnetic calorimeter (PEM) are located at both ends of the CTC and covers $1.1 < |\eta| < 2.4$. Each of the modules consists of four quadrants of $\triangle\phi = 90°$ each, and each of the quadrants consists of 34 layers of proportional tube arrays interleaved with 2.7 mm thick lead absorber panels (Fig. 2.8). Cathode strips outside the plastic tube arrays have a tower segmentation of $\triangle\eta \times \triangle\phi = 0.1 \times 5°$. Ten layers have ϕ or θ strips ($\Delta\eta \times \Delta\phi = 0.01 \times 1°$) for position and shower shape determination.

The coverage of these strips in polar angle is limited to the region of η =1.2 – 1.84. The PEM has an energy resolution of $\delta E_T/E_T = 0.28/\sqrt{E_T}$ where E_T is measured in GeV.

Two modules of the forward electromagnetic calorimeter (FEM) are located approximately 6.5 m from the interaction point and enclose the beam pipe at either end of the CDF. Each calorimeter consists of 30 sampling layers, each of which is composed of lead sheets and chambers of gas proportional tubes with cathode and readout. Each cathode pad subtends 0.1 units of η and 5° of ϕ. The FEM covers $2.2 < |\eta| < 4.2$ and has an energy resolution of $\delta E_T/E_T = 0.25/\sqrt{E_T}$ where E_T is in GeV.

The Hadron Calorimeters

The central and endwall hadron calorimeters (CHA, WHA) are steel-scintillator sandwich calorimeters. The CHA covers $|\eta| < 0.9$ and the WHA covers $0.7 < |\eta| < 1.3$. The CHA and WHA consist of 48 layers and are divided into projective towers, each covering 0.1 in η and 15° in ϕ, matching those of the CEM which is in front of them.

The end plug hadron calorimeters (PHA) cover the region $1.3 < |\eta| < 2.4$, while the the forward hadron calorimeters (FHA) cover $2.3 < |\eta| < 4.2$. The calorimeters are composed of proportional tube chambers and steel plates.

The energy resolutions of the CHA/WHA, PHA, and FHA are ($\delta E_T/E_T =$) $0.8/\sqrt{E_T}$, $1.3/\sqrt{E_T}$, and $1.41/\sqrt{E_T}$.

2.2.4 Beam-Beam Counters

There is a plane of scintillation counters on the front face of each of the forward and the backward calorimeters. These scintillators, called the beam-beam counters (BBC), provide a “minimum-bias” trigger for the detector, and are also used as the primary luminosity monitor. The counters are arranged in a rectangle around the beam pipe. They cover the range of 3.24

to 5.90 in η. The minimum bias trigger requires at least one counter in each plane to fire within a 15 ns window centered on the beam crossing time.

2.2.5 The Trigger System

The CDF trigger system consists of three levels. The idea of the multi-level trigger structure is to introduce as little bias as possible at the lower levels, with the goal of reducing the rate to a point where the next level can do a more sophisticated analysis without incurring significant deadtime. The first two, Level 1 and Level 2 triggers are hardware triggers, and the Level 3 trigger is a software trigger running on UNIX machines. Triggers relevant to this analysis are described below.

The Level 1 decision is made in the 3.5 μsec window between beam crossings and it therefore incurs no deadtime. Both hadron and electromagnetic calorimeter towers are summed into trigger towers with a width of $\Delta\eta \times \Delta\phi$ of $0.2{\times}15°$. This results in a representation of the entire detector as a 42 (in η) by 24 (in ϕ) array for both the electromagnetic and hadronic calorimeters. An event need only pass one of the individual Level 1 triggers. The Level 1 calorimeter trigger requires a minimum transverse energy ($E sin\theta$) of 8 GeV in a CEM trigger tower.

Events which pass the Level 1 triggers are considered in the Level 2 hardware. At this level, clusters of energy are formed by the hardware "cluster finder". Tracks are also reconstructed by the Central Fast Tracker (CFT). The tracks found by the CFT are matched to EM clusters in the central region. The cluster finder also calculates transverse energy imbalance, which is a vector sum of the transverse energy of the towers. An event is required to pass a combination of L2 triggers.

The Level 3 trigger is designed to execute FORTRAN-77 filter algorithms as the last stage of on-line trigger selection. The software used is essentially the same as the offline reconstruction code. The primary differences in the cut quantities between the offline analyses and the Level 3 are: E_T is calculated using a vertex point at $z = 0$ and final database constants for tracking and calorimetry are not available. Events passing through the Level 3 trigger are recorded onto 8-mm tapes and disks.

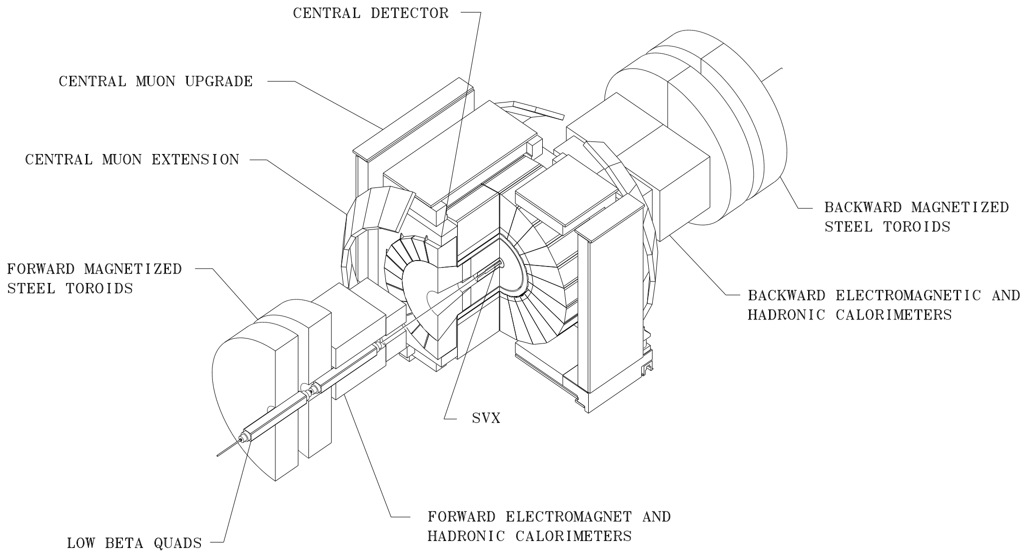

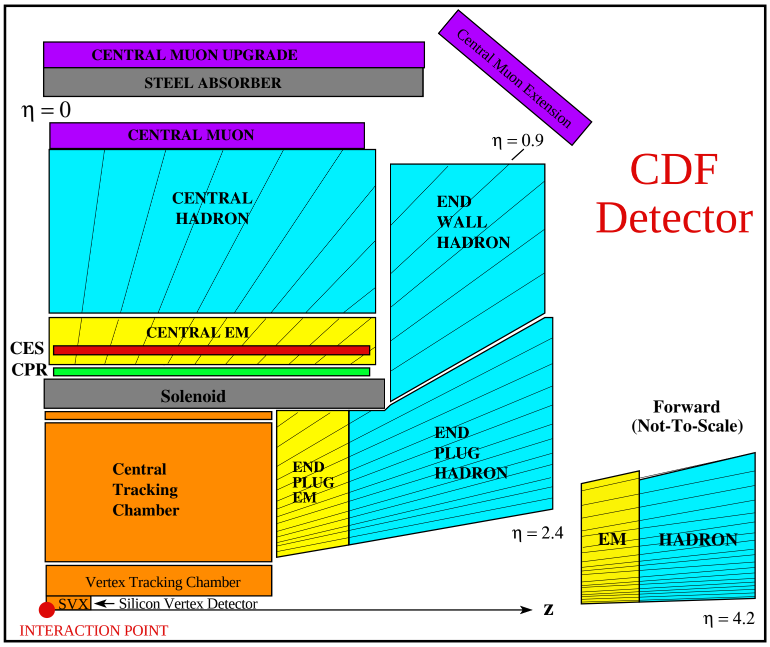

Figure 2.3: TOP: Schematic perspective view of the CDF detector. Bottom: The CDF detector. One quarter of the detector is shown.

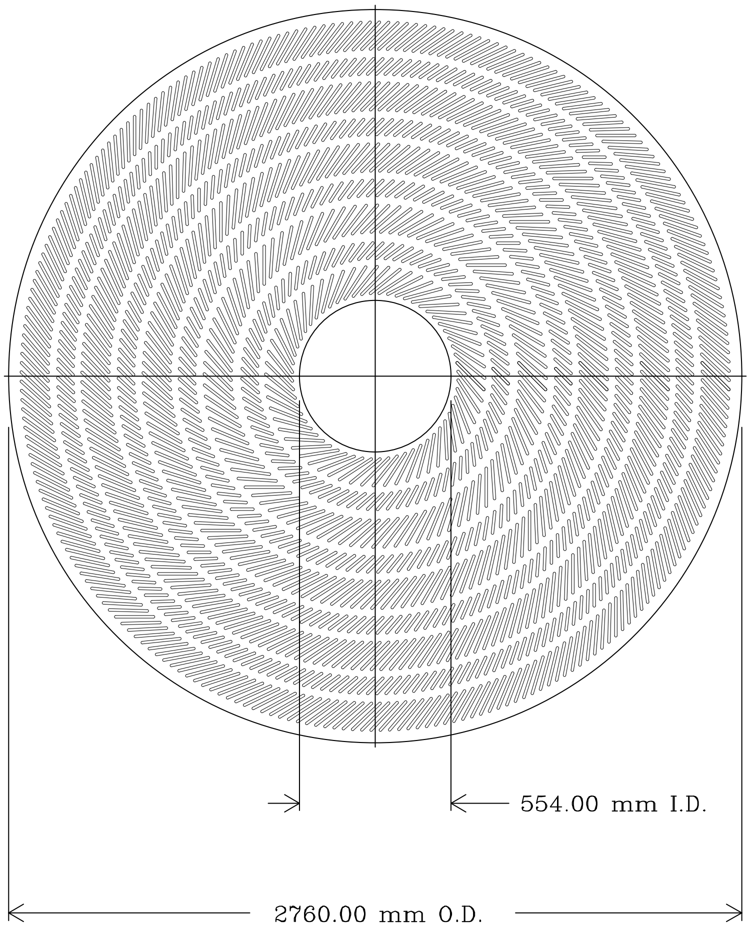

Figure 2.4: Schematic view of an endplate of the CTC showing the arrangement of the blocks which hold the 84 layers of sense wires.

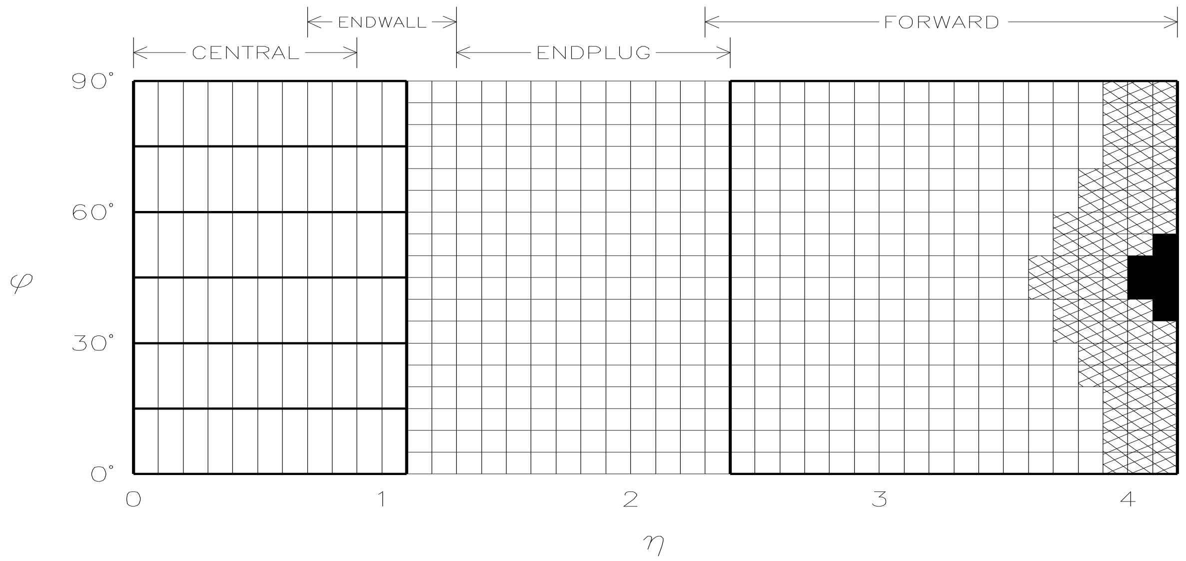

Figure 2.5: Map of the calorimetry coverage which shows the η-ϕ coverage of the separate calorimeters. The small squares represent the tower segmentation of the calorimeters.

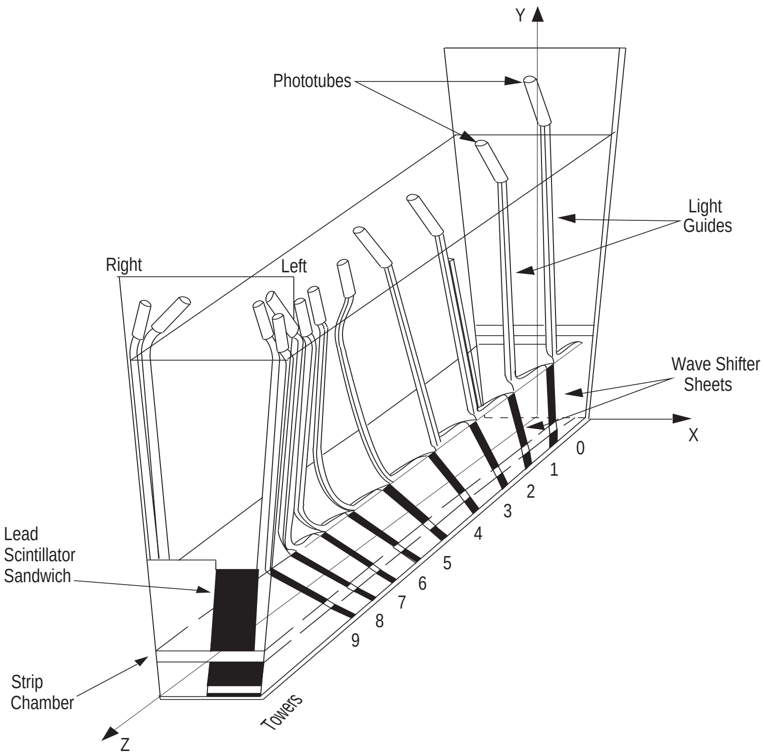

Figure 2.6: A wedge of the CEM. The CES strip chambers are embedded in the CEM where the maximum of an electron shower is expected to be.

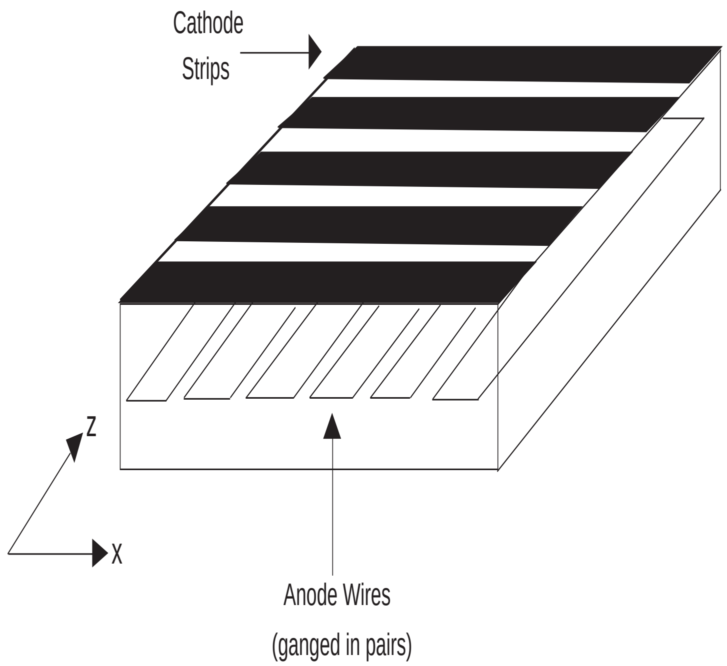

Figure 2.7: The local coordinate of the CES.

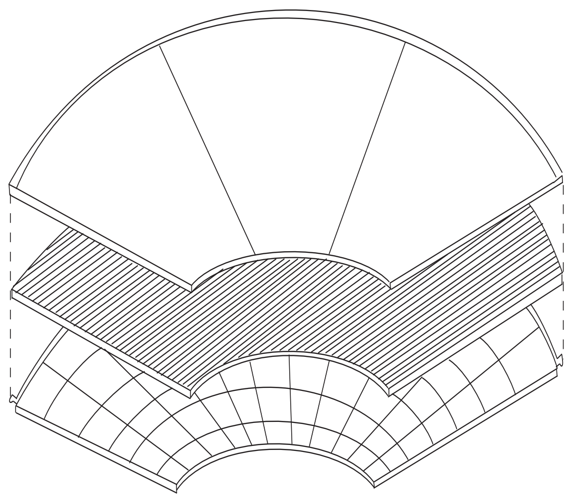

Figure 2.8: The construction of the grounding plane (top), proportional tubes (middle), and cathode pads (bottom).

Chapter 3

Event Selection

The data collected at the CDF during the 1992–1993 (Run 1A) and 1994–1995 (Run 1B) runs corresponding to 110 pb^{-1} are used in this analysis.

The key event signature to this analysis is an isolated electron with large transverse energy (E_T) and a large missing transverse energy ($\not\!\!E_T$) in an event.

Section 3.1 describes the data sets in more detail and Sections 3.2 and 3.3 define what we consider an electron and how we determine the missing transverse energy. Z boson background is removed as shown in Section 3.4 and we present the final W boson candidate events in Section 3.5.

3.1 Data Set

Several datasets are made using combinations of Level 3 triggers. The ICE is the inclusive central electron data set of Run 1A where most important requirements are $E_T > 18$ GeV and $p_T > 13$ GeV/c. The EIA is the inclusive central electron data of Run 1B. The EWA is the W electron in the central region data set of the Run 1B; most important requirements are $E_T > 22$ GeV and $p_T >$13 GeV/c, and large missing transverse energy ($>$ 22 GeV). The definition of the missing transverse energy is given in Section 3.3. The EZA is the Run 1B Z electrons data set, where at least one electron with $E_T > 22$ GeV and $p_T > 13$ GeV/c is required in the central region and a second electron with $E_T > 20$ (CEM), 15 (PEM), or 10 (FEM) GeV is also required. The EIA and EZA data sets are used in the following chapters for background study and missing transverse energy correction study. In this chapter, we select W events from ICE and EWA date sets.

3.2 Electron Quality Cuts

We use W events with electrons in the central region, $|\eta| < 1.1$. The acceptance of this requirement is not good (about 45 %. See Chapter 6), however, the quality of the data is good (less background, good energy measurement).

An electron energy cluster consists of a seed tower and one or two shoulder towers. The seed tower is identified as any tower with $E_T > 3$ GeV in the CEM. If the EM towers adjacent in pseudorapidity to the seed tower have $E_T > 0.1$ GeV, these towers (shoulder towers) are added to the seed tower. If the tower has more energy than the seed tower, that tower is considered a seed tower and the process is repeated with it. The maximum cluster size is restricted to three towers in pseudorapidity ($\triangle\eta = 0.3$) and one in azimuth ($\triangle\phi = 15°$).

The cut criteria for the central electrons are described below and summarized in Table 3.1 and the distributions of these quantities after the cut are shown in Figs. 3.1 $\sim$ 3.10.

Fiducial Volume

We restrict electrons to be in the fiducial volume of the CEM. The region $|\eta| < 0.05$, where the two halves of the detector meet, is excluded. The region $0.77 < \eta < 1.0$, $75° < \phi < 90°$ is uninstrumented because it is the penetration for the cryogenic connections to the solenoidal magnet. The region $1.05 < |\eta| < 1.10$ is also excluded because of the smaller depth of the electromagnetic calorimeter in this region. In addition, we exclude edges of the towers; the electrons which lie within 21 cm of the tower center in the r-ϕ view are used so that the showers are fully contained in the active region. The fiducial area is 78.9% of the CEM.

Transverse Energy

An EM cluster is required to have transverse energy (E_T) $\geq$ 25 GeV. The transverse energy is corrected due to:

- response variations in the individual CEM towers,
- tower-to-tower gain variation,
- time dependent gain variation.

The correction factors for the difference in the response in each individual tower of the calorimeter and the tower-to-tower gain correction factor are given from the test beam results with electrons [15]. The long-term stabilities of the phototubes, scintillating tiles, wave-shifting sheets, and the light guides are monitored during the runs and corrected at off-line level.

Lateral Energy Sharing of Towers

The lateral energy sharing (LSHR) of the calorimeter towers containing the electron shower must be consistent with the sharing measured in test beam electrons. The definition of L_{shr} is:

$$L_{shr} = 0.14 \sum \frac{E_i^{adj} - E_i^{prob}}{\sqrt{0.14^2 E + \left(\triangle E_i^{prob}\right)}} \tag{3.1}$$

where E_i^{adj} is the measured energy (E in GeV) in a tower adjacent to the seed tower, E_i^{prob} is the expected energy (in GeV) in the adjacent tower, $0.14\sqrt{E}$ (E in GeV) is the error on the energy measurement, and $\triangle E_i^{prob}$ (in GeV) is the error on the energy estimate. E_i^{prob} is calculated using a parameterization from test beam data. Fake electrons tend to have clusters wider than real electrons and therefore larger L_{shr}.

We require L_{shr} of our electrons to be less than 0.2.

Leakage into the Hadronic Calorimeters

The ratio HAD/EM of the energy deposited in the hadronic calorimeter to the energy deposited in the electromagnetic calorimeter is required to satisfy the following:

$$\frac{HAD}{EM} \leq 0.055 + 0.045 \cdot \frac{E}{100} \ , \tag{3.2}$$

where E is the energy of the electron cluster in GeV. The functional form is determined by studying energy deposition of electrons from a test beam.

Isolation

Electrons from W decay are expected to be "isolated"; the electromagnetic energy of the W electron should be physically separated from other energy in the detector. The isolation (ISO) is defined as the ratio of all non-electron energy around the electron to the electron energy:

$$ISO = \frac{E_T^{cone} - E_T^{cluster}}{E_T^{cluster}} \tag{3.3}$$

where E_T^{cone} is the sum of the electromagnetic and hadronic transverse energies in all of the towers (including the electron cluster) in a radius of $\triangle R = \sqrt{(\triangle\eta)^2 + (\triangle\phi)^2} = 0.4$ centered around the electron cluster, and $E_T^{cluster}$ is the electromagnetic transverse energy in the electron cluster. We require that ISO be less than 0.1.

High Transverse Momentum

Electrons and photons have similar calorimetry signatures. The CTC, however, measures momentum of charged particles, which allows us to distinguish an electron from photon. We require a three dimensional track with a p_T of at least 13 GeV/c pointing at the EM energy cluster.

Energy Momentum Ratio

We require the ratio of the electromagnetic energy of the electron cluster to the electron's momentum, E/p, to lie in the range from 0.5 to 2.0. The electrons with $E/p > 1$ are due to radiation of photons by the electron as they pass through the material. The radiated photons generally land in the same calorimeter cell as the electron, so E has the same value as the initial electron energy, but p is smaller because the momentum of photon is not measured.

Track-Shower Matching

The electron cluster's position measured in the CES is compared with the position of the CTC track pointing at the cluster. The CTC track is extrapolated to the CES. The variable $\triangle x$ and $\triangle z$ are the differences in the r-ϕ and r-z view between the CES strip cluster position and the extrapolated CTC track position. We require $\triangle x \leq 1.5$ cm and $\triangle z \leq 3.0$ cm.

Strip Chamber Pulse Height Shape

The lateral profile of the shower in the CES is measured by the cathode strips. The shower shape is required to be consistent with the shower shape measured for electrons from the test beam. This is quantified by a χ^2 test between the two distributions. We require $\chi^2_{strip} \leq 10.0$.

Event Vertex

The position in z of the primary event vertex is measured by the VTX. We require the vertex position ($|z_{vertex}|$) to be within 60 cm in z from the center of the detector to confirm the event occurring inside the fiducial region of the CDF detector.

Conversion Electron

Electrons from photon conversions are removed. A conversion electron is identified by searching for a second, oppositely signed charged track near the electron track in the CTC. We flag electrons as conversions if there is a second track with $|\Delta\,(r-\phi)\,| < 0.2$ cm and $|\Delta\,(cot\theta)\,| < 0.06$. The criteria are differences in the r-ϕ and θ views between the two tracks at their tangent point.

Detector region Central
Fiducial volume
$E_T \geq 25$ GeV
of 3D tracks in a cluster ≥ 1
$p_T \geq 13$ GeV/c
$\lvert z_{vertex}\rvert \leq 60.0$ cm
$0.5 \leq E/p \leq 2.0$
$L_{shr} \leq 0.2$
HAD/EM $\leq 0.055 + 0.00045E$
$\chi^2_{strip} \leq 10.0$
Iso ≤ 0.1
$\mid \triangle x \mid \leq 1.5$ cm
$\mid \triangle z \mid \leq 3.0$ cm
conversion removed

Table 3.1: High E_T electron selection cuts.

3.3 Missing Transverse Energy

A neutrino does not interact in the CDF detector. A large missing transverse energy, however, exists as the result of the production of the neutrino (transverse momentum of the neutrino). The missing E_T is calculated from

$$\not{E}_T \equiv \left|(-1) \times \sum \vec{E_T^i}\right| \quad , \tag{3.4}$$

where $\vec{E_T^i}$ is a vector whose magnitude is the transverse energy in a calorimeter tower and whose direction points from the event vertex to the center of the calorimeter tower. For Level 3 triggers, the direction points from $z = 0$, because what vertex to use is physics dependent and the least bias is introduced by choosing $z = 0$. We use the vertex nearest to the electron track as the event vertex, and recalculate all E_T^is using it.

In the above calculation of the missing E_T, we do not correct for the magnitude of $\vec{E_T^i}$ as described in Section 3.2. The sum is performed within the region $|\eta| < 3.6$.

For W events, the $\not\!\!E_T$ spectrum is similar to the electron spectrum. We require $\not\!\!E_T \geq 25$ GeV, the same criterion we do for the electron.

3.4 Z Veto

Electrons (positrons) from Z bosons can pass the electron selection as easily as electrons (positrons) from W bosons. The $\not\!\!E_T$ cut removes most of Z events, but some of them can survive the cut. We remove these Z events by searching for "second" electrons. The following Z identification cuts are applied to a second electron:

- HAD/EM ≤ 0.125
- ISO ≤ 0.15
- $E_T \geq 20$ GeV (Central region)
  $E_T \geq 15$ GeV (Plug region)
  $E_T \geq 10$ GeV (Forward region)
- 76 GeV/$c^2 \leq M_{ee} \leq$ 106 GeV/c^2,

where the M_{ee} is the electron-positron invariant mass.

3.5 Selected W Events

We obtain 62165 W events by the above cuts. The E_T distribution of the electrons and the $\not{E}_T$ distribution are shown in Figs. 3.10 and 3.11.

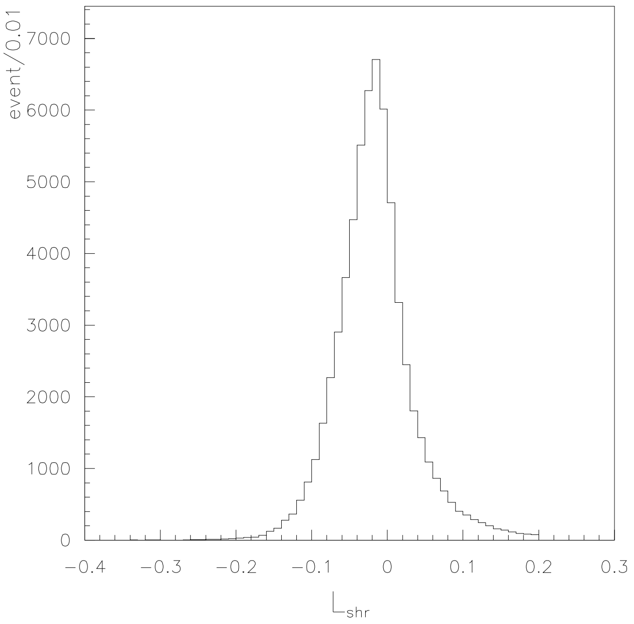

Figure 3.1: The L_{shr} distribution of electrons, after the electron cuts, $\not{E}_T$ cut, and Z veto cuts.

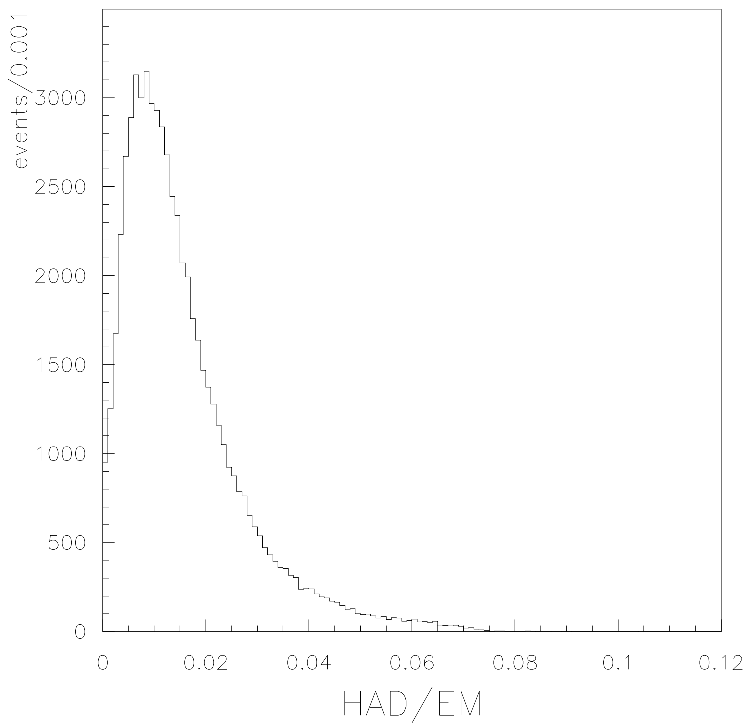

Figure 3.2: The HAD/EM distribution of electrons, after the electron cuts, $\not{E}_T$ cut, and Z veto cuts.

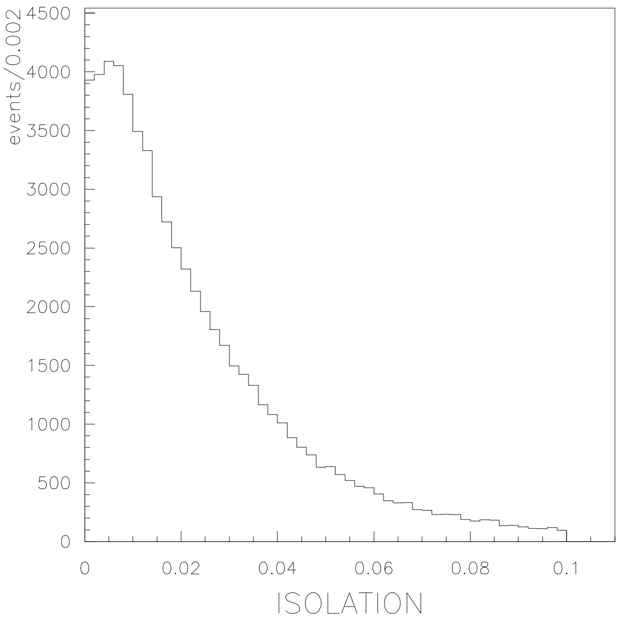

Figure 3.3: The isolation distribution of electrons, after the electron cuts, $\not{E}_T$ cut, and Z veto cuts.

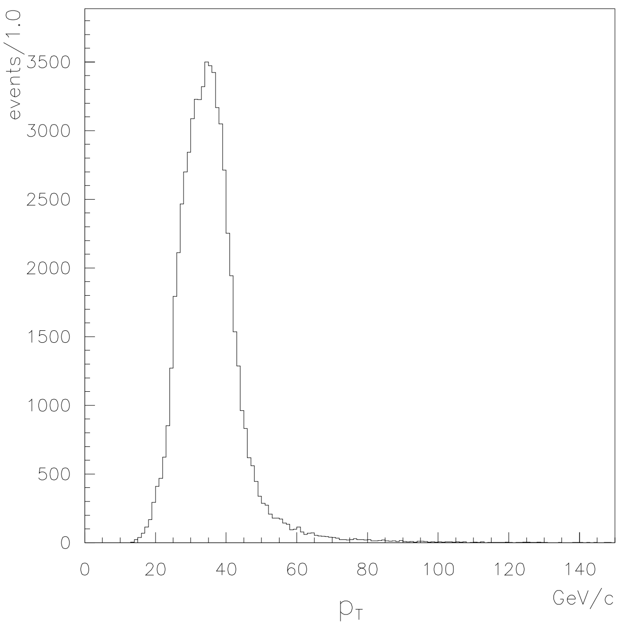

Figure 3.4: The transverse momentum distribution of electrons, after the electron cuts, $\not{E}_T$ cut, and Z veto cuts.

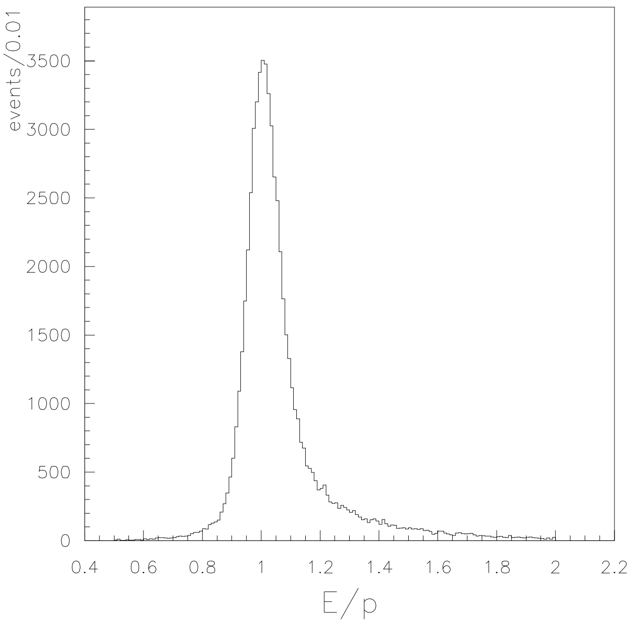

Figure 3.5: The E/p distribution of electrons, after the electron cuts, $\not{E}_T$ cut, and Z veto cuts.

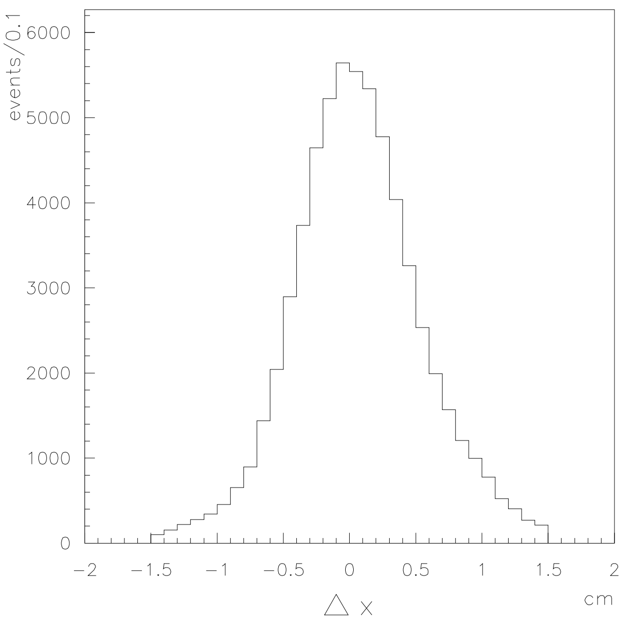

Figure 3.6: The $\triangle x$ distribution of electrons, after the electron cuts, $\not{E}_T$ cut, and Z veto cuts.

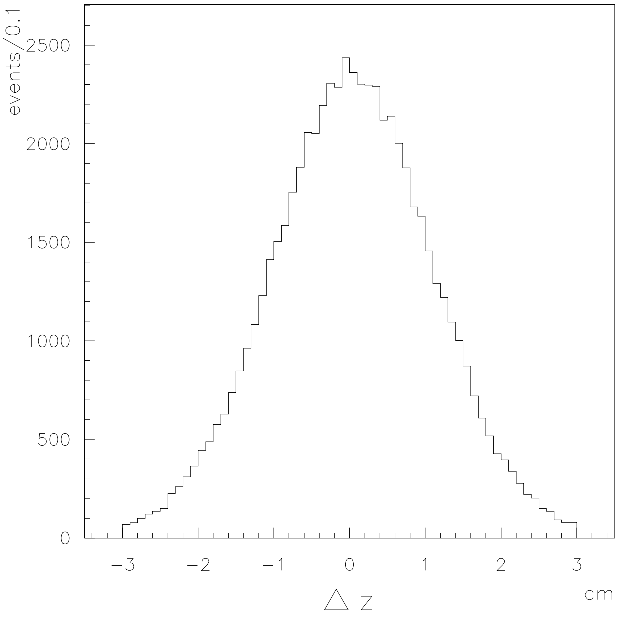

Figure 3.7: The $\triangle z$ distribution of electrons, after the electron cuts, $\not{E}_T$ cut, and Z veto cuts.

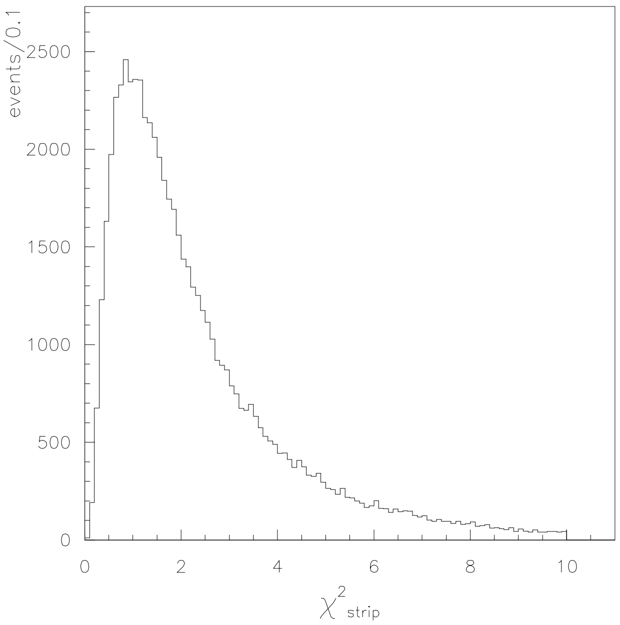

Figure 3.8: The χ^2_{strip} distribution of electrons, after the electron cuts, $\not{E}_T$ cut, and Z veto cuts.

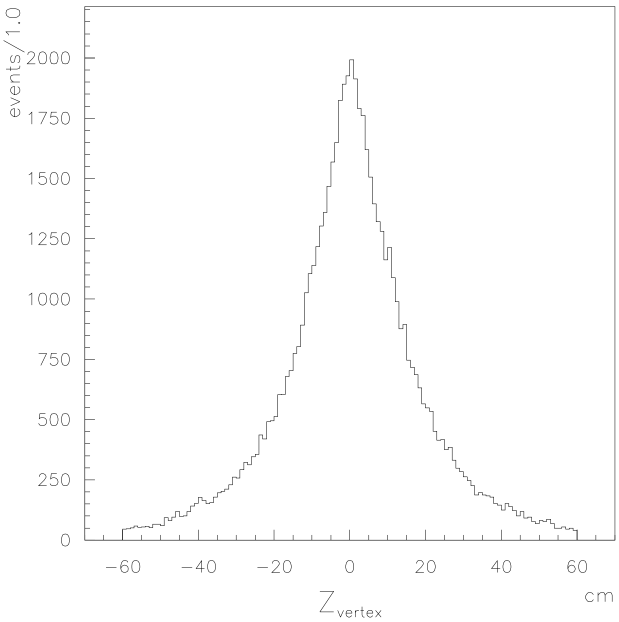

Figure 3.9: The z_{vertex} distribution of electrons, after the electron cuts, $\not\!\!E_T$ cut, and Z veto cuts.

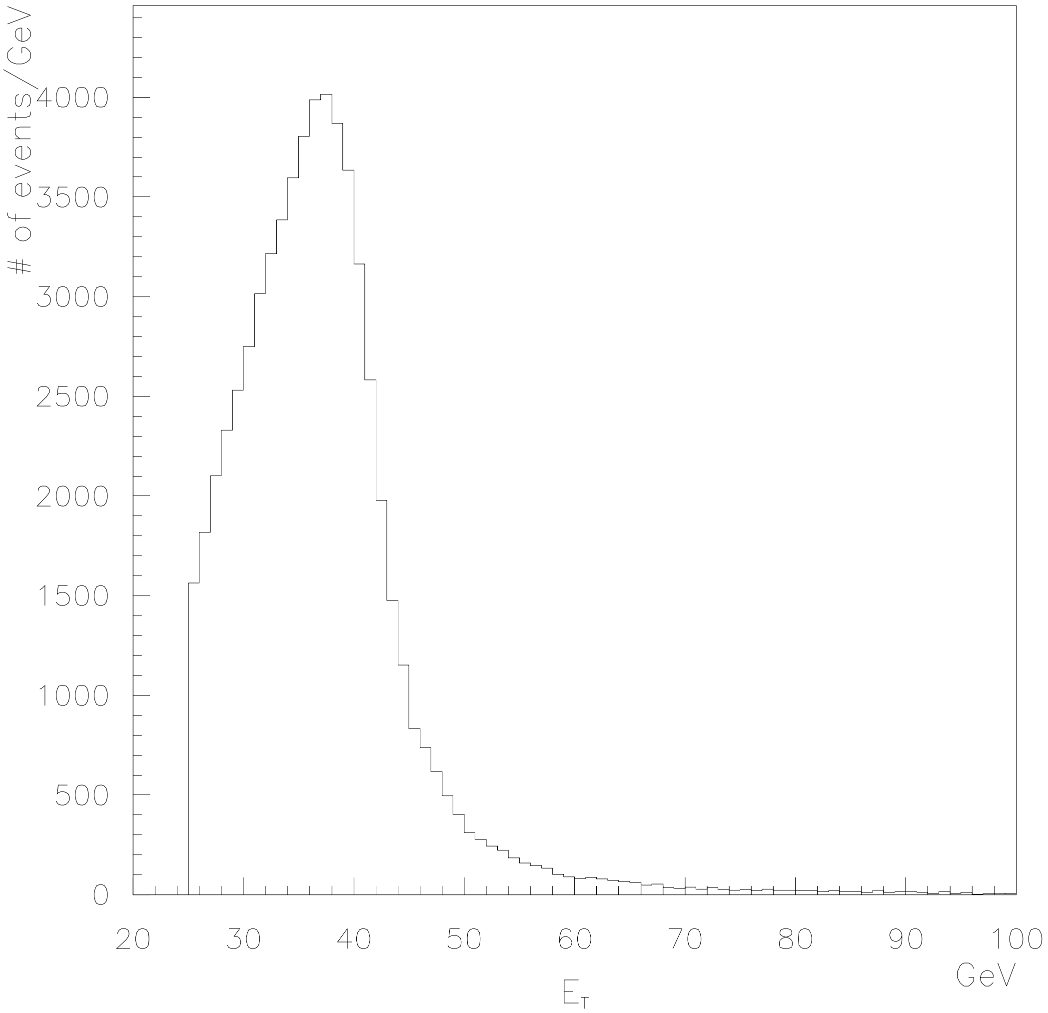

Figure 3.10: The transverse energy distribution of the W electrons.

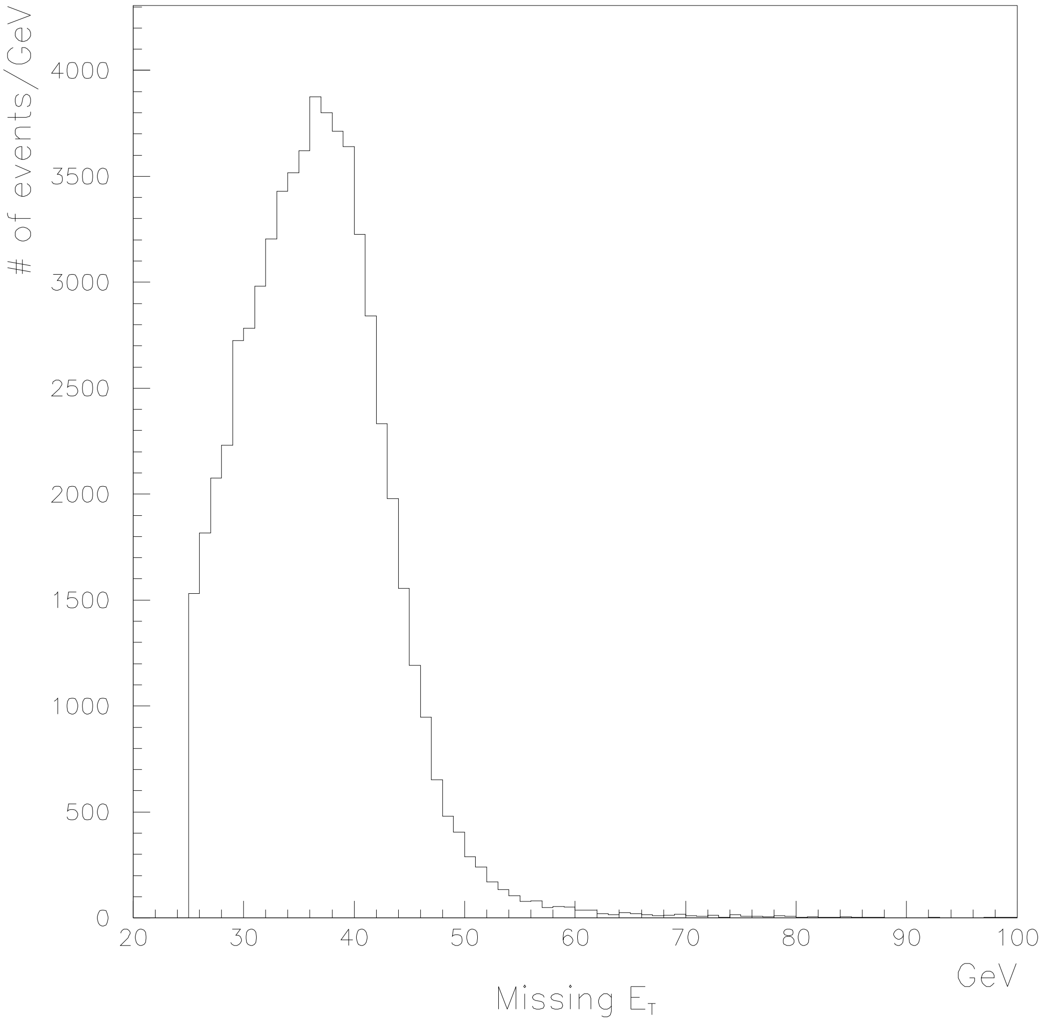

Figure 3.11: The missing transverse energy distribution of the W sample.

Chapter 4

Recoil Energy

The P_T^W is reconstructed from the electron and neutrino energies, E_T^{ele} and E_T^{ν}:

$$\vec{P_T^W} = \vec{E_T^{ele}} + \vec{E_T^{\nu}} \quad . \tag{4.1}$$

However, as described in the previous chapter, the transverse energy of the neutrino itself is undetected and needs to be reconstructed from all measured transverse energies which include the one from the electron. The transverse energy of the electron is therefore cancelled out from the above P_T^W calculation and only the energies of the particles recoiling the W boson remain;

$$\begin{aligned} \vec{P_T^W} &= \vec{E_T^{ele}} + \vec{\not{E}_T} \\ &= \vec{E_T^{ele}} + \left\{ - \left(\vec{E_T^{ele}} + \sum_{Recoil\ particles} \vec{E_T} \right) \right\} \\ &= - \sum_{Recoil\ particles} \vec{E_T} \quad . \end{aligned} \tag{4.2}$$

We classify the recoil particles into two groups, *jet* and *unclustered energies* due to their transverse energies:

$$\begin{aligned} \vec{P_T^{rec}} &= \sum_{Recoil\ particles} \vec{E_T} \\ &= \sum \vec{E_T^{jet}} + K \cdot E_T^{unc} \quad . \end{aligned} \tag{4.3}$$

Here the E_T^{jet} is the transverse energy of a jet cluster with $E_T \geq 10$ GeV. The clustering method is described in the following section. The E_T^{unc} is the vector sum of transverse energies of all towers except one from the jet clusters or the electron cluster. The factor K is the correction factor for unclustered energies and is determined using $Z \to ee$ events as described in Section 4.2.

4.1 Jet

4.1.1 Jet Energy Clustering

We use a cone clustering algorithm for finding jets [16]. This algorithm starts with looking for a seed tower. All calorimeter towers containing more than 1.0 GeV of transverse energy are seed towers. Towers in a cone $R = \sqrt{(\triangle\phi)^2 + (\triangle\eta)^2}$ around the seed tower are included in the cluster, if they have E_T more than 0.1 GeV. Using each tower in the cluster, the E_T weighted centroid is calculated and a new cone is formed around the centroid. The process is iterated until the towers in the cone remains unchanged.

We use a cone radius of 0.4 for the clustering algorithm. This choice is less susceptible to energy contamination from outside the jet. We show a $W + 1$ jet event as an example of the jet clustering in Fig 4.1.

4.1.2 Jet Correction

The above clustering procedure defines a jet as the energy in a cluster of towers within the R of 0.4. The energies of these clusters must be corrected due to nonlinearity and nonuniformity in the calorimeter tower response.

The correction is achieved in two steps ([17, 18]). First, the energy of jets deposited in the plug and forward calorimeters are corrected to the same value as they would be measured in the central calorimeter. This correction is given as a function of η and p_T of a jet. We derive this function using dijet events. Since dijets should balance back-to-back in p_T, if one of jets is measured well in the central calorimeter, the other measured anywhere in the detector can be corrected by requiring them to balance. After this

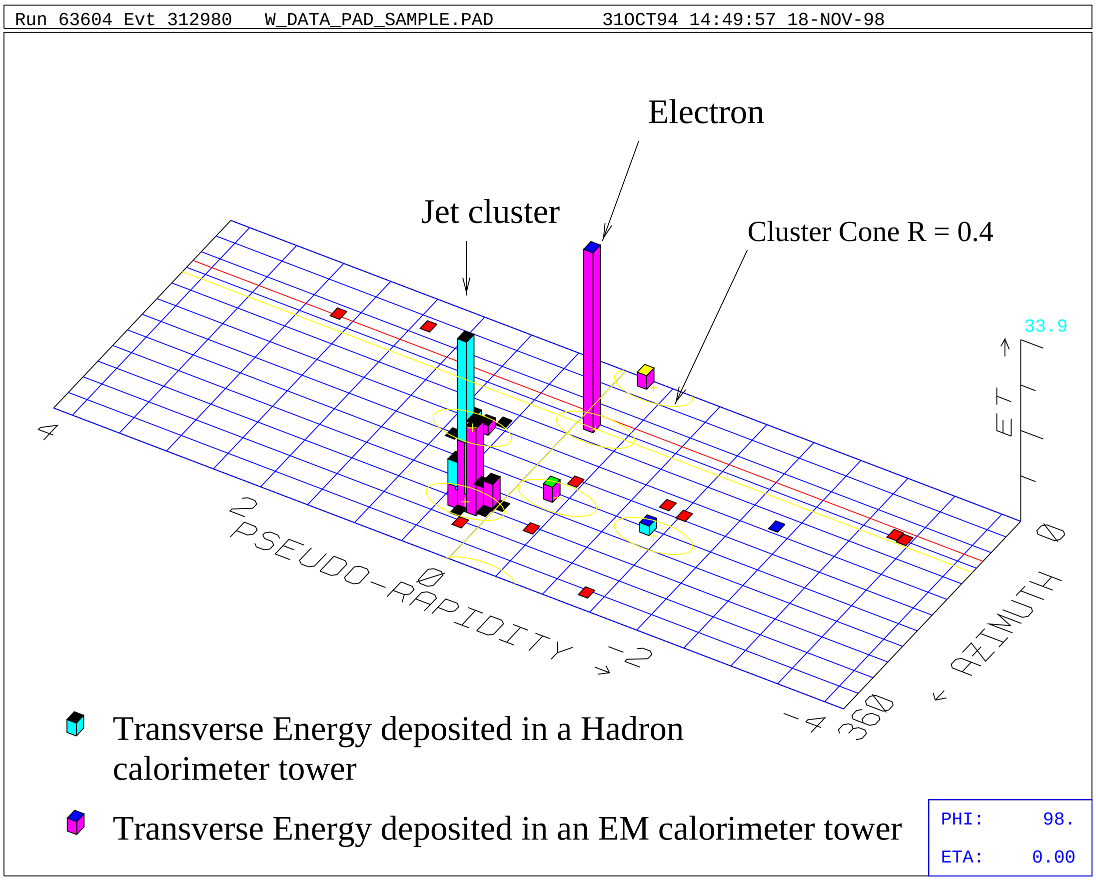

Figure 4.1: A $W(\rightarrow e\nu) + 1$ jet event. An ellipse shows a jet clustering area with the cone radius R of 0.4.

relative correction applied, the second step which is an "absolute" correction is applied. This is an attempt to make the energy of the cluster as close as possible to the parton energy. The relation between clusters and partons were studied using a GEANT simulation.

4.2 Unclustered Energy

We calculate the unclustered energy by summing the transverse energy vectors ($\vec{E_T}$) of all towers except ones included in jet clusters or the electron cluster ([19, 20]). The unclustered energies are corrected using the constant factor K. We determined this factor K using $Z \rightarrow ee$ events, because we can compare the transverse momentum of the recoil to well-measured transverse momentum of the Z boson.

4.2.1 Control Sample

We use $Z \to ee$ events from Run 1 as the control sample. We require that an event has two central electrons or one central and another plug electrons. Central electrons should pass the same cuts as we require for W events in the previous chapter. Plug electrons should pass the loose cuts shown in Table 4.1.

$E_T^{corrected} \geq 15$ GeV
$\chi^2_{3\times3} \leq 3.0$
fiducial cut
conversions removal cut

Table 4.1: Cut criteria for the plug electrons of Z events.

The invariant mass of two electrons is required to lie within a mass window, $81 \leq M_{ee} \leq 101$ (GeV/c^2).

We only use Z sample with no jet activities ($E_T^{jet} \geq 10$ GeV) to remove uncertainties from jet energy measurements.

The M_{ee} distribution is shown in Fig. 4.2.

4.2.2 The K Factor

We define the K factor so as to balance the recoil energy distribution with momentum distribution of the Z boson. In lower P_T^Z regions, uncertainties in energy of electrons may lead to large uncertainty in P_T^Z, because electrons from Z move almost back to back. To reduce these uncertainties from electron energy measurement, we only use the components along the direction of the angular bisector of the electron pair (Fig. 4.3). We denote this direction by η, and the perpendicular direction to the η direction by ξ.

The top figure in Fig. 4.4 shows the $E_\eta^{ele1} + E_\eta^{ele2}$ distribution of the

$Z \to ee$ control sample. The bottom figure shows the E_η^{unc} distribution of the Z sample. We require the mean of the distribution of $E_\eta^{ele1} + E_\eta^{ele2} + K \cdot E_\eta^{unc}$ to be zero:

$$\overline{\left(E_\eta^{ele1} + E_\eta^{ele2}\right)} + K \cdot \overline{E_\eta^{unc}} = 0 \tag{4.4}$$

We conclude $K = 2.0$. We show the distributions of $(E_\eta^{ele1} + E_\eta^{ele2} + K \cdot E_\eta^{unc})$ and $(E_\xi^{ele1} + E_\xi^{ele2} + K \cdot E_\xi^{unc})$ with $K = 2.0$ in Fig. 4.5. We also show the distributions of $(E_\eta^{ele1} + E_\eta^{ele2} + K \cdot E_\eta^{unc})$ with $K = 1.0$, 1.8, and 2.2 in Fig. 4.6.

4.2.3 P_T^{rec} Distribution of W Events

The recoil P_T of the W events is calculated with the factor $K = 2.0$. The distribution is shown in Fig. 4.7.

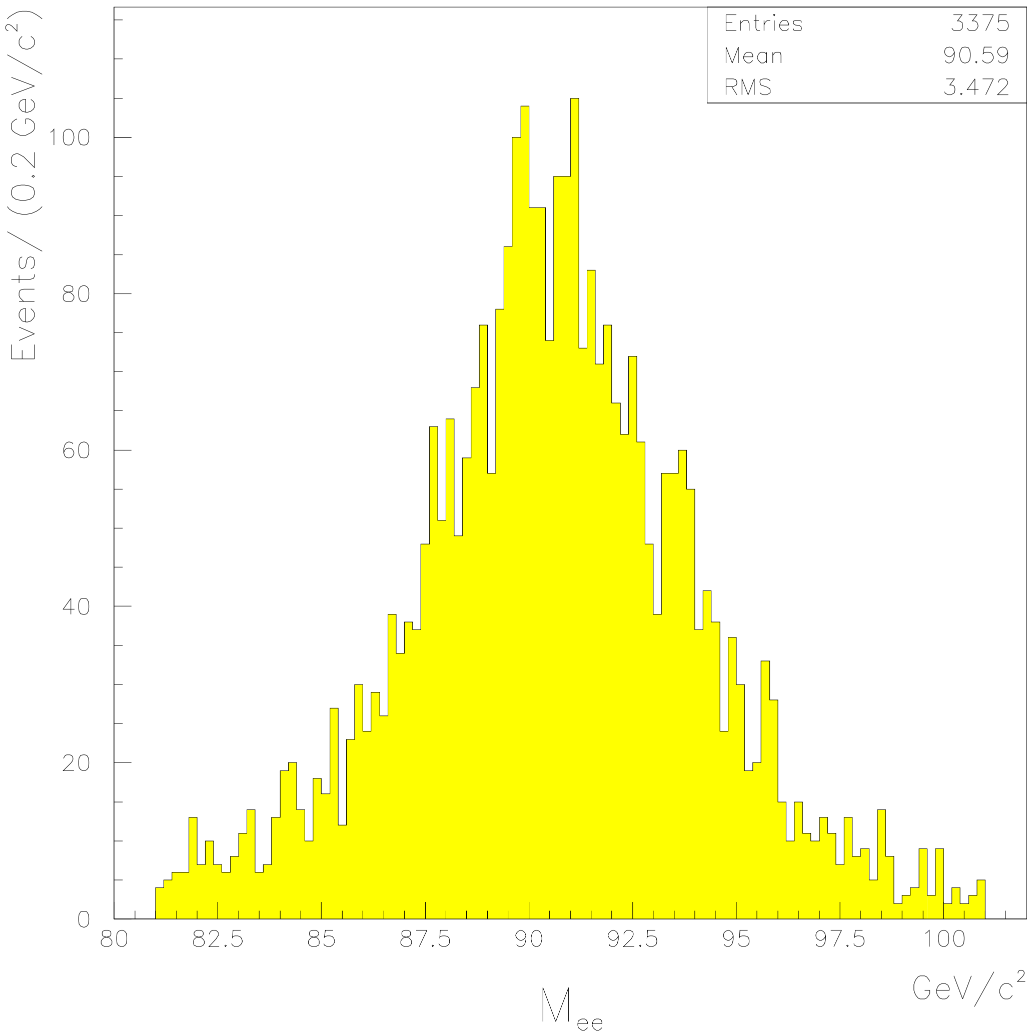

Figure 4.2: The invariant mass distribution of the electron pairs in the Z sample. At least one electron should be in the central region, the other should be in the central or plug regions. We require the data not have any jet cluster with $E_T \geq 10$ GeV.

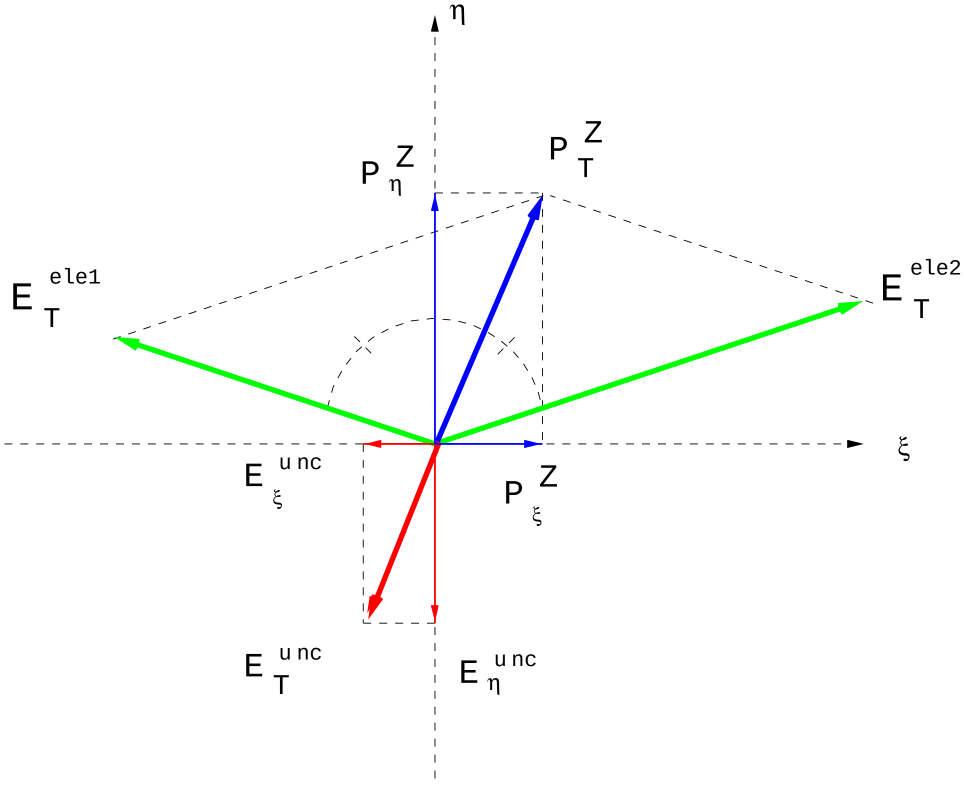

Figure 4.3: A $Z \rightarrow ee + 0$ jet event in the r-ϕ view. The bisector of the angle between the ee pair is labeled η. The perpendicular direction is labeled ξ.

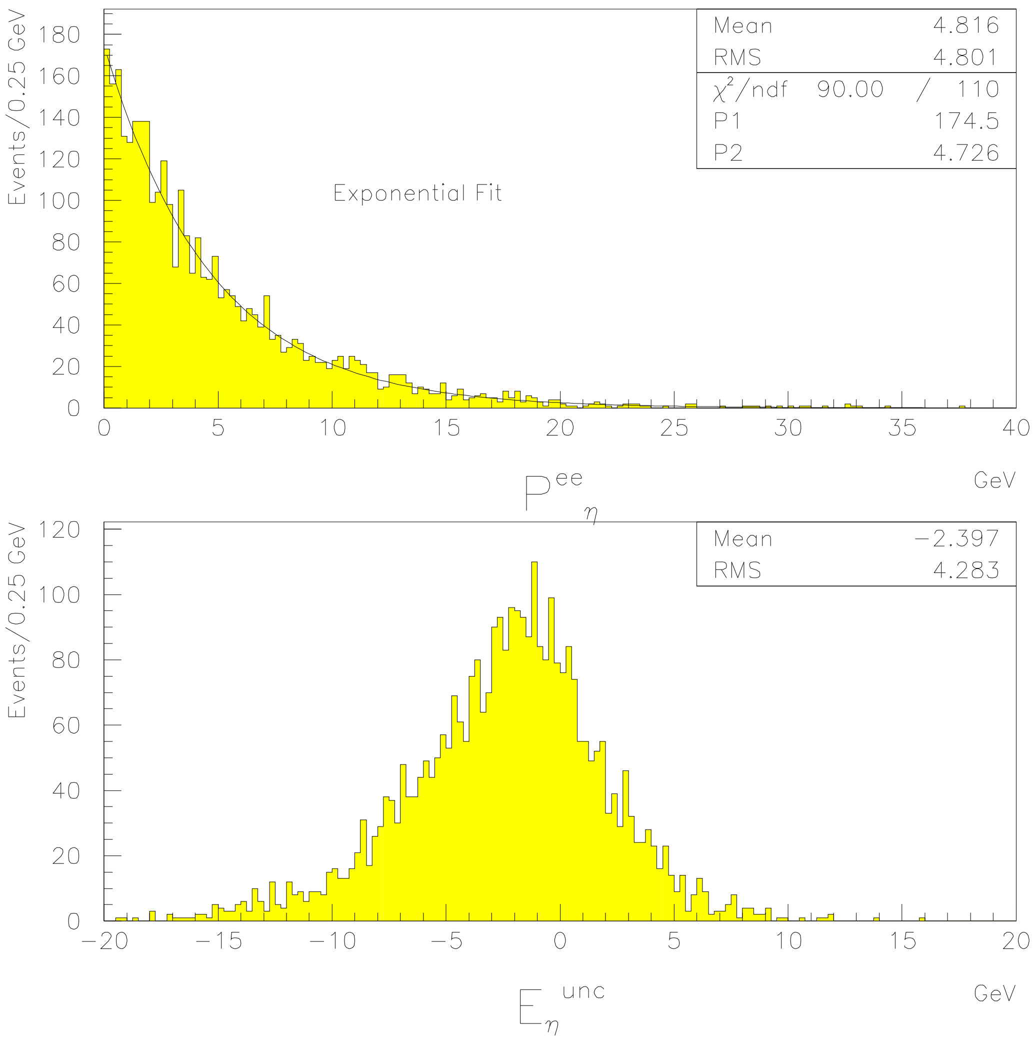

Figure 4.4: TOP: P_η^{ee} distribution of $Z+0$ jet ($E_T^{jet} \geq 10$ GeV) events. The line is a fit to the exponential curve. BOTTOM: E_η^{unc} distribution.

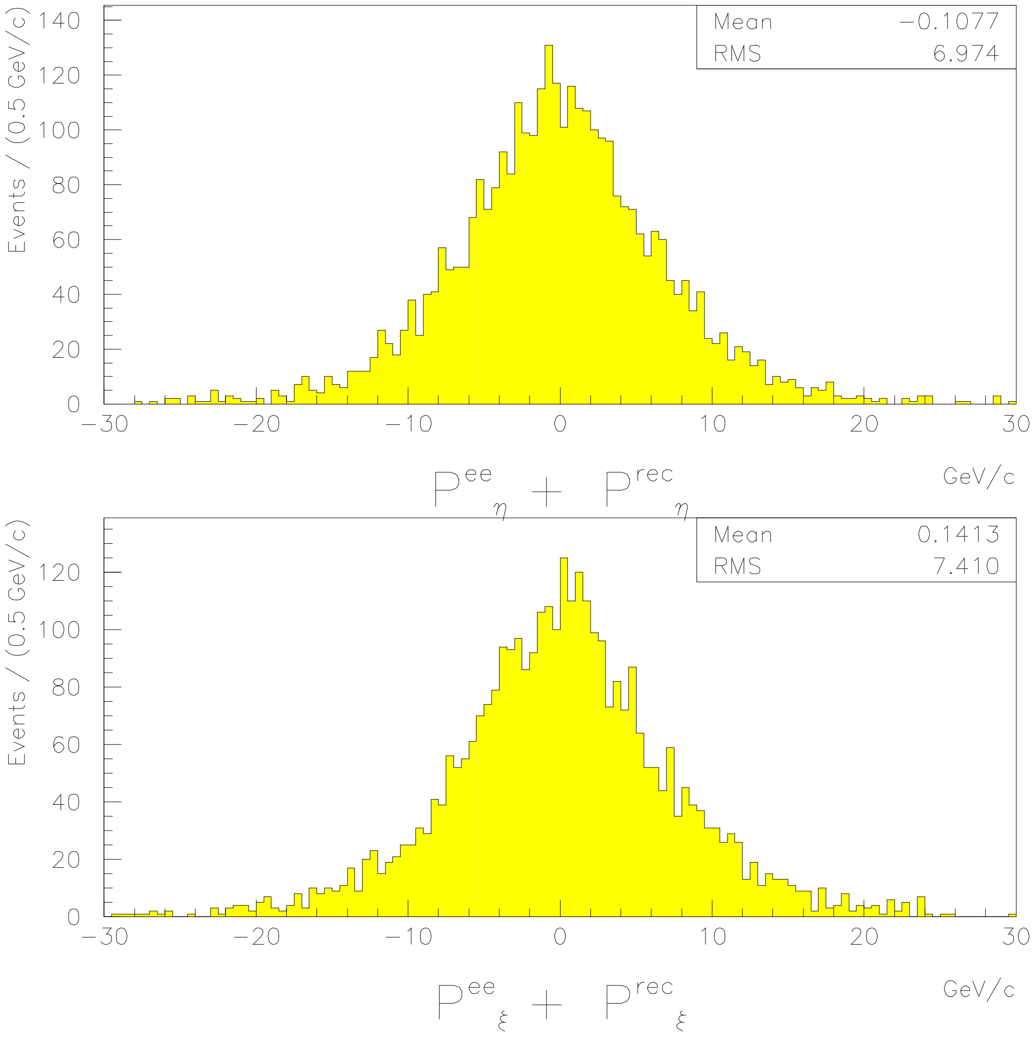

Figure 4.5: TOP: The distribution of $E_{\eta}^{ele1} + E_{\eta}^{ele2} + K \cdot E_{\eta}^{unc}$ with $K = 2.0$. The distribution is balanced by K. The data are required not to have any jet with $E_T^{jet} \geq 10$ GeV. BOTTOM: The distribution of $E_{\xi}^{ele1} + E_{\xi}^{ele2} + K \cdot E_{\xi}^{unc}$ with $K = 2.0$.

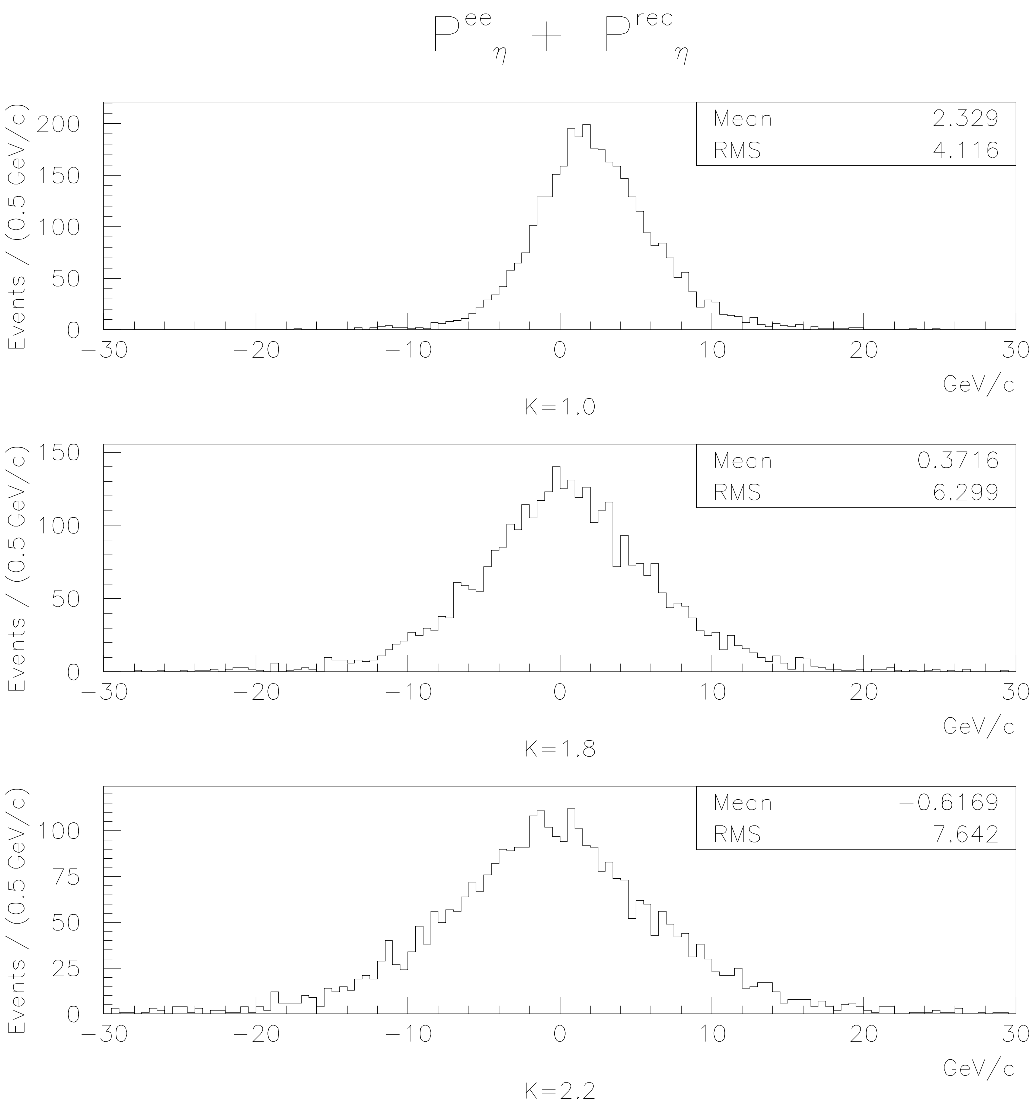

Figure 4.6: The distribution of $E^{ele1}_{\eta} + E^{ele2}_{\eta} + K \cdot E^{unc}_{\eta}$ with $K = 1.0$, 1.8, and 2.2.

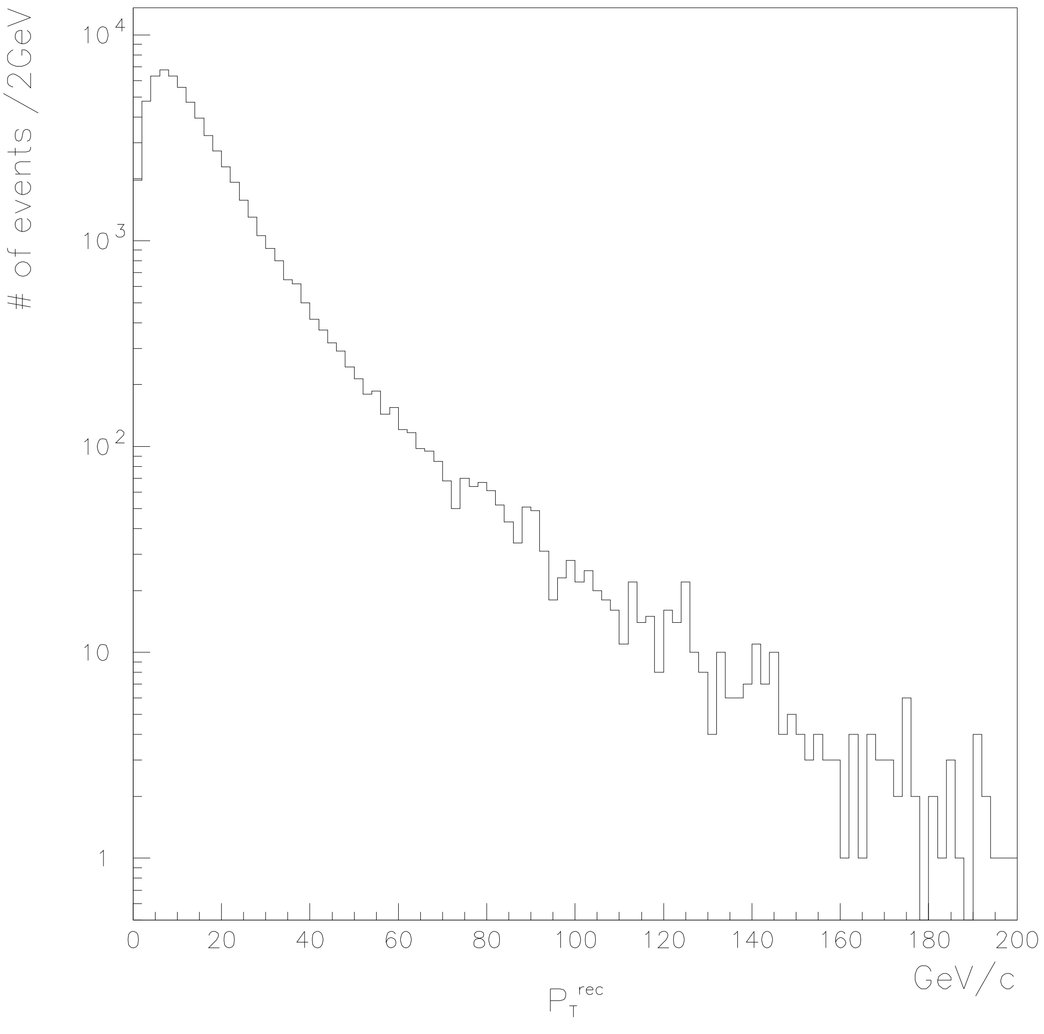

Figure 4.7: The distribution of the recoil transverse energy of the W events is shown in semi-log scale.

Chapter 5

Backgrounds

We selected $W \to e\nu$ events as described in Chapter 3. We, however, expect that some background events still remain in our data sample. In this chapter, we estimate these residual backgrounds. We consider backgrounds from QCD multijet production and single boson production ($W \to \tau\nu \to e\nu\nu\nu$ and $Z \to ee$). We can not remove these backgrounds individually using any further cuts, so we study their fractions in our data.

5.1 QCD Background

5.1.1 Introduction

A real electron is produced in the semileptonic decay of bottom quarks or charm quarks and can be misidentified as coming from a W decay. Quarks or gluons can fake an electron signature (*e.g.* $\pi^{\pm}\pi^{0}$ overlap). We refer to these events as QCD backgrounds. Even if an electron signature is produced, most of the background events are rejected by the $\not{E}_T$ cut. However, some events can produce large $\not{E}_T$ because of a jet escaping through a crack or because of mismeasurement of the energy cluster. The electrons from W decay are more isolated than the electrons from these backgrounds since they will tend to have other particles (*e.g.* b, c quark decay) near the electron. We estimate the QCD backgrounds remaining in our data using the isolation distribution of the "electrons" (the isolation extrapolation method[21]).

5.1.2 Data Sample

In order to study the isolation distribution of the background "electrons", we make a data sample which contains both QCD and W events from Run 1 data. We use the cut criteria for the W events selection (Chapter 3) except two cuts: we do not apply the $\not\!\!E_T$ cut and we do not apply the isolation cut for electrons in order to obtain a sample of QCD multijet events. Since we need events with low $\not\!\!E_T$, we use the inclusive data sets which do not require the $\not\!\!E_T$ trigger (ICE and EIA, Chapter 3). The E_T of the "electrons" and $\not\!\!E_T$ shapes are shown in Fig. 5.1.

5.1.3 The Isolation Extrapolation Method

We classify events into the following four categories according to their isolation (ISO) and $\not\!\!E_T$ values (Fig. 5.2):

- Region 1: ISO ≤ 0.1, $\not\!\!E_T \leq 10.0$ (GeV)
- Region 2: ISO ≥ 0.3, $\not\!\!E_T \leq 10.0$ (GeV)
- Region 3: ISO ≥ 0.3, $\not\!\!E_T \geq 25.0$ (GeV)
- Region 4: ISO ≤ 0.1, $\not\!\!E_T \geq 25.0$ (GeV)

The isolation distribution of the sample in each region is shown in Fig. 5.3. We assume events in Region 1, 2, and 3 are all QCD events and not W's. In Region 4, in contrast, most of them are assumed to be W's, with some small number of background events. Assuming the isolation shape of QCD events does not depend on $\not\!\!E_T$, we can calculate the number of QCD events in Region 4 (N_4^{QCD}) using the numbers of events in Regions 1, 2, and

3 ($N_{1,2,3}$) as follows:

$$N_4^{QCD} = R \times N_3 \tag{5.1}$$
$$R \equiv \frac{N_1}{N_2} \tag{5.2}$$

However, the isolation shape has some correlation with $\not\!\!E_T$. In Region 3 and 4, the QCD background events have at least two jets with $E_T \geq 25$ GeV: one jet is misidentified as an electron and the other causes large $\not\!\!E_T$. Therefore we require that the events in Region 1 and 2 have at least one jet in addition to the electron candidate. The fraction of electromagnetic energy in this jet must be less than 0.8. This jet corresponds to the jet recoiling against the "electron" in Regions 3 and 4. We show in Table 5.1 that R indeed varies with the E_T cut value of the jet. The isolation shapes of the events in Regions 1 and 2 with the jet requirements of $E_T^{jet} \geq 10$, 20, 25 GeV and without imposing the jet requirements are also shown in Fig. 5.4.

	Region 1	Region 2	Ratio R
≥ 0 jets	7240	2554	2.83
$E_T^{jet} \geq 10GeV$	5237	2429	2.16
$E_T^{jet} \geq 20GeV$	3957	2221	1.78
$E_T^{jet} \geq 25GeV$	3412	2107	1.62

Table 5.1: Number of events and the ratio R

Since we require the events in Region 3 and 4 have $\not\!\!E_T \geq 25$ GeV, we also require the events in Region 1 and 2 have at least one jet with $E_T \geq 25$ GeV in addition to the electron candidate.

We conclude $R = 1.62$.

5.1.4 Systematic Error

We can test this isolation extrapolation method by making two subsamples containing only QCD events. One subsample named *Low* $\not\!\!E_T$ *set* consists of the events in Region 1 and 2. The other subsample named *High ISO set* consists of the events in Region 2 and 3. Both subsamples are further divided into four regions as shown in Fig. 5.5. We require the events of the High ISO set have at least one jet with $E_T \geq 25$ GeV as we did above. We compare the number of events in Region 4 to the number calculated using the isolation extrapolation method. We show the results in Table 5.2.

	Region 1	Region 2	Region 3	Region 4	Ratio	Predicted
Low $\not{E}_T$	2137	747	1516	4252	2.86	4337
High ISO	1418	575	119	191	2.47	293.5

Table 5.2: Results of the test of the QCD background estimation. The number of events in Region 4 are directly counted.

The actual numbers in Regions 4 are 2% (LOW $\not{E}_T$ set) and 35% (High ISO set) less than the predicted numbers. We assign the larger discrepancy of 35% to the systematic uncertainty on our isolation extrapolation method. We therefore obtain:

$$R = 1.62 \pm 0.57 \tag{5.3}$$

5.1.5 Total Number of QCD Backgrounds

We have used the data samples from ICE and EIA in order to obtain the QCD sample. However, we use ICE and EWA for our W selection. Therefore we re-select events in Region 3 from ICE and EWA. We obtain 330 events in Region 3. The number of QCD backgrounds is thus:

$$N^{QCD} = 534.6 \pm 29.4(stat) \pm 188.1(syst) \ . \tag{5.4}$$

5.1.6 The P_T^{rec} Shape of QCD Background

We use the "P_T^{rec}" shape of the events in Region 3 as the shape of QCD background. The distribution is shown in Fig. 5.6. We assume that the correlation between the isolation and the P_T^{rec} distribution is negligible.

5.1.7 Conclusion of QCD Background

We estimate the QCD background in $W \to e\nu$ events by multiplying the P_T^{rec} distribution in Region 3 by the factor of $R = 1.62$. We subtract the number of QCD events from the number of W events as shown in Fig. 5.7. The contribution from QCD background events is negligibly small in lower P_T^W regions.

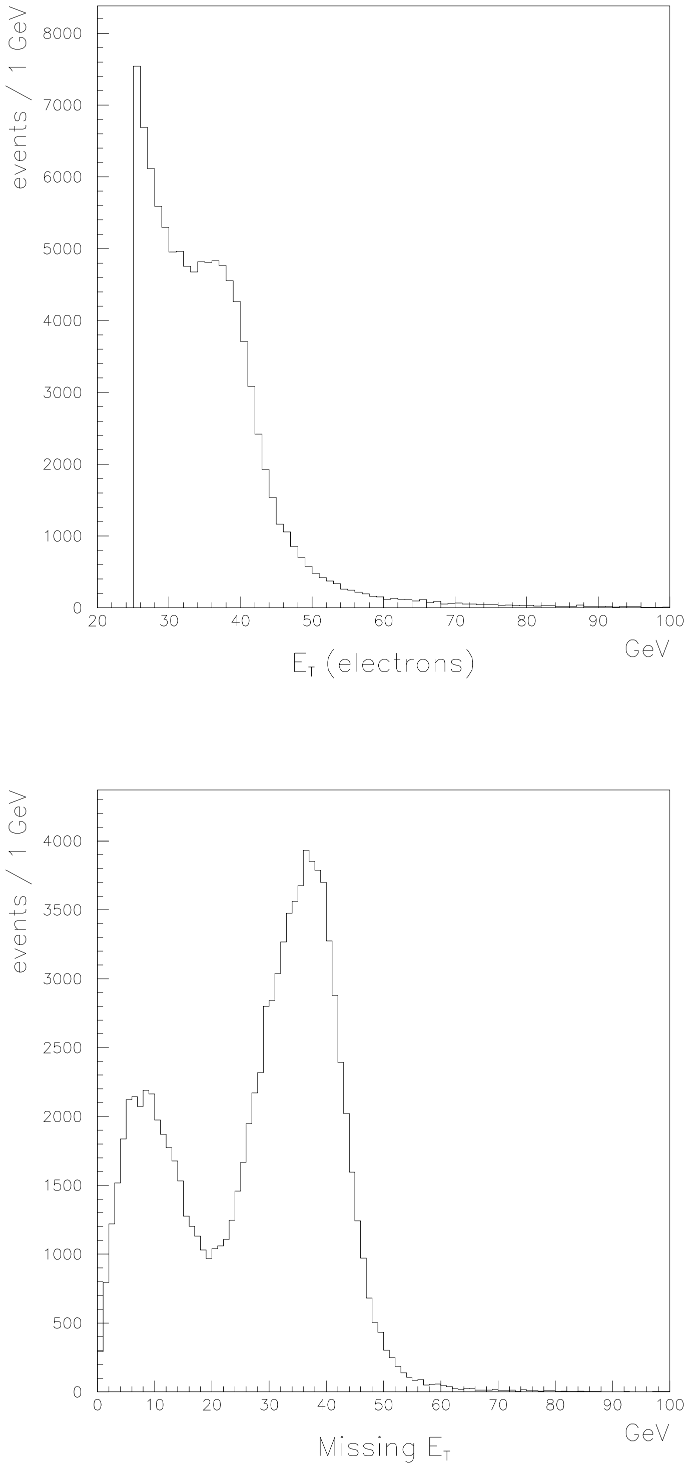

Figure 5.1: The data sample containing W and QCD events. TOP: the E_T distribution of "electrons". BOTTOM: the $\not\!\!E_T$ shape.

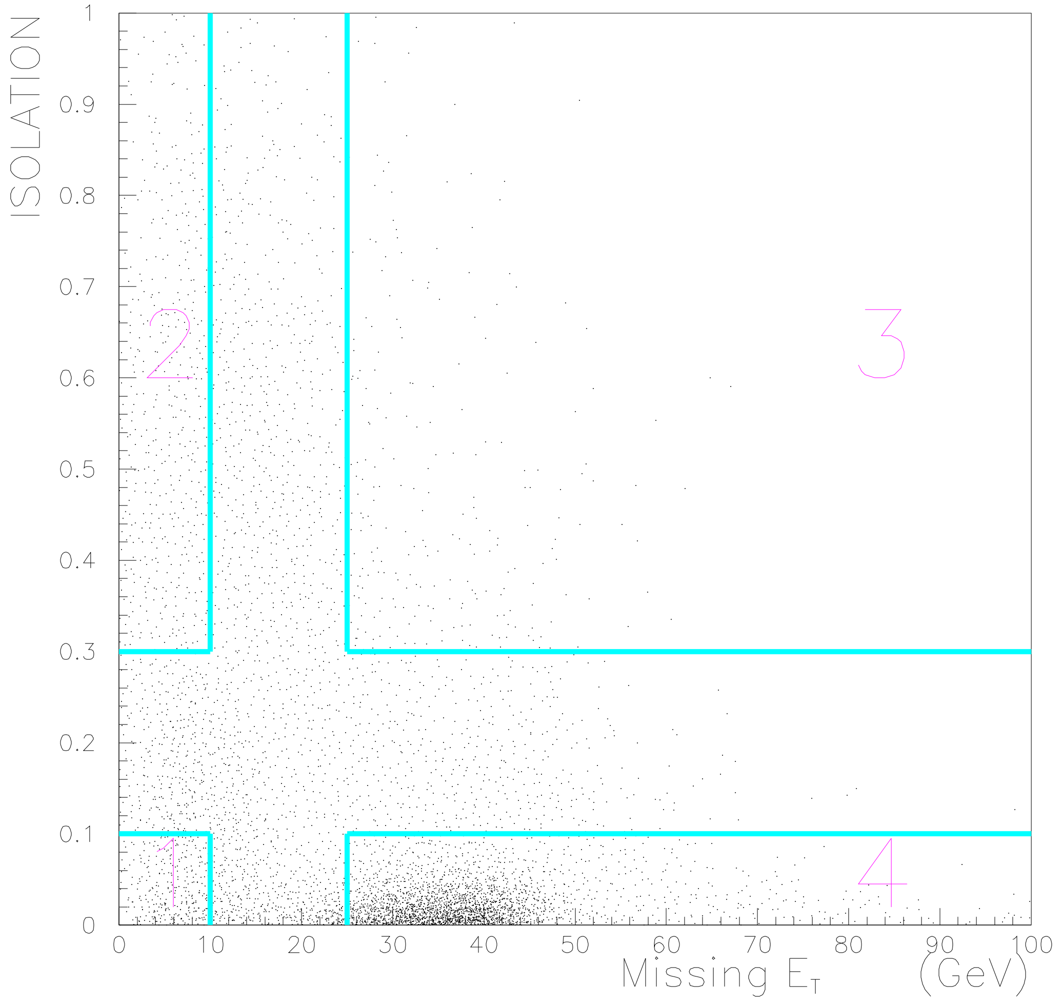

Figure 5.2: The isolation vs. $\not{E}_T$. Four regions are defined: Region 1: ISO ≤ 0.1 $\not{E}_T \leq 10$ GeV, Region 2: ISO ≥ 0.3 $\not{E}_T \leq 10$ GeV, Region 3: ISO ≥ 0.3 $\not{E}_T \geq 25$ GeV, and Region 4: ISO ≤ 0.1 $\not{E}_T \geq 25$ GeV.

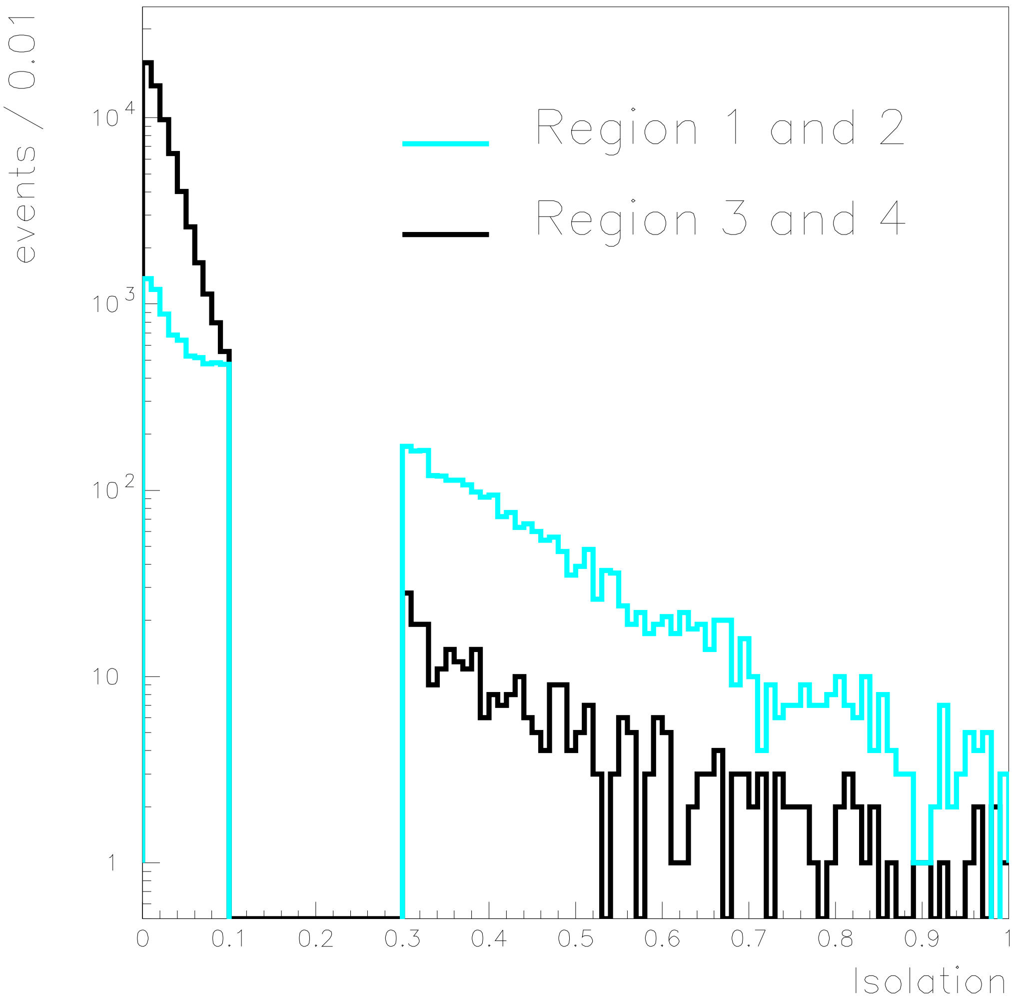

Figure 5.3: The isolation shapes; Region 1 (ISO$\leq$ 0.1), Region 2 (ISO $\geq$ 0.3), Region 3 (ISO $\geq$ 0.3), and Region 4 (ISO $\leq$ 0.1).

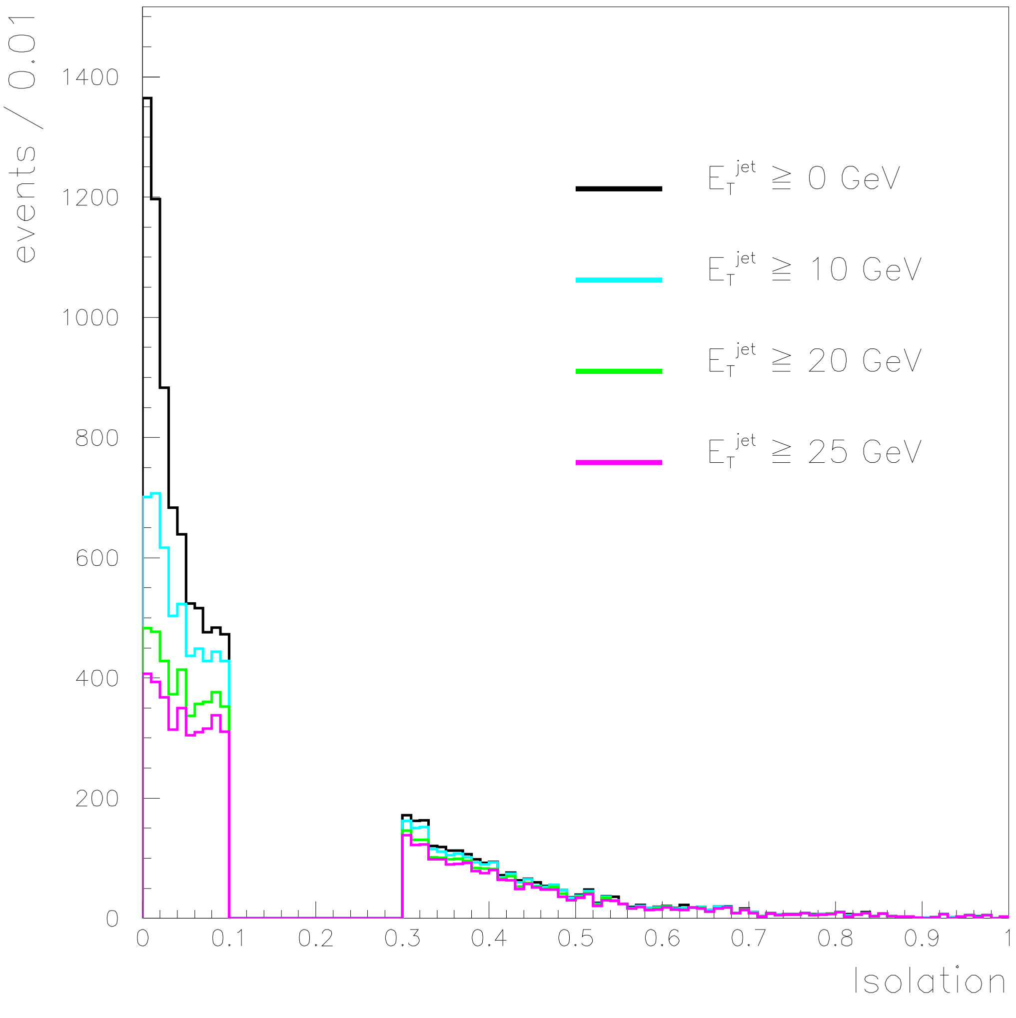

Figure 5.4: The isolation distributions in Region 1 (ISO ≤ 0.1) and 2 (ISO ≥ 0.3).

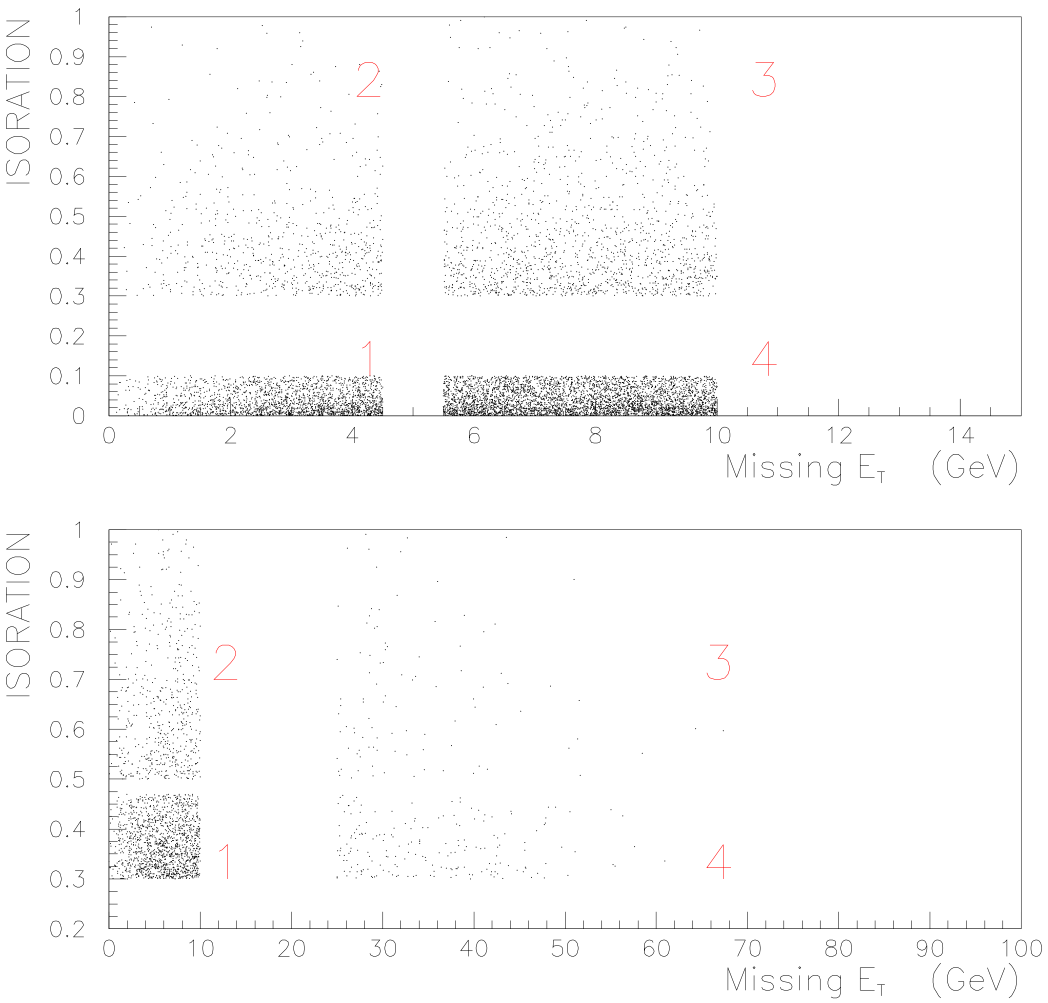

Figure 5.5: We make another two sets of the "four regions"; *Low* $\not\!\!E_T$ set (TOP) and *High ISO* set (BOTTOM).

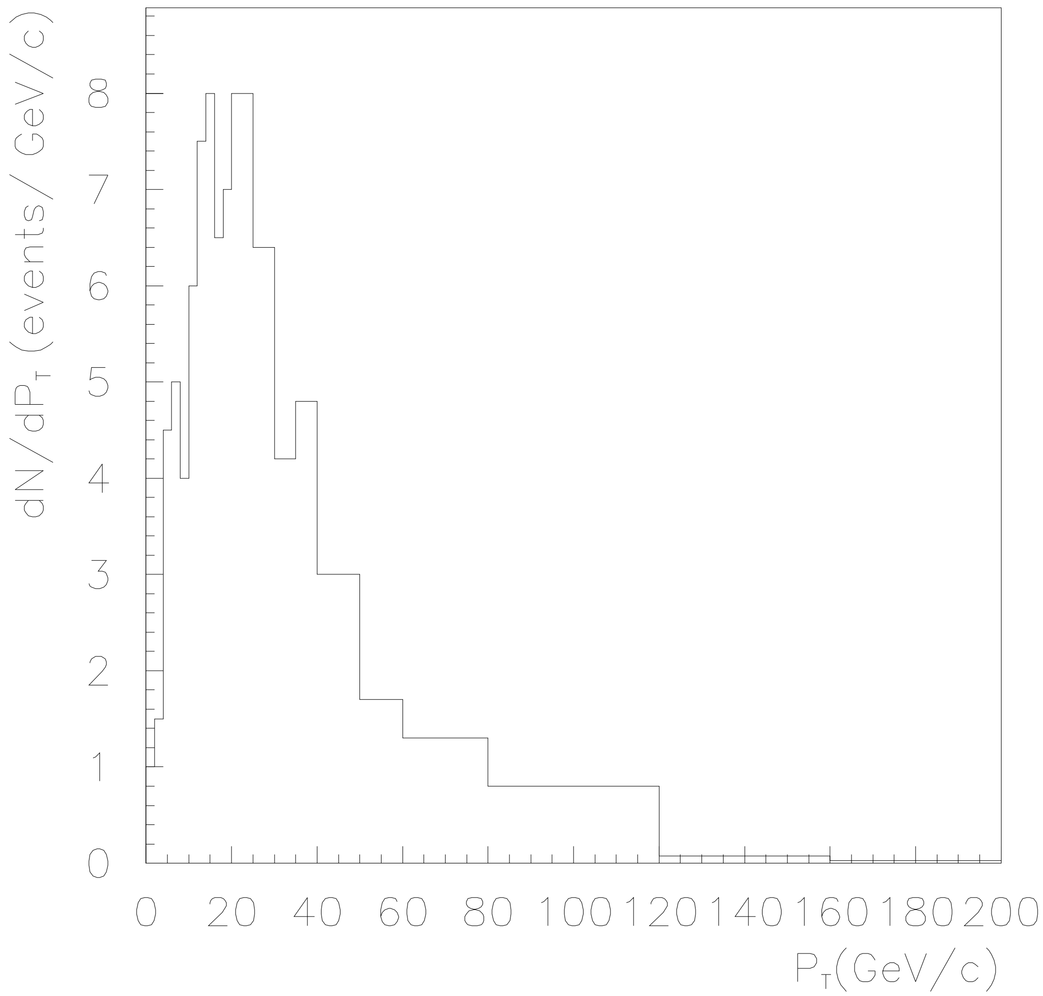

Figure 5.6: "P_T^{rec}" distribution of the events in Region 3. We use this shape as the QCD background shape.

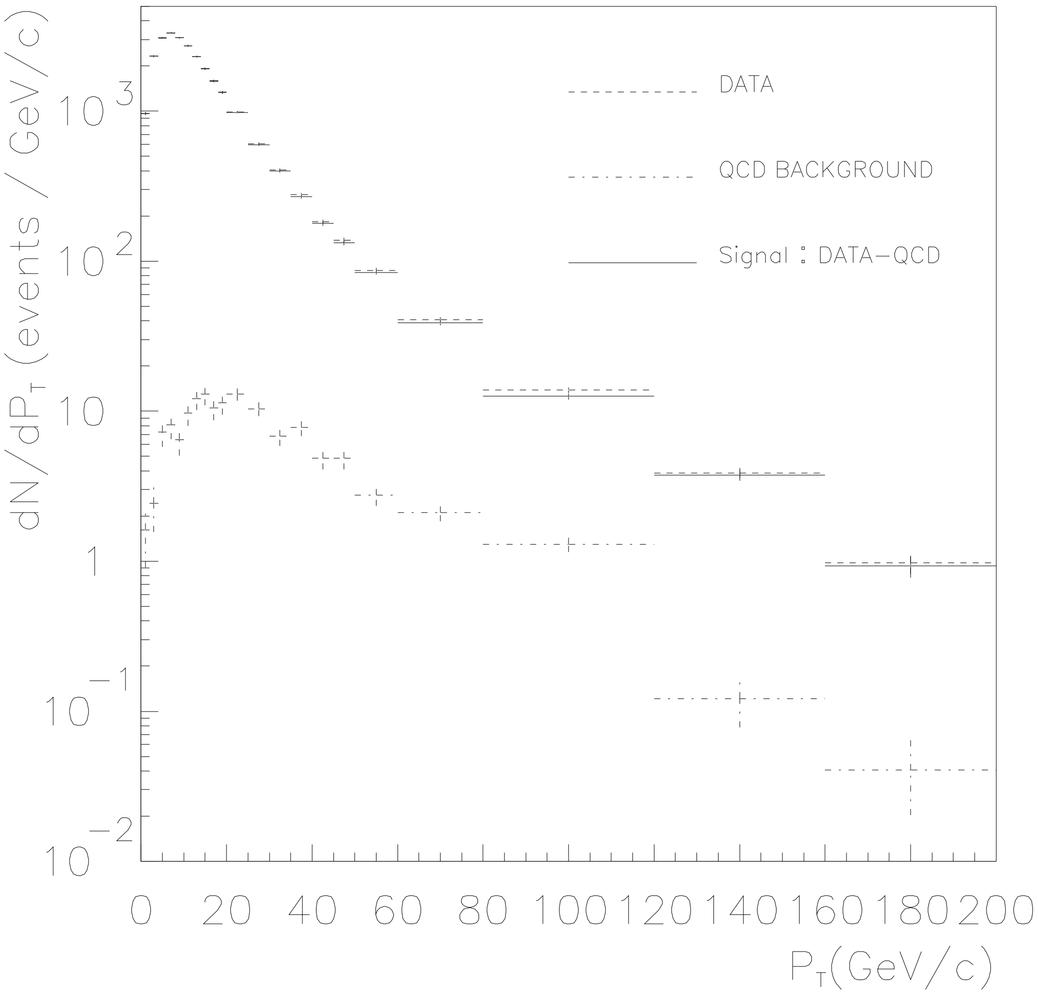

Figure 5.7: P_T^{rec} shapes of the data, QCD background and the “DATA-QCD”.

5.2 Single Boson Background

5.2.1 Introduction

In this section, we estimate backgrounds from the single boson processes of $W \to \tau\nu \to e\nu\nu\nu$ and $Z \to ee$.

A W produces an electron and $\not\!\!E_T$ by not only decaying directly into an electron and a neutrino but also decaying into a tau and a neutrino where the tau decays into an electron and neutrinos. In this process, the electron is softer than the one from $W \to e\nu$ process, because the electron shares the energy of the tau with two neutrinos. A P_T^{rec} shape in the $W \to \tau\nu \to e\nu\nu\nu$ process is the same as in the $W \to e\nu$ process.

We have the Z veto in the W event selection as described in Chapter 3; however, some Z events can still remain in our event sample with $\not\!\!E_T \geq 25$ GeV. If one of the Z electrons or a jet produced with a Z boson escapes through a crack in the detector, this can result in a large $\not\!\!E_T$.

We estimate the backgrounds from the above sources using Monte Carlo samples.

5.2.2 Monte Carlo Samples

We use PYTHIA Monte Carlo generator [22] with PHOTOS [23] which is a Monte Carlo for QED radiative corrections. The detector simulation is done using QFL [24]. The parameters used in running PYTHIA are given in Appendix A. We make data sets for some P_T regions in $W \to e\nu$, $W \to \tau\nu \to e\nu\nu\nu$, and $Z \to ee$ modes. Since we divide the Monte Carlo sample into narrow P_T bins, we do not need to consider the difference in P_T spectra between the Monte Carlo samples and the real data.

5.2.3 Method

We estimate a background ratio to the observed data bin by bin of the unsmeared (generation level) P_T^W. Since we know the relative production cross sections of the backgrounds to the signal from other measurements, we just need the relative cut efficiencies and acceptances of the background to the signal[1].

We apply all the event selection cuts on the backgrounds and the signal Monte Carlo data to calculate the efficiency and the acceptance of them respectively. We denote the efficiency×acceptance by R_{We} for $W \to e\nu$, $R_{W\tau}$ for $W \to \tau\nu \to e\nu\nu\nu$, and R_{Ze} for $Z \to ee$.

After the QCD background is subtracted from the data, the number of events in an unsmeared P_T bin should be:

$$N_{obs} = R_{We} \cdot N_{We} + R_{W\tau} \cdot N_{W\tau} + R_{Ze} \cdot N_{Ze} \tag{5.5}$$

where N_{We}, $N_{W\tau}$, and N_{Ze} are the numbers of $W \to e\nu$, $W \to \tau\nu \to e\nu\nu\nu$, and $Z \to ee$ events generated in $p\bar{p}$ collisions. Using the branching ratio of $\tau \to e\nu\nu$ ($BR = 17.83\%$ [25]) and the ratio $R_{W/Z} = \sigma B(p\bar{p} \to W \to e\nu)/\sigma B(p\bar{p} \to Z \to ee)$ at CDF ($R_{W/Z} = 10.90$ [26]), we have

$$N_{W\tau} = BR \cdot N_{We} \quad \text{and} \quad N_{Ze} = R_{W/Z}^{-1} \cdot N_{We} \ . \tag{5.6}$$

Then, Eq. 5.5 becomes

$$N_{obs} = \left(R_{We} + BR \cdot R_{W\tau} + R_{W/Z}^{-1} \cdot R_{Ze}\right) \cdot N_{We} \tag{5.7}$$

The number of $W \to e\nu$ events in the observed events is:

$$R_{We} \cdot N_{We} = \frac{1}{1 + \frac{R_{W\tau}}{N_{We}} \cdot BR + \frac{R_{Ze}}{R_{We}} \cdot R_{W/Z}^{-1}} \cdot N_{obs} \tag{5.8}$$

[1] We assume here that there is no noticeable difference in P_T shape between Z and W.

5.2.4 Results

Figs. 5.8– 5.10 show the second Z electrons of the background Monte Carlo events which passed the W selection cuts. In the left figures, ϕ and η distributions of the second electrons are shown using the information at the generation level. In the center figures, the invariant mass of the two electrons (vertical axis) and the number of electrons tagged as a second electron (horizontal axis) are shown using information after the detector simulation. The number of electrons tagged as a second electron are also shown in the right figures. The left figure for $P_T^Z < 35$ GeV/c shows that almost all second electrons go into crack regions. These electrons cause large $\not\!\!E_T$ and thus misidentification. The center figures in Figs. 5.8–5.10 show that mismeasurement of Z mass at the Z veto causes misidentification of Z as W, where a mismeasured electron or a jet is considered to produce high $\not\!\!E_T$.

Fig. 5.11 shows the $R_{W\tau}$, R_{Ze}, and R_{We} as a function of P_T, where the P_T is given from the generation level.

The result is shown in Fig. 5.12. The horizontal axis is the unsmeared P_T^W. The fraction of $W \to e\nu$ events in the observed events is around 97% for lower P_T events. This fraction begins to drop at $P_T \sim 50$ GeV/c and is about 85% in the high P_T region $140 < P_T < 200$ GeV/c. This fraction is applied to theoretical curves when comparing data to the theoretical predictions.

5.2.5 Systematic Uncertainty

In the calculation of this single boson backgrounds, the values from the Monte Carlo show up as ratios, thus uncertainties from the Monte Carlo are cancelled. To estimate the systematic uncertainty in the final P_T^W distribution from this single boson backgrounds, we shift each P_T bin of Fig. 5.12 randomly and independently according to each statistical error, which changes the final distribution. We calculate the standard deviation for each P_T bin of the final distribution and assign it as the systematic uncertainty. However, this uncertainty is negligible.

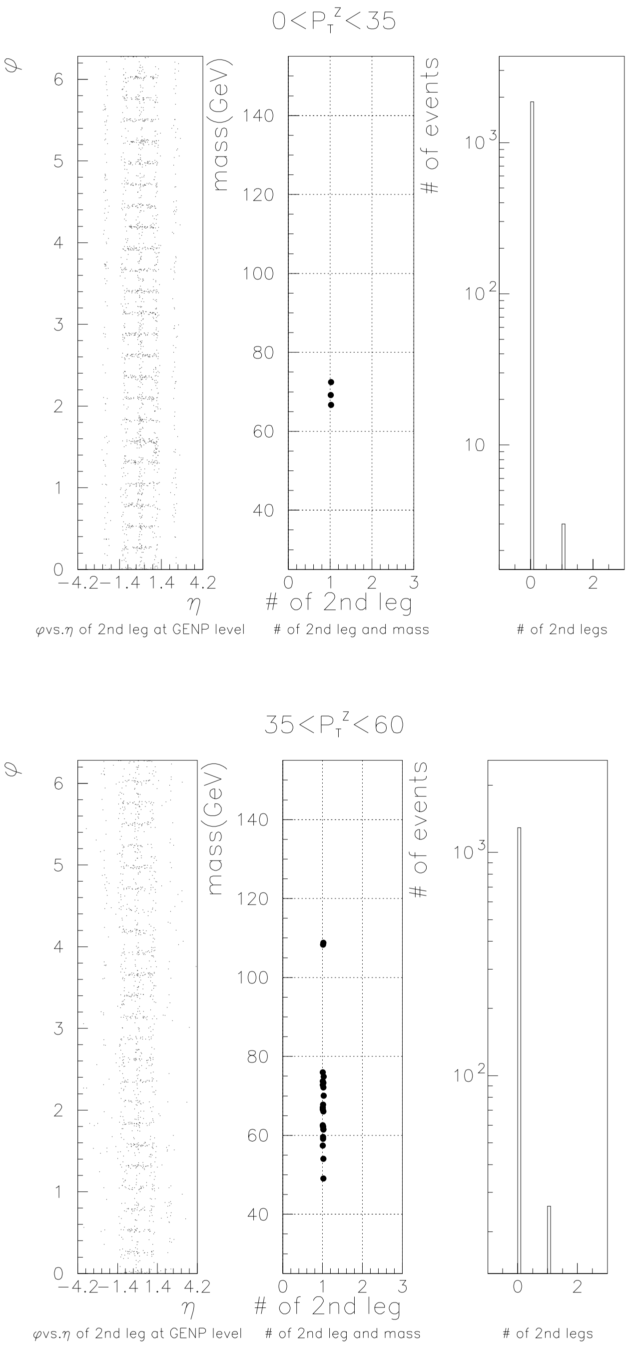

Figure 5.8: The Monte Carlo Z events passing the W selection cuts (TOP:$0 \leq P_T^Z < 35$ GeV/c, BOTTOM: $35 \leq P_T^Z < 60$ GeV/c). LEFT: ϕ and η distribution of the second electrons. The information used here is at the generation level. Most of the second electrons point to the region of the detector cracks. CENTER: Invariant mass vs. the number of "second" electrons. The information used here is at the detector level. If there are more than one "second" electrons, we use the one which makes a closest invariant mass to Z mass. The mass window for the Z removal is 76 to 106 GeV/c^2. RIGHT: The number of "second" electrons at the detector level.

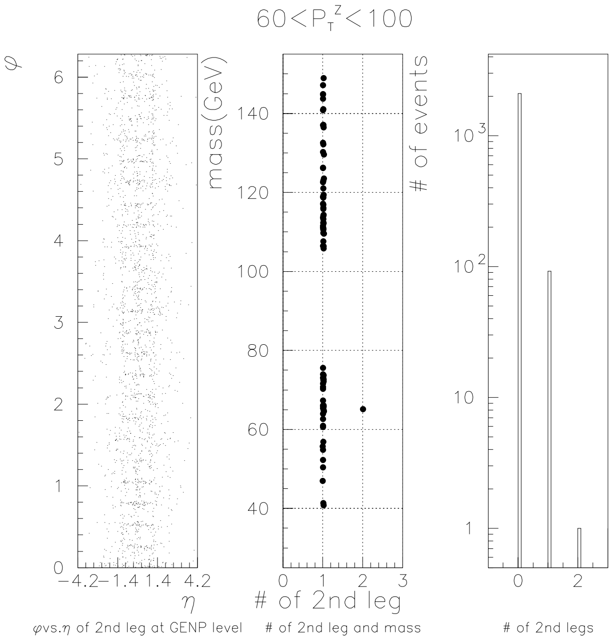

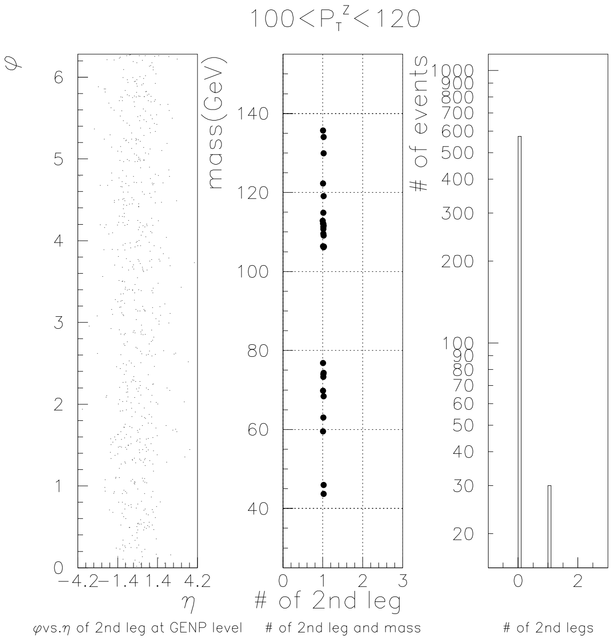

Figure 5.9: Same as Fig. 5.8. TOP: $60 \leq P_T^Z < 100$ GeV/c. BOTTOM: $100 \leq P_T^Z < 120$ GeV/c.

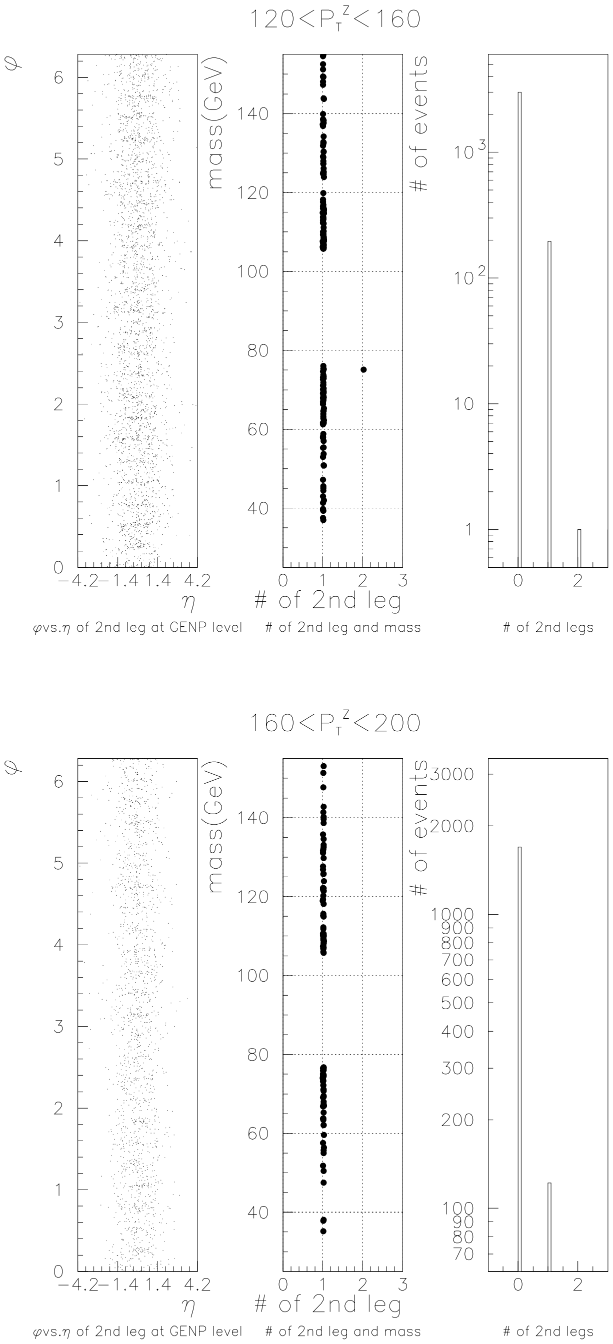

Figure 5.10: Same as Fig. 5.8. TOP: $120 \leq P_T^Z < 160$ GeV/c, BOTTOM: $160 \leq P_T^Z < 200$ GeV/c. The left and right figures show that there are events, the second electron of which does not point to the region of the detector cracks and is identified as the second electron. In these events, jets could cause the large $\not{E}_T$.

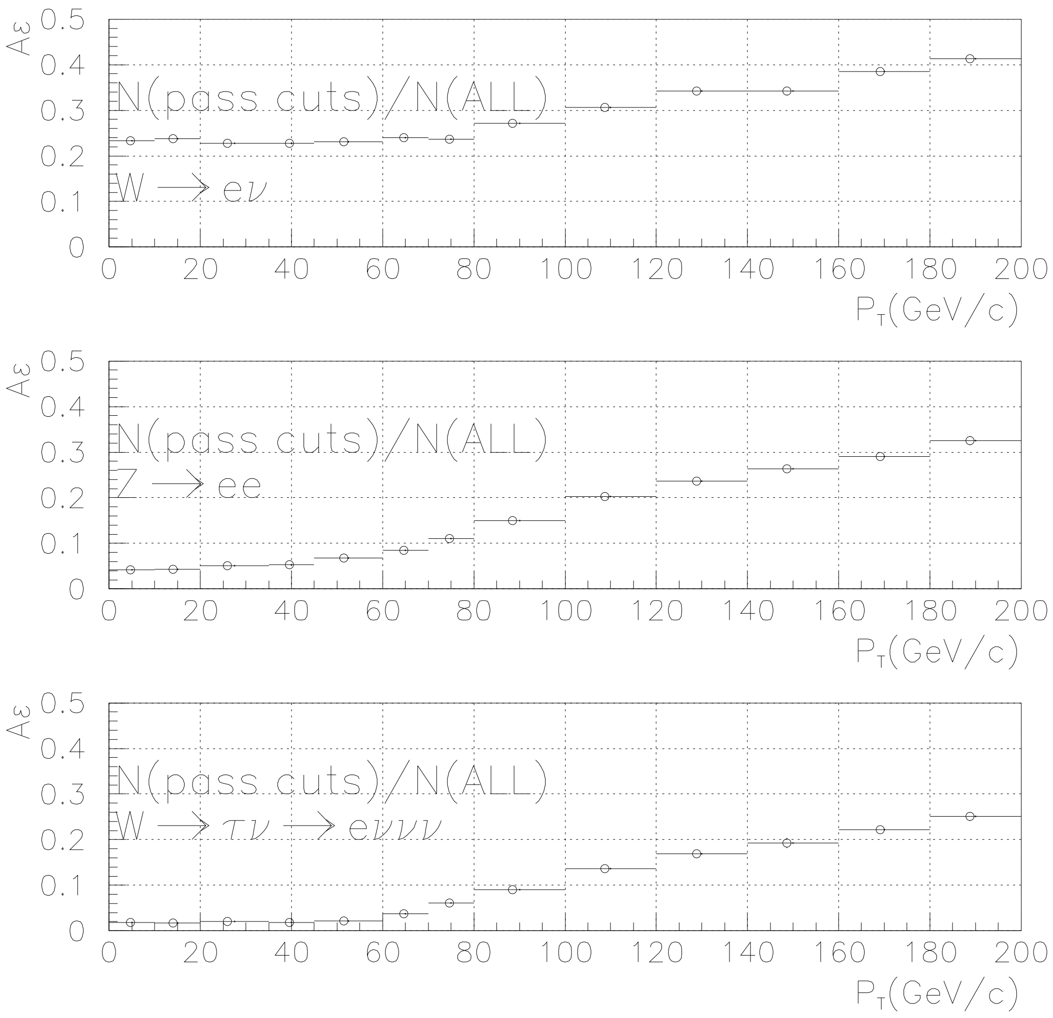

Figure 5.11: The acceptance×efficiency for $W \to e\nu$, $Z \to ee$, and $W \to \tau\nu \to e\nu\nu\nu$. The reason why the second bin for $W \to e\nu$ is relatively high is mentioned in the next chapter.

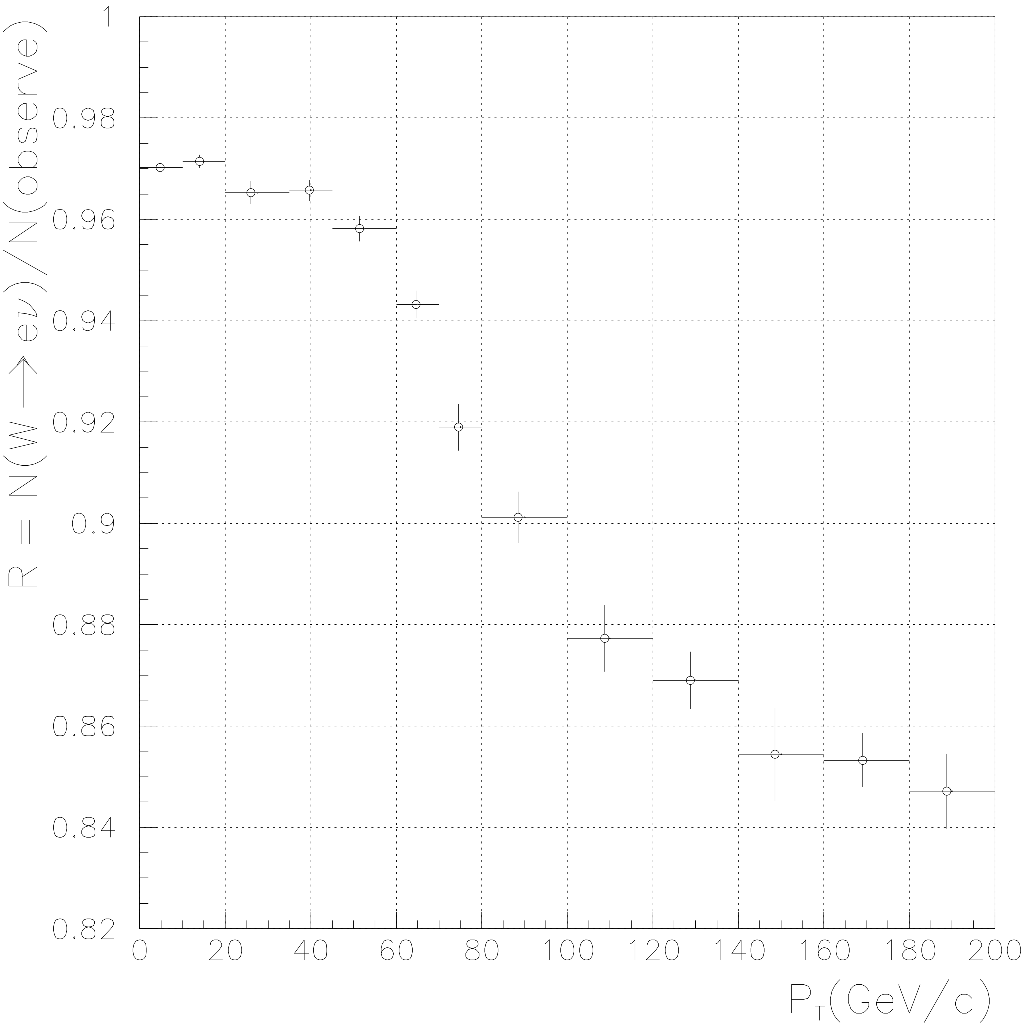

Figure 5.12: The fraction of the signal $W \to e\nu$ events in the observed events.

Chapter 6

Acceptance

6.1 Introduction

In this chapter, we describe how we determine the geometric and kinematic acceptances. The geometric acceptance is defined as the efficiency for the W electron to be in the fiducial volume of the CEM calorimeter. The kinematic acceptance is the efficiency for the electron in the fiducial volume of the CEM calorimeter to have E_T of at least 25.0 GeV and for the $\not{E}_T$ to be at least 25.0 GeV. We estimate the acceptances using a Monte Carlo event generator. We present the acceptances as a function of P_T^W.

6.2 Monte Carlo Sample

We generate the $W \rightarrow e\nu$ events using the PYTHIA event generator enhanced with PHOTOS radiative correction routines and QFL parametric detector simulation package. The nucleon parton distribution functions are CTEQ4M [27].

6.3 Geometric Acceptance

We first require that a W electron goes to the CEM. We use the information after the detector simulation.

Next, we require that the electron which passes the above requirement be in the fiducial volume.

We calculate the geometric acceptance as follows:

$$A_{CEM} = \frac{N_{CEM}}{N} \tag{6.1}$$

$$A_{fid} = \frac{N_{fid}}{N_{CEM}} \tag{6.2}$$

$$A_{geo} = A_{fid} \times A_{CEM} \tag{6.3}$$

where N is the total number of generated events with P_T^W in a certain P_T range, N_{CEM} is the number of events with the electron in the central region and N_{fid} is the number of events with the electron in the central fiducial volume.

6.4 Kinematic Acceptance

We require that E_T of the electron is ≥ 25 GeV. $\not{E}_T$ is also required to be ≥ 25 GeV. The calculation of the kinematic acceptance is as follows:

$$A_{E_T} = \frac{N_{E_T}}{N_{fid}} \tag{6.4}$$

$$A_{\not{E}_T} = \frac{N_{\not{E}_T}}{N_{E_T}} \tag{6.5}$$

$$A_{kin} = A_{\not{E}_T} \times A_{E_T} \tag{6.6}$$

where N_{E_T} stands for the number of events which have the electron with $E_T \geq 25$ GeV and pass the above geometric cuts, $N_{\not{E}_T}$ is the number of events which have both $E_T \geq 25$ GeV and $\not{E}_T \geq 25$ GeV.

6.5 Result of the Cuts

The results are shown in Figs. 6.1, 6.2, and 6.4.

The top figure in Fig. 6.1 shows the A_{CEM} as a function of P_T^W. Events with higher P_T^W tend to have an electron in the central region.

The bottom figure in Fig. 6.1 shows the geometric acceptance A_{geo}. The fiducial cut decreases the CEM acceptance by $\sim 10\%$. The geometric acceptance increases with P_T^W.

The top figure in Fig. 6.2 shows that the E_T cut efficiency for the events which passed the geometric cut increases P_T^W. The center figure in Fig. 6.2 shows that the $\not{E}_T$ efficiency cut for the events which passed both the E_T and the geometric cuts decreases with increasing P_T^W up to about 65 GeV/c, and then increases. This could be understood as follows by looking at event distributions in the $\not{E}_T$-E_T plane (Fig. 6.3). In lower P_T^W regions, the events are concentrated along the line of $\not{E}_T = E_T$ in the $\not{E}_T$-E_T plane, where events that are rejected by the $\not{E}_T$ cut do not remain much after the E_T cut is applied. As the P_T^W increases, the events spread in the direction of the line $\not{E}_T + E_T = constant$, which makes the acceptance decrease because some events spill over into the cut regions. Events with higher P_T^W tend to have E_T and $\not{E}_T$ above 25 GeV, thus the acceptance increases with increasing P_T^W. The bottom figure in Fig. 6.2 shows the kinematic acceptance.

The total acceptance is shown in Fig. 6.4. The acceptance is fitted to the following empirical formula:

$$F(P_T) = p_1 \cdot P_T^{p_2} + p_3 \cdot tanh\,(-p_4 \cdot P_T) + p_5 \tag{6.7}$$

6.6 Systematic Uncertainties

We use the fitting errors as the systematic uncertainties from this acceptance estimation to the final W boson P_T distribution $\frac{1}{N}\frac{dN}{dP_T}$. We shift each parameter randomly using its fitting error independently. Each "random acceptance curve" is applied to the $\frac{1}{N}\frac{dN}{dP_T}$ distribution. We calculate a standard deviation for each P_T bin as the systematic uncertainty.

We also check dependences on the PDF used. We test MRS-G [28] and CTEQ4HJ (Fig. 6.5). We apply the acceptance curves obtained using MRS-

G and CTEQ4HJ to the $\frac{1}{N}\frac{dN}{dP_T}$ distribution. However, these dependences on the PDF are negligibly small.

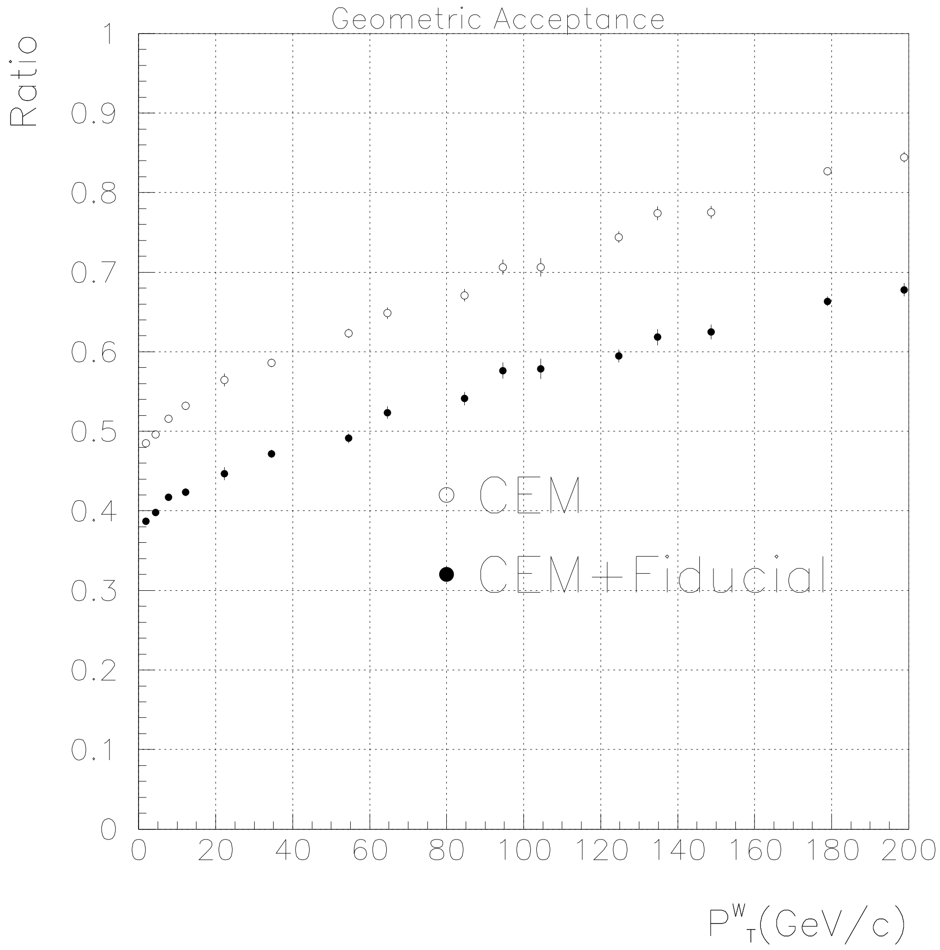

Figure 6.1: The efficiency of the CEM cut (open circle) and the geometric acceptance A_{geo} (CEM + Fiducial cuts, closed circle). The acceptance increases with increasing P_T^W.

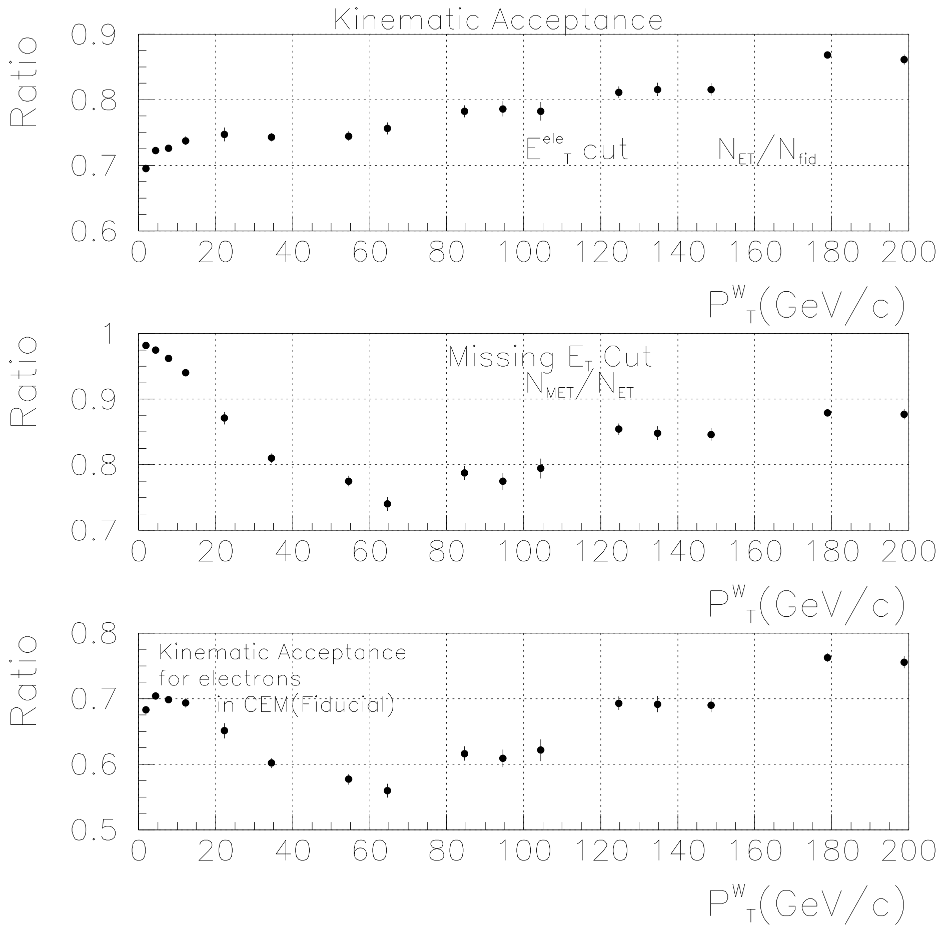

Figure 6.2: The kinematic acceptance. TOP: The E_T cut efficiency for electrons which passed the geometric cut. This efficiency increases with increasing P_T^W. MIDDLE: The $\not\!\!E_T$ cut efficiency for events which passed the geometric and E_T cuts. The number of events which are rejected by one of the two cuts, E_T or $\not\!\!E_T$ cut, increases with the increasing P_T up to P_T of around 65 GeV/c, thus the efficiency decreases. BOTTOM: The kinematic acceptance A_{geo} for events which passed the geometric cut.

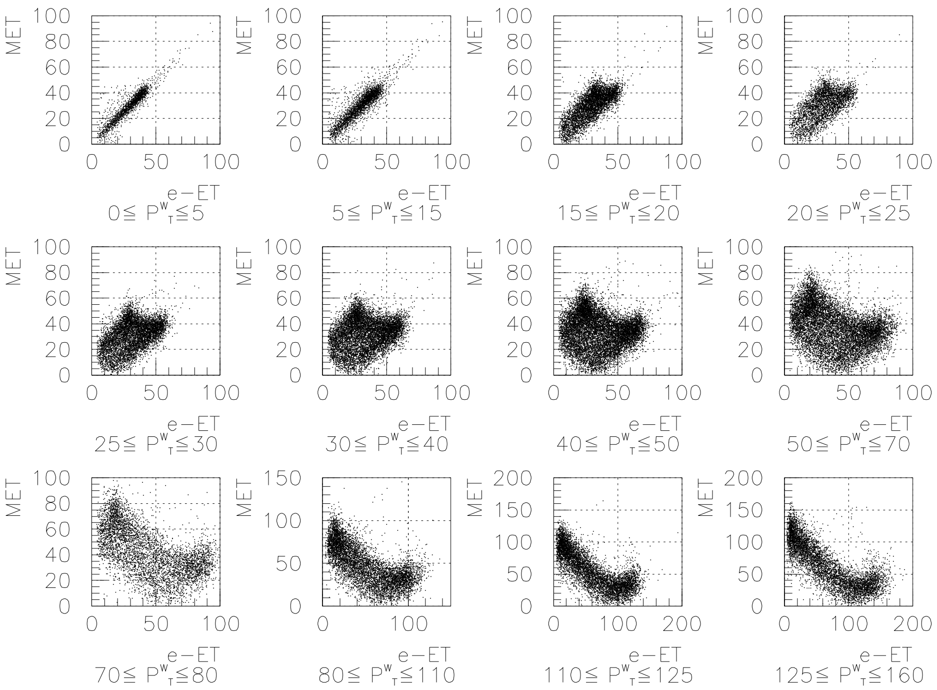

Figure 6.3: Scatter plots of the electron E_T vs. $\not\!\!E_T$, before the E_T and $\not\!\!E_T$ cuts. The distribution in the E_T and $\not\!\!E_T$ plane spreads with increasing P_T^W. In lower P_T^W regions, the events are concentrated on the line $\not\!\!E_T = E_T$. The increasing P_T^W spreads events on the line, $\not\!\!E_T + E_T = constant$, which decreases the acceptance. In higher P_T^W regions, many events have $\not\!\!E_T$ and E_T above 25 GeV, thus the acceptance increases again.

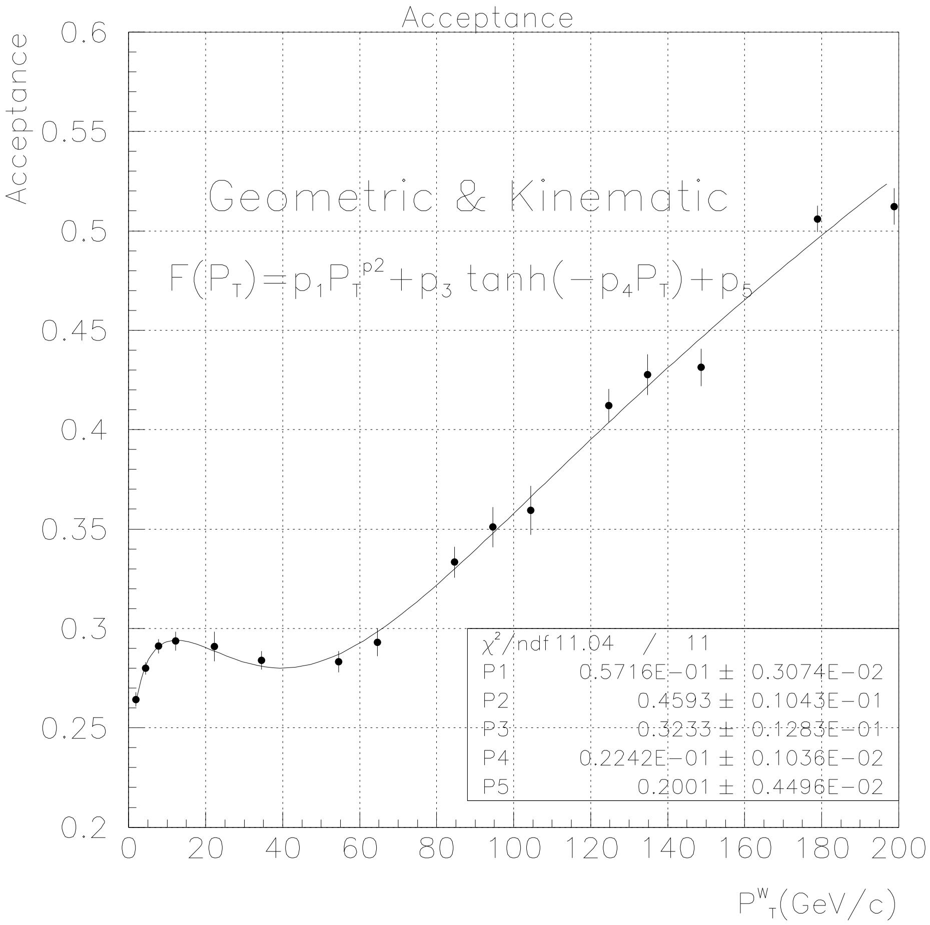

Figure 6.4: The total acceptance. The plots are fitted using an empirical formula $F(P_T) = p_1 \cdot P_T^{p_2} + p_3 \cdot tanh(-p_4 \cdot P_T) + p_5$.

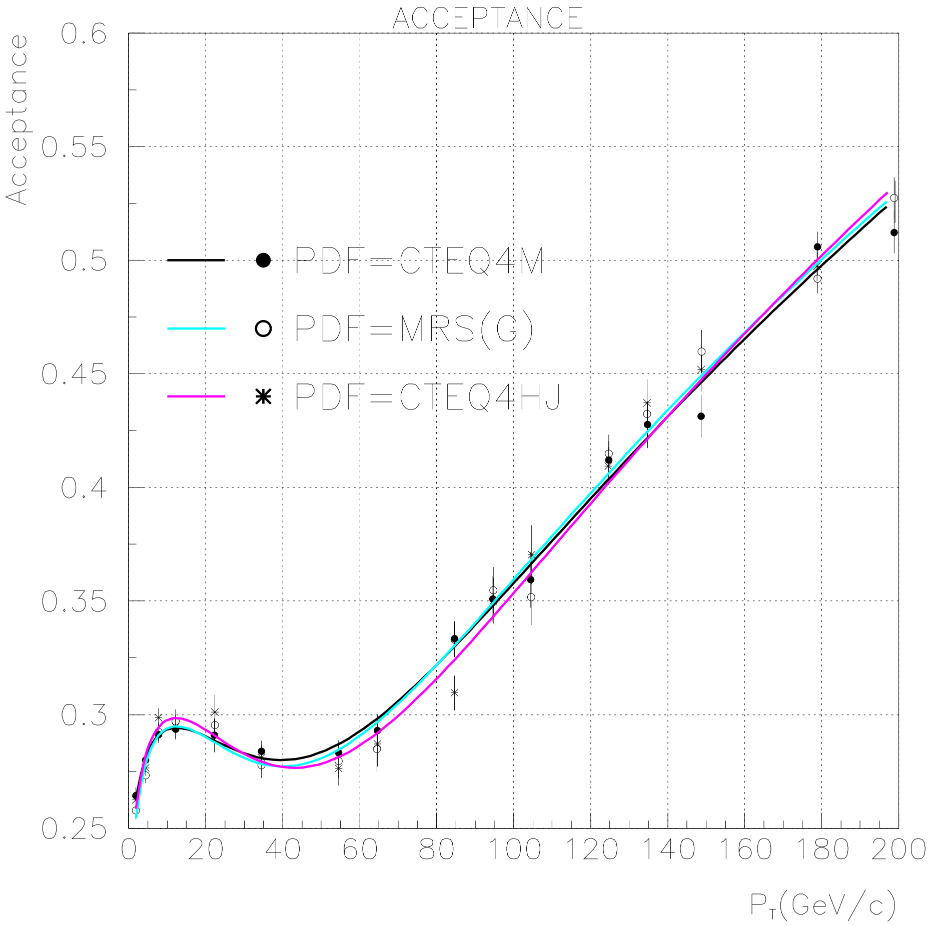

Figure 6.5: The uncertainty in the acceptance estimation due to the PDF.

Chapter 7

The Smearing Model

7.1 Introduction

In this chapter, we estimate the detector resolution of the recoil P_T using real Z data as a control sample. In the following chapter, we smear theory curves using our smearing model which we determine in this section and then compare them with our data.

The P_T^{rec} in a W event is calculated using energies of all measurable particles except the electron from W:

$$\vec{P_T^{rec}} = \sum \vec{E_T^{jet}} + K \cdot \vec{E_T^{unc}} \quad . \tag{7.1}$$

The E_T^{jet} and E_T^{unc} are corrected by the methods previously described in Sections 4.1 and 4.2, respectively. The shape of this P_T^{rec} distribution is, however, still smeared due to detector resolutions.

We estimate this detector resolution effect using real Z data by comparing the P_T^{rec} in Z events with the P_T of the two electrons (P_T^{ee}). We assume that the uncertainty in P_T^{ee} measurement is negligible.

7.2 Control Sample

We use the inclusive Z data sample with the same selection criteria used for the E_T^{unc} correction described in Section 4.2 except the jet veto cut; we include the events with jets. In each event, the P_T^{rec} is broken into two components (Fig. 7.1): one ($P_\perp^{rec}$) perpendicular to the Z boson P_T ($P_T^Z = P_T^{ee}$) and the other ($P_\parallel^{rec}$) parallel to it. Fig. 7.2 shows that the correlation between $P_T^{ee} + P_\parallel^{rec}$ and $P_\perp^{rec}$ is negligible.

We classify events into 8 bins according to the size of $P_T^Z = P_T^{ee}$. We then make two types of plots, one is $P_T^{ee} + P_\parallel^{rec}$, and the other is $P_\perp^{rec}$.

The results are shown in Figs. 7.3 and 7.4. We fit these distributions to the function:

$$F(x) = p_1 \cdot exp\left(-\sqrt{\left(\frac{x - p_3}{p_2}\right)^2 + 1}\right) \quad . \tag{7.2}$$

The parameter p_2 corresponds to the width of the distribution. The parameter p_3 is the mean of the distribution and fixed to 0 in fitting the $P_\perp^{rec}$ distribution.

We plot the widths (p_2) of the $P_T^{ee} + P_\parallel^{rec}$ and $P_\perp^{rec}$ distributions as a function of P_T^{ee} in Figs. 7.5 and 7.6. We find that the width of the distribution increases with increasing P_T^{ee}. These two plots are fitted to the function,

$$F(P_T) = \sqrt{p_1 \cdot P_T} + p_2 \quad . \tag{7.3}$$

Fig. 7.7 shows that the mean of the $P_T^{ee} + P_\parallel^{rec}$ distribution shifts with P_T^{ee}. This shift arises because the E_T^{unc} correction factor (K-factor) depends on P_T^{ee}. We determined $K = 2.0$ for the whole event sample in Chapter 4, because we can not measure $P_T^{e\nu}$ event by event like P_T^{ee}. We include this dependence into this smearing model. This plot is fitted using the following empirical form:

$$F(P_T) = tanh\,(p_1 \cdot P_T - p_2) \cdot \sqrt{p_3 \cdot P_T} \quad . \tag{7.4}$$

However, the result of the fit has a little problem in the lowest P_T^{ee} region; for P_T less than 0.4 GeV/c, the fit result $F(P_T)$ becomes larger than P_T, that is,

$$\left\langle P_T^{ee} + P_{\parallel}^{rec} \right\rangle = \left\langle P_T^{ee} \right\rangle + \left\langle P_{\parallel}^{rec} \right\rangle \geq \left\langle P_T^{ee} \right\rangle \quad . \tag{7.5}$$

This means that the $P_{\parallel}^{rec}$ of the whole events directs in the same direction as P_T^{ee}, which is unnatural. When we smear the theory curves in the next chapter, we thus require $F(P_T) < P_T$ by the following:

$$F(P_T)' = min(a \cdot P_T^{ee} \, , \, tanh(b \cdot P_T - c) \cdot \sqrt{d \cdot P_T}) \quad . \tag{7.6}$$

There is no particular reason for the form $a \cdot P_T^{ee}$. The constant a is quite arbitrary and should only be $0 < a < 1$. In this analysis, we use $a = 0.5$ which makes $F(P_T) = P_T$ at $P_T = 1.2$ GeV/c[1].

7.3 Systematic Errors

In the above we have determined three functions of P_T^W: $F(P_T)_{\parallel}$, $F(P_T)_{\perp}$, and $F(P_T)_{mean}$. Using these curves, we study systematic errors in the final W boson distribution $\frac{1}{N}\frac{dN}{dP_T}$ arising from the uncertainty of our smearing model. Each curve has a finite fitting error. First, we shift one of the three curves by its fitting error, next we carry the smearing procedure, then we measure the difference between the two distributions. The same procedure is repeated for other curves. Finally, the systematic error in the final distribution from the smearing model is calculated as the quadrature sum of the differences.

7.4 Summary

The detector resolution of the P_T^{rec} is determined using real Z data as a control sample. The resolution is evaluated in two components, one perpendicular to the boson P_T and the other parallel to it. The dependence of the width of the resolution distribution on P_T^W is determined for each component, and the shift of the center of the resolution distribution is determined

[1] There is not big difference in the result between $a = 0.5$ and $a = 0.7$.

for the parallel component. We use the fitting errors in the above processes as the uncertainty due to the smearing model. The parameters we get are shown in Figs. 7.5 ~ 7.7.

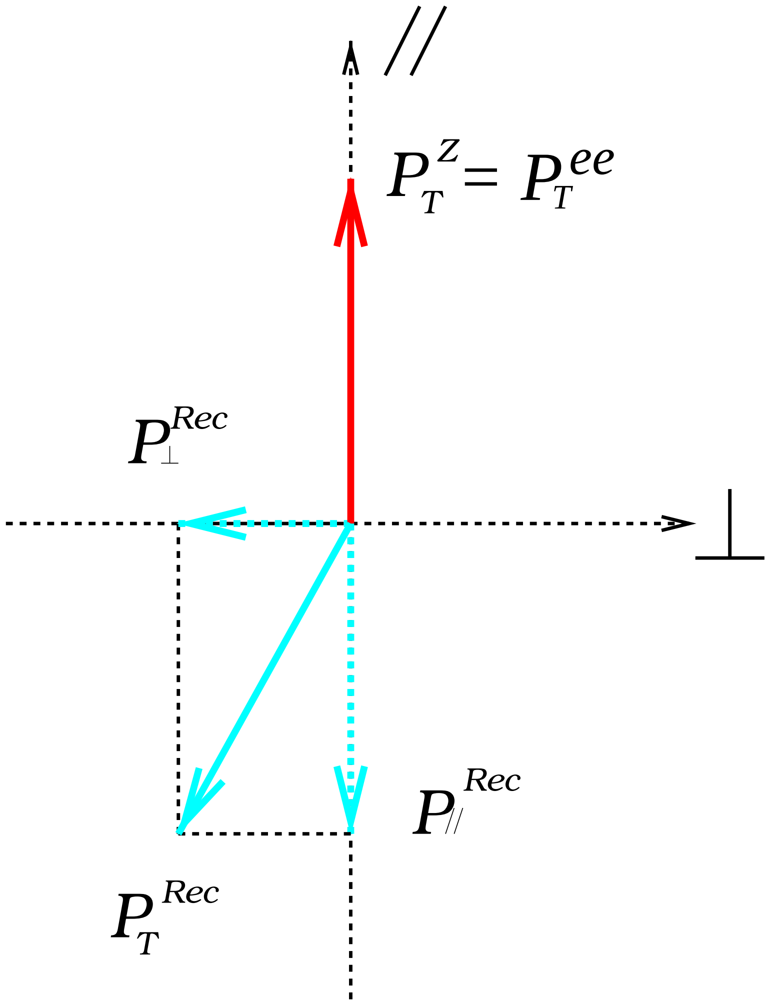

Figure 7.1: The definition of the $P_\perp^{rec}$ and $P_\parallel^{rec}$.

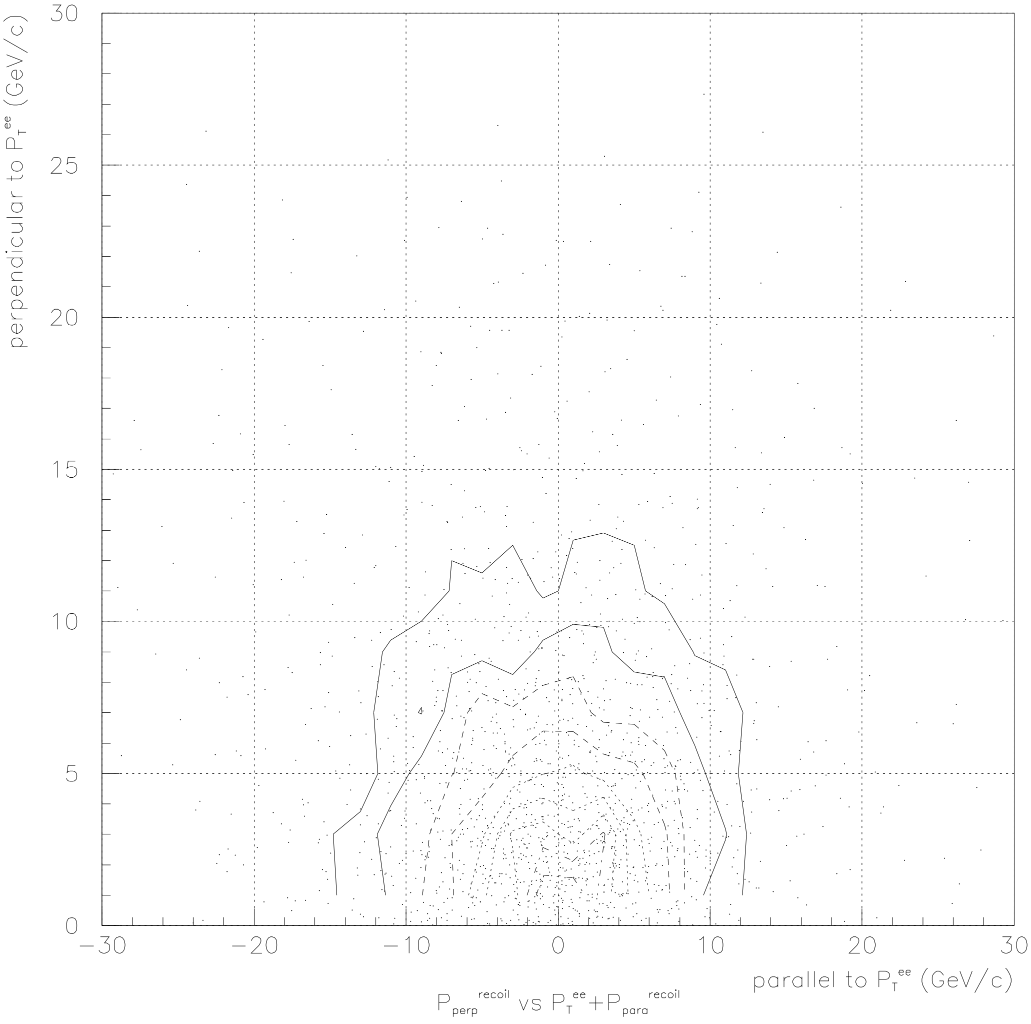

Figure 7.2: $P_{\perp}^{rec}$ vs. $P_T^{ee} + P_{\parallel}^{rec}$. The correlation between them is negligible.

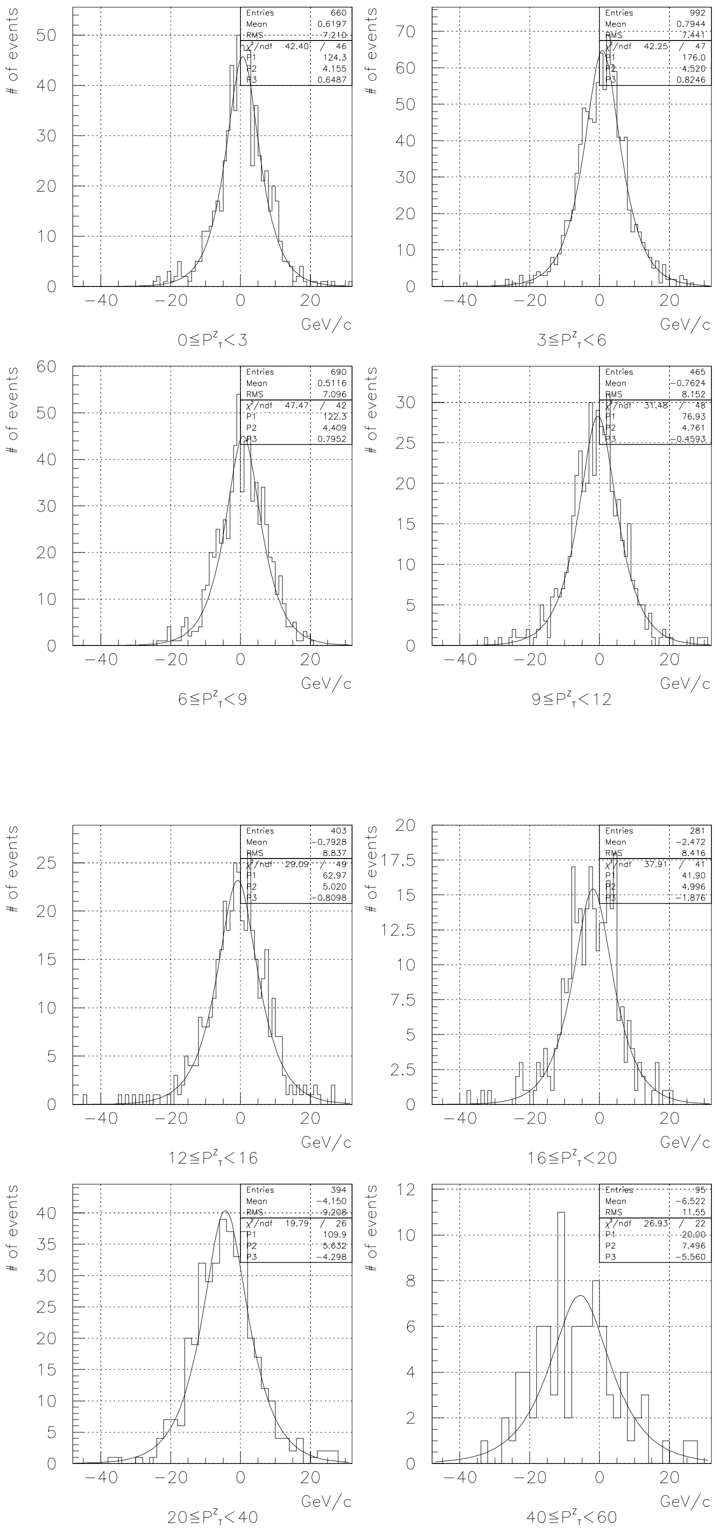

Figure 7.3: The $P_T^{ee} + P_{\parallel}^{rec}$ distributions. The mean of the distribution (p_3) shifts with P_T^{ee}.

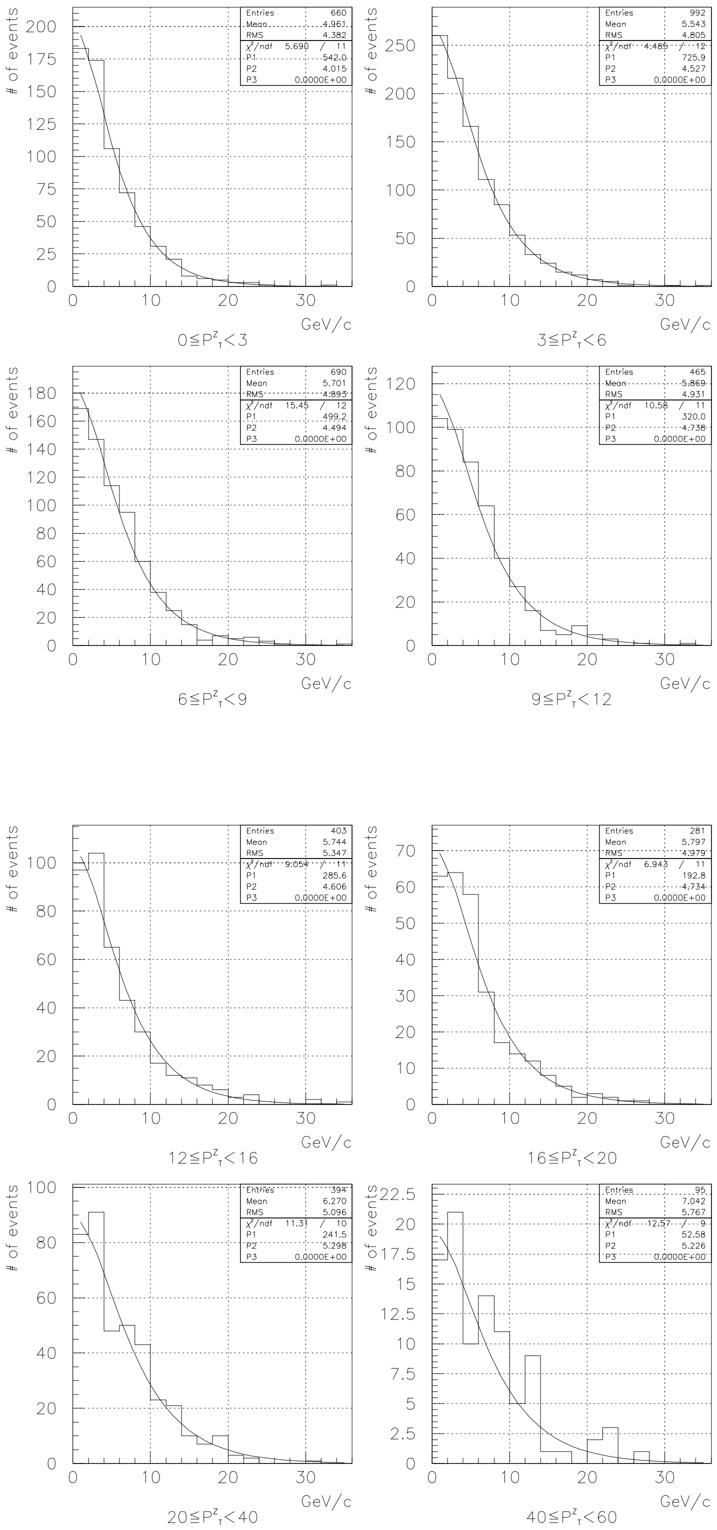

Figure 7.4: The $P_{\perp}^{rec}$ distributions. The width of the distribution (p_2) increases with P_T^{ee}. The parameter p_3 is fixed to 0.

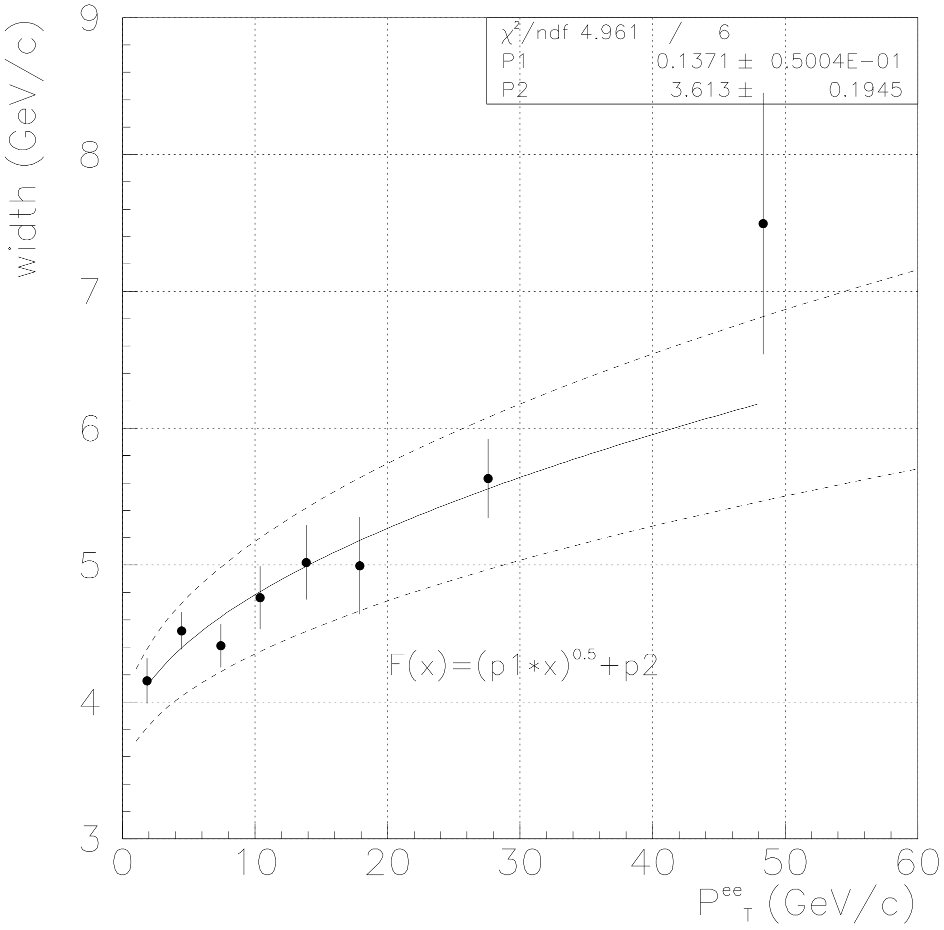

Figure 7.5: The widths (p_2) of the $P_T^{ee} + P_{\parallel}^{rec}$ distribution vs. P_T^{ee}. The width is proportional to $\sqrt{P_T^{ee}}$.

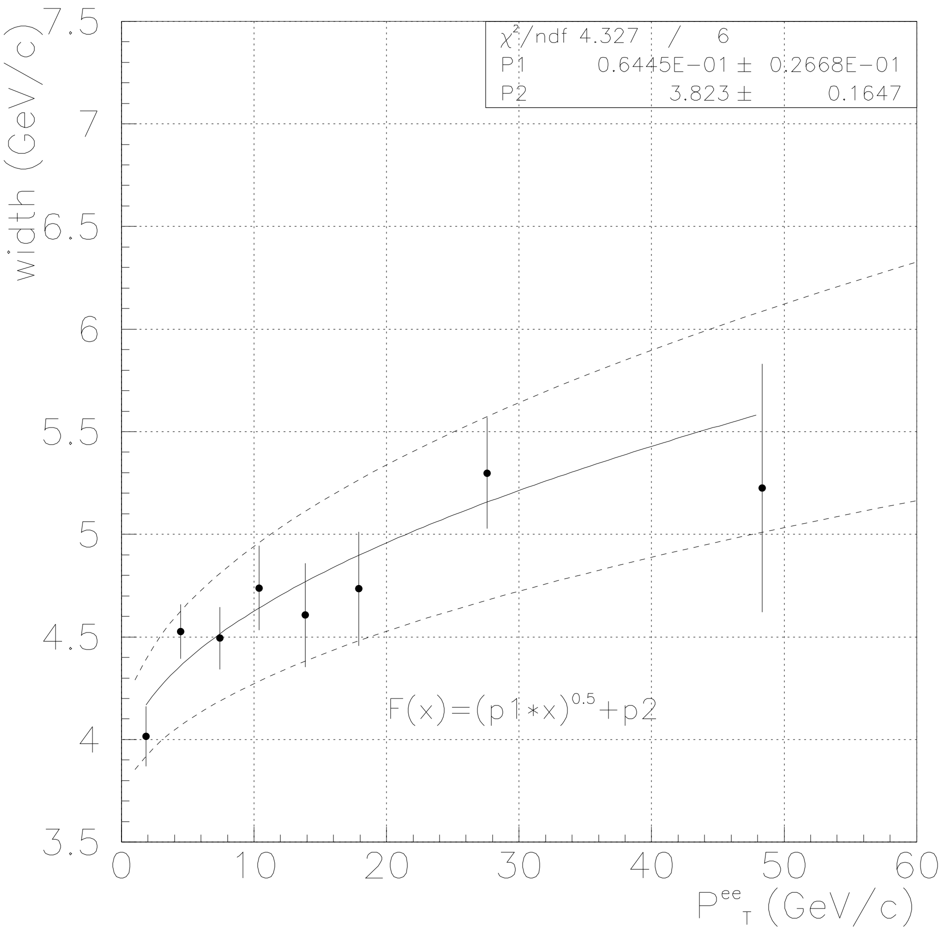

Figure 7.6: The widths (p_2) of the $P_{\perp}^{rec}$ distribution vs. P_T^{ee}. The width is proportional to $\sqrt{P_T^{ee}}$.

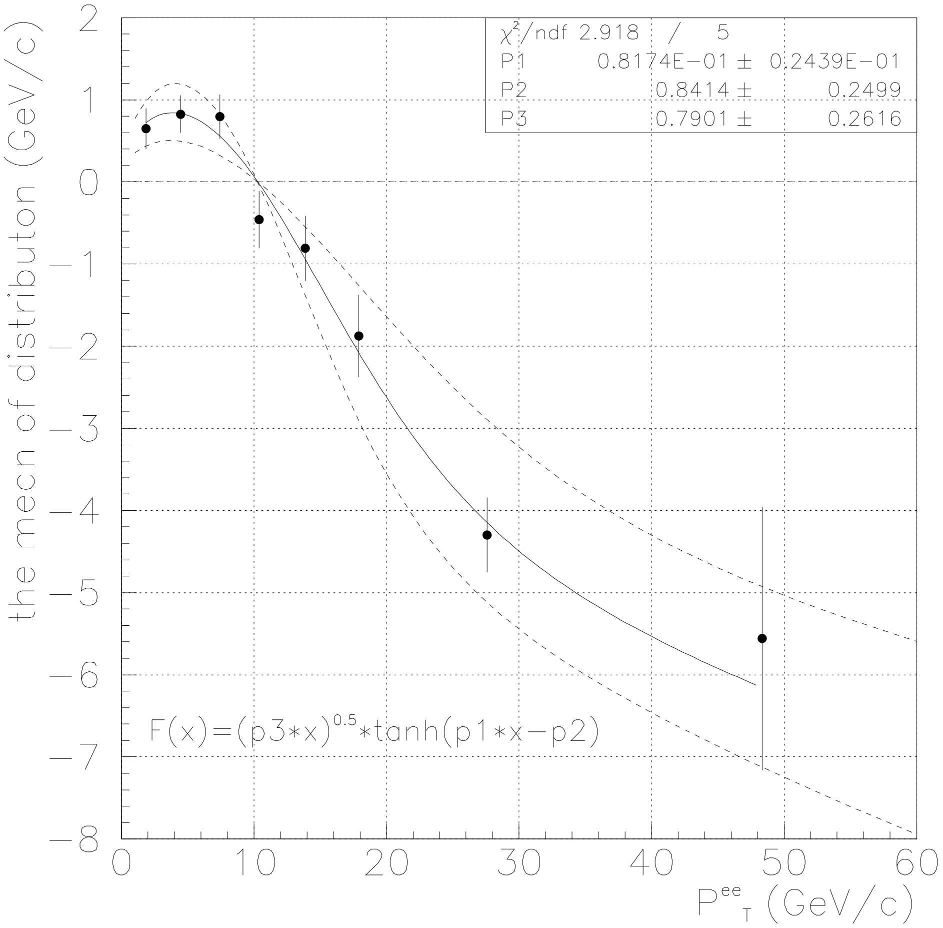

Figure 7.7: The mean of the $P_T^{ee} + P_{\parallel}^{rec}$ distribution as a function of P_T^{ee}.

Chapter 8

Comparing Data with Theory

8.1 Introduction

In this chapter, we compare our data to two theory curves: calculated by the b-space and q_T-space formalisms, as mentioned in Chapter 1.

We can not measure P_T^W distribution directly and thus measure P_T^{rec} whose shape is smeared, as described in Chapters 4 and 7. In this study, we do not unfold our data distribution as CDF did at the previous analysis using 1988–1989 collider run, because the unfolding procedure[29] is sensitive to the choice of the fitting function. Instead of unfolding the data, we smear the theoretical curves according to the detector resolution studied in Chapter 7.

8.2 Data

As described in the previous chapters, the W events are selected by requiring an isolated electron with high E_T and large $\not\!\!E_T$. The P_T^{rec} distribution of these events is presented after the jet energy correction and the unclustered energy correction. From that P_T^{rec} distribution, the shape of QCD background is subtracted. We can not subtract the backgrounds of $W \to \tau\nu$ and $Z \to ee$ from the data, because we do not know P_T^{rec} distributions of these backgrounds; we determine the fraction of the backgrounds in the data as a function of P_T^W. Therefore we present theoretical curves with the boson backgrounds for comparison.

8.3 Theory

We compare the data to the theoretical curves calculated by the b-space and q_T-space formalisms. The theoretical distributions of P_T^W is re-shaped into "P_T^{rec}" distributions in the following steps:

- multiplying the detector acceptance,
- adding the shapes of the boson backgrounds,
- smearing by the detector smearing model.

As described in the previous chapters, the above three procedures are given as functions of P_T^W.

8.4 Systematic Uncertainties

The systematic uncertainties from the following items are estimated as described in the previous chapters. We summarize them here.

- QCD background
  The scale factor $R = 1.62$ has the systematic uncertainty of 35%. The shape of the QCD background is determined using the real data whose size is 330. The statistical uncertainty from this number is also counted as a systematic uncertainty of the final distribution, $\frac{1}{N}\frac{dN}{dP_T}$.
- Single boson backgrounds
  The fraction of the boson background events in the data shown in Fig. 5.12 has a statistical uncertainty in each P_T bin. We shift randomly each P_T bin independently, which changes the final distribution. We

repeat this shift 100 times. We calculate the standard deviations at each P_T bin of the final distribution.

- Acceptance

  The ratio shown in Fig. 6.4 has five fitting parameters with errors. We shift randomly all parameters independently according to the errors, which also changes the final distribution. We repeat this shift 100 times and calculate the standard deviations at each P_T bin of the final distribution. We also check dependencies on the PDF used. The results with two other PDFs, CTEQ4HJ and MRS-G, are shown in Fig. 6.5.

- Smearing Model

  The smearing model involves three curves with fitting errors. We check the shift of the final distribution if one of the curves changes by the error. We assume here that three curves cause the systematic uncertainties independently.

8.5 Comparing Data with Theory

Theoretical distributions which are smeared by the above procedures and real data are given in Table 8.3 and shown in Figs 8.3 and 8.4. Top figures show the P_T^W distributions in lower P_T regions using the b-space (Fig. 8.3) and q_T-space (Fig. 8.4) formalisms, and bottom figures show the same distributions up to $P_T = 200$ GeV/c in log scale. The error bars with the data points are the sum in quadrature of the statistical uncertainties and the systematic uncertainties from the QCD background estimation. The systematic uncertainties from the single boson background estimation, the acceptance estimation, and the smearing model are shown as bands with the theoretical distributions. Systematic uncertainties in the error bands are shown in Tables 8.1, 8.2 , Figs. 8.1, and 8.2.

P_T bins (GeV/c)	Boson (%)	Acceptance (%)	Smearing Model (+/−) (%)
0-2	±0.08	±1.81	5.53/9.12
2-4	±0.08	±1.70	6.55/4.78
4-6	±0.08	±1.53	5.06/3.87
6-8	±0.08	±1.30	2.72/2.54
8-10	±0.07	±1.06	2.54/1.83
10-12	±0.07	±0.81	2.15/2.29
12-14	±0.07	±0.64	1.75/3.62
14-16	±0.06	±0.52	2.23/4.70
16-18	±0.07	±0.52	3.44/6.15
18-20	±0.07	±0.61	3.88/4.63
20-25	±0.07	±0.93	4.09/4.41
25-30	±0.09	±1.55	4.99/2.23
30-35	±0.12	±2.21	6.01/4.75
35-40	±0.14	±2.86	4.54/9.79
40-45	±0.13	±3.55	7.06/5.83
45-50	±0.13	±4.17	4.66/8.71
50-60	±0.15	±4.92	7.63/6.76
60-80	±0.17	±5.93	6.49/7.15
80-120	±0.26	±6.60	4.76/5.78
120-160	±0.39	±6.57	5.92/4.32
160-200	±0.58	±6.40	5.20/6.20

Table 8.1: The systematic uncertainties for the re-shaped theoretical prediction (the b-space formalism). The uncertainties are from the boson background estimation, acceptance estimation, and smearing model.

Figs. 8.5 and 8.6 show the residual distributions, $\frac{DATA-THEORY}{THEORY}$. The statistical uncertainties are shown as error bars and the all systematic uncertainties are shown as bands. The reduced χ^2's between the data and theoretical curves are 1.05 (the q_T-space formalism; 0∼120 GeV/c, 19 points), 1.71 (the q_T-space formalism; 0∼200 GeV/c, 21 points), 1.85 (the b-space formalism; 0∼120 GeV/c, 19 points), and 2.49 (the b-space formalism; 0∼200 GeV/c, 21 points).

The theoretical predictions by the q_T-space and b-space formalisms provide reasonable description of the data at low P_T.

There appears to be discrepancies at high P_T although the experimental

P_T bins (GeV/c)	Boson (%)	Acceptance (%)	Smearing Model (+/−) (%)
0-2	±0.06	±1.58	5.72/9.01
2-4	±0.06	±1.47	6.87/4.77
4-6	±0.05	±1.31	5.53/3.69
6-8	±0.05	±1.10	3.05/2.24
8-10	±0.05	±0.89	2.65/1.44
10-12	±0.05	±0.68	2.24/2.03
12-14	±0.05	±0.55	1.73/3.68
14-16	±0.05	±0.47	2.42/4.64
16-18	±0.05	±0.52	3.98/6.44
18-20	±0.06	±0.65	4.68/5.08
20-25	±0.07	±1.01	5.19/4.87
25-30	±0.10	±1.69	6.20/2.83
30-35	±0.14	±2.37	6.81/5.12
35-40	±0.16	±3.04	5.02/9.91
40-45	±0.15	±3.72	7.78/5.72
45-50	±0.15	±4.34	5.13/8.64
50-60	±0.15	±5.10	7.99/6.32
60-80	±0.16	±6.14	6.19/6.27
80-120	±0.27	±6.78	4.56/5.03
120-160	±0.39	±6.80	6.25/4.16
160-200	±0.57	±6.62	5.49/6.01

Table 8.2: The systematic uncertainties for the re-shaped theoretical prediction (the q_T-space formalism). The uncertainties are from the boson background estimation, acceptance estimation, and smearing model.

errors are large.

P_T bins (GeV/c)	N_{data}	$\frac{1}{N}\frac{dN}{dP_T}$ (GeV/c)$^{-1}$	Stat (GeV/c)$^{-1}$	Sys (GeV/c)$^{-1}$	b-space (GeV/c)$^{-1}$	q_T-space (GeV/c)$^{-1}$
0-2	1924	0.01588	0.00036	0.00002	$0.01493^{+0.00089}_{-0.00137}$	$0.01360^{+0.00079}_{-0.00126}$
2-4	4659	0.03847	0.00056	0.00003	$0.03986^{+0.00280}_{-0.00199}$	$0.03636^{+0.00246}_{-0.00184}$
4-6	6166	0.05085	0.00065	0.00006	$0.05336^{+0.00303}_{-0.00209}$	$0.04897^{+0.00259}_{-0.00204}$
6-8	6652	0.05485	0.00067	0.00006	$0.05671^{+0.00184}_{-0.00142}$	$0.05257^{+0.00158}_{-0.00150}$
8-10	6167	0.05087	0.00065	0.00005	$0.05328^{+0.00149}_{-0.00090}$	$0.05014^{+0.00138}_{-0.00106}$
10-12	5463	0.04500	0.00061	0.00007	$0.04664^{+0.00109}_{-0.00100}$	$0.04477^{+0.00103}_{-0.00109}$
12-14	4627	0.03805	0.00056	0.00009	$0.03962^{+0.00072}_{-0.00147}$	$0.03886^{+0.00073}_{-0.00143}$
14-16	3860	0.03169	0.00051	0.00009	$0.03254^{+0.00080}_{-0.00152}$	$0.03274^{+0.00075}_{-0.00155}$
16-18	3180	0.02611	0.00047	0.00008	$0.02648^{+0.00106}_{-0.00171}$	$0.02731^{+0.00095}_{-0.00169}$
18-20	2676	0.02193	0.00043	0.00008	$0.02139^{+0.00101}_{-0.00110}$	$0.02259^{+0.00089}_{-0.00106}$
20-25	4951	0.01616	0.00023	0.00008	$0.01508^{+0.00080}_{-0.00075}$	$0.01654^{+0.00069}_{-0.00075}$
25-30	3038	0.009874	0.000182	0.000067	$0.009298^{+0.000598}_{-0.000307}$	$0.01067^{+0.00056}_{-0.00029}$
30-35	2026	0.006586	0.000149	0.000047	$0.006113^{+0.000441}_{-0.000345}$	$0.007229^{+0.000463}_{-0.000379}$
35-40	1385	0.004451	0.000123	0.000052	$0.004253^{+0.000250}_{-0.000441}$	$0.005129^{+0.000275}_{-0.000523}$
40-45	917	0.00295	0.00010	0.00004	$0.00288^{+0.00025}_{-0.00020}$	$0.00353^{+0.00028}_{-0.00024}$
45-50	689	0.00220	0.00009	0.00004	$0.00210^{+0.00014}_{-0.00020}$	$0.00260^{+0.00016}_{-0.00025}$
50-60	870	0.00139	0.00005	0.00002	$0.00133^{+0.00013}_{-0.00011}$	$0.00163^{+0.00015}_{-0.00014}$
60-80	817	0.000641	0.000024	0.000014	$0.000616^{+0.000054}_{-0.000054}$	$0.000716^{+0.000063}_{-0.000067}$
80-120	554	0.000208	0.000010	0.000008	$0.000182^{+0.000015}_{-0.000015}$	$0.000184^{+0.000015}_{-0.000016}$
120-160	155	0.0000621	0.0000052	0.0000014	$0.0000395^{+0.0000037}_{-0.0000032}$	$0.0000391^{+0.0000035}_{-0.0000031}$
160-200	39	0.000015	0.000003	0.000001	$0.000010^{+0.000001}_{-0.000001}$	$0.000010^{+0.000001}_{-0.000001}$

Table 8.3: The P_T^{rec} distribution of W bosons corresponding to Figs. 8.3 and 8.4. The column labeled "Stat" shows the statistical uncertainty; "Sys" shows the systematic uncertainty from QCD background estimation; "b-space" and "q_T-space" show the smeared predictions with the systematic uncertainties from the single boson background estimation, the acceptance estimation, and the detector smearing model.

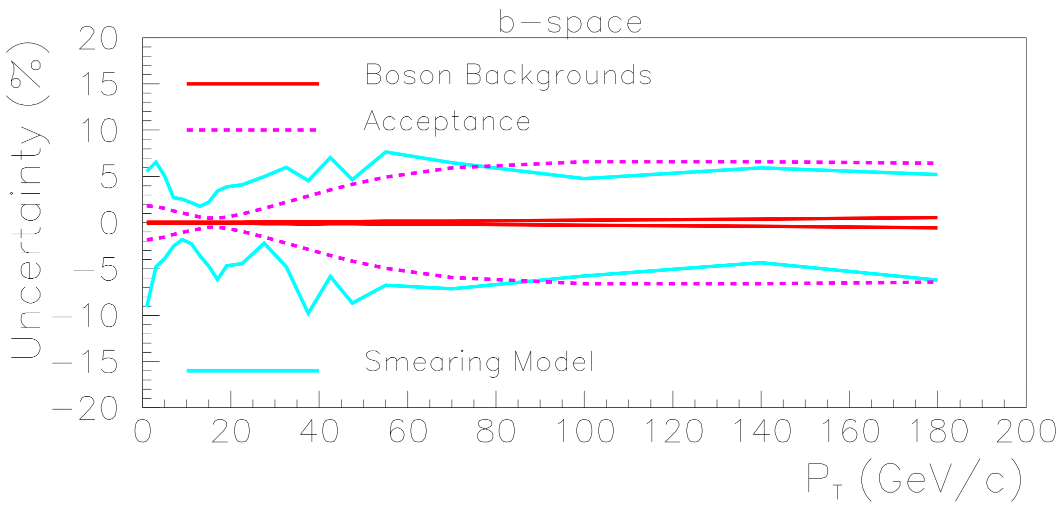

Figure 8.1: The systematic uncertainties for the re-shaped theoretical prediction (the b-space formalism). The uncertainties are from the boson background estimation, acceptance estimation, and smearing model.

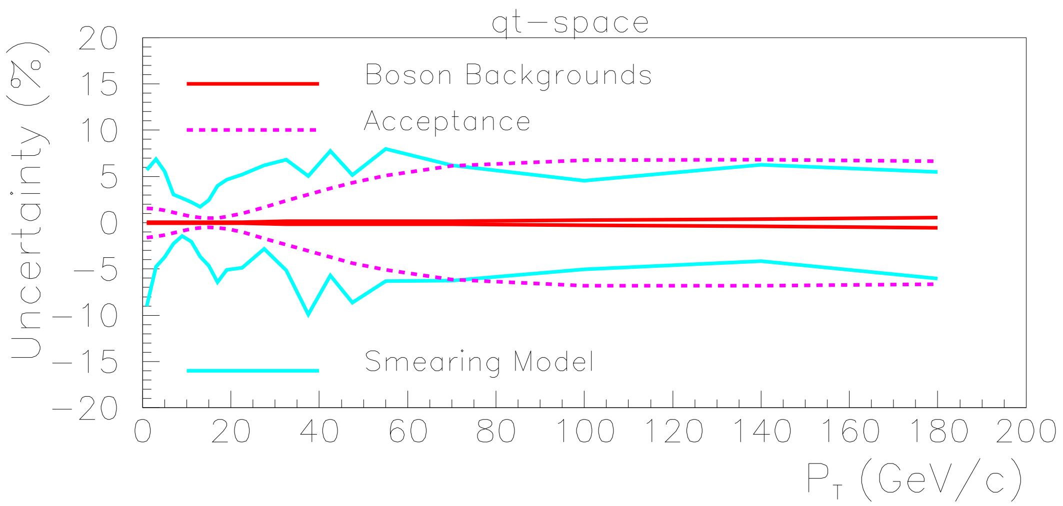

Figure 8.2: The systematic uncertainties for the re-shaped theoretical prediction (the q_T-space formalism). The uncertainties are from the boson background estimation, acceptance estimation, and smearing model.

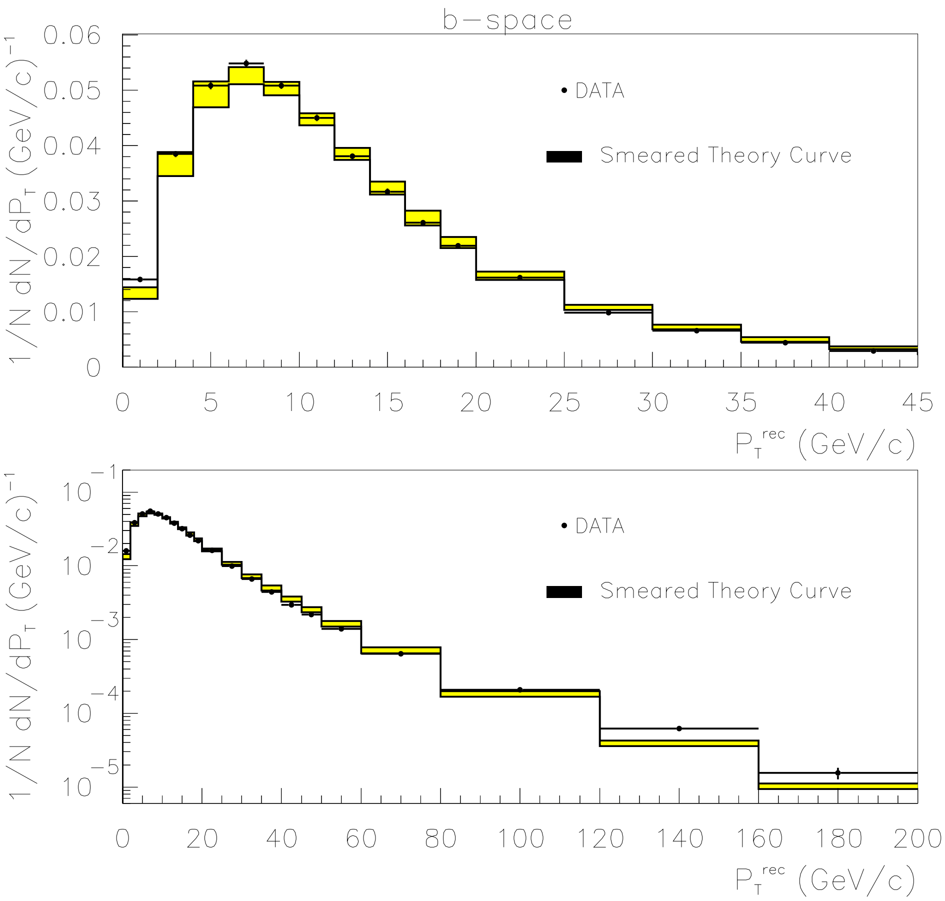

Figure 8.3: Comparison of the data and the smeared theory curve by the b-space formalism. The top figure shows P_T distribution in lower P_T region. The bottom shows the distribution up to $P_T = 200$ GeV/c in log scale. The systematic uncertainties from the single boson background estimation, the acceptance estimation, and the smearing model are shown as a band with the theory curve. The error bars of with data plots show the sum in quadrature of the statistical uncertainties and the systematic uncertainties from the QCD background estimation.

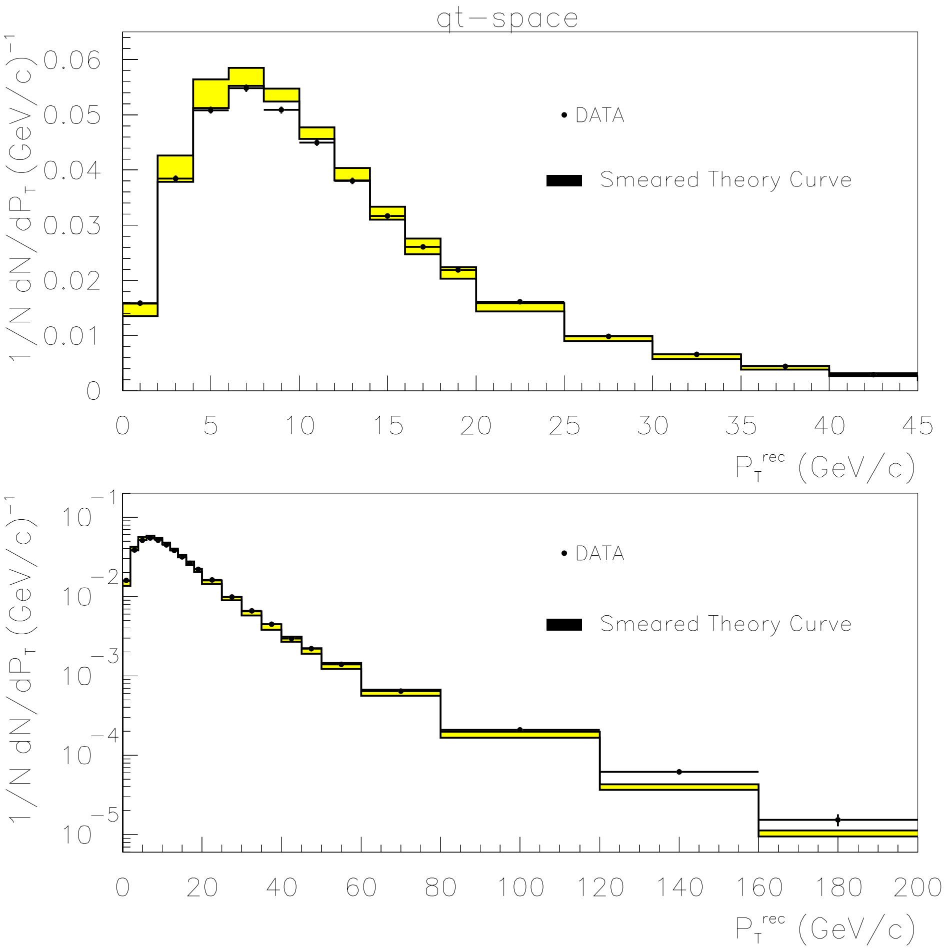

Figure 8.4: Comparison of the data and the smeared theory curve by the q_T-space formalism. The top figure shows P_T distribution in lower P_T region. The bottom shows the distribution up to $P_T = 200$ GeV/c in log scale. The systematic uncertainties from the single boson background estimation, the acceptance estimation, and the smearing model are shown as a band with the theory curve. The error bars with the data plots show the sum in quadrature of the statistical uncertainties and the systematic uncertainties from the QCD background estimation.

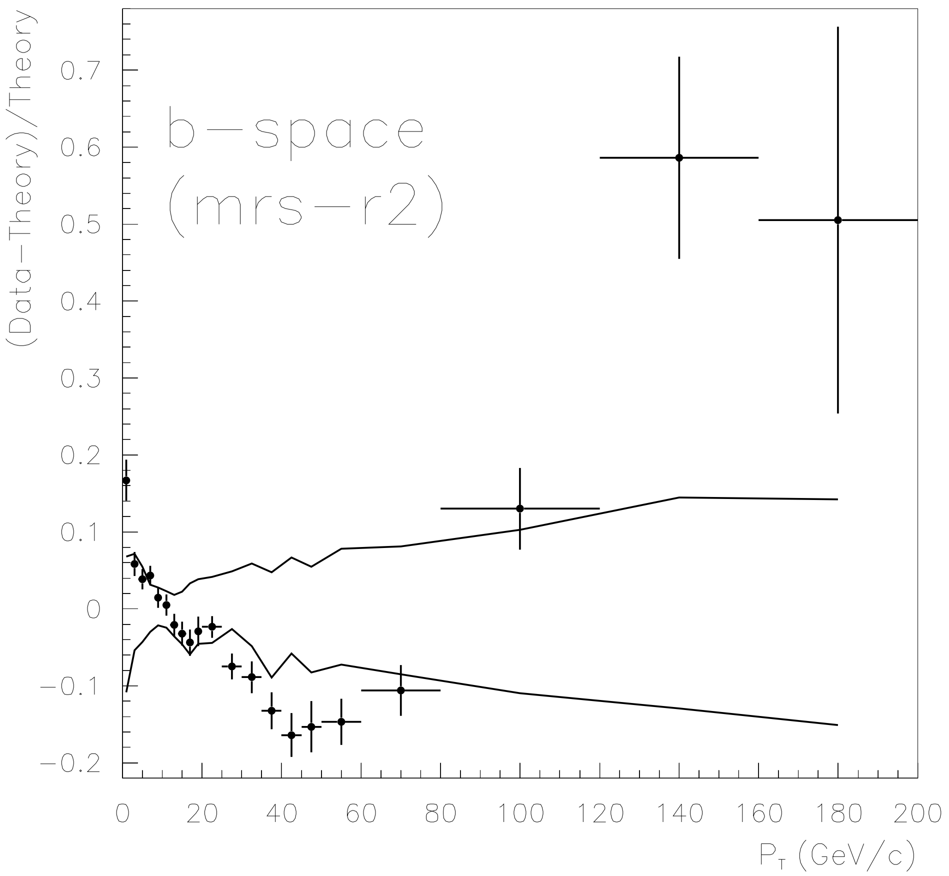

Figure 8.5: (Data-Theory)/Theory (b-space formalism). The error bars with the data plots are the statistical uncertainties. The systematic uncertainties from the QCD background estimation, the single boson background estimation, the acceptance estimation, and the smearing model are shown as a band.

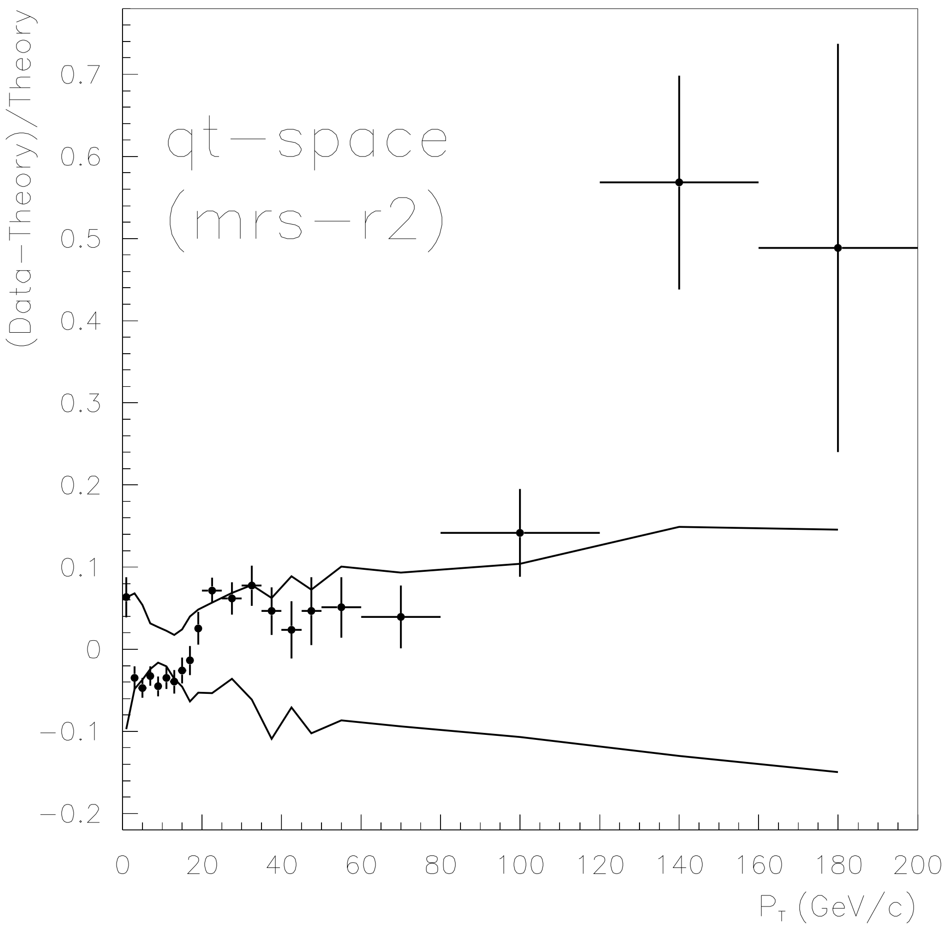

Figure 8.6: (Data-Theory)/Theory (q_T-space formalism). The error bars with the data plots are the statistical uncertainties. The systematic uncertainties from the QCD background estimation, the single boson background estimation, the acceptance estimation, and the smearing model are shown as a band.

Chapter 9

Conclusions

We have measured the W boson transverse momentum (P_T^W) distribution in $p\bar{p}$ collisions at $\sqrt{s} = 1.8$ TeV. The data corresponding to an integrated luminosity of 110 pb^{-1} were collected with the CDF detector during Run I from 1992 to 1995.

A total of 62165 $W \to e\nu$ candidate events are selected by requiring an isolated high E_T (≥ 25 GeV) electron in the central region ($|\eta| < 1.1$) and a large $\not{E}_T$ (≥ 25 GeV).

Residual backgrounds from QCD multijet events are subtracted from the W candidate events. The size and shape of these background events are estimated using independent QCD multijet samples. These background events are less than 1% of the W candidate events. The fraction of backgrounds from processes such as $W \to \tau\nu \to e\nu\nu\nu$ and $Z \to ee \to e$"ν" in the candidates are determined as a function of P_T^W, for which we use a Monte Carlo event generator. The fraction of the backgrounds from $W \to \tau\nu$ and $Z \to ee$ events is ~3% for $P_T^W < 50$ GeV/c and ~15% for $P_T^W > 140$ GeV/c.

The detector resolution on the P_T distribution of the recoil as a function of P_T^W is estimated, where we use the $Z \to ee$ events as a control sample.

We compare the data with the NLO plus gluon resummation (the b-space and q_T-space formalisms) predictions. The theory curves are re-shaped according to the boson backgrounds, the detector resolution, and the detector acceptance. The last item is studied using a Monte Carlo event generator.

We find that the NLO plus gluon resummation calculation provides reasonable description of the data in the range $P_T^W \lesssim 120$ GeV/c and that there appears to be a discrepancy at high P_T^W ($120 \lesssim P_T^W \lesssim 200$ GeV/c), though the experimental errors are large.

Appendix A

Monte Carlo Samples

We make Monte Carlo samples for the single boson backgrounds estimation (Chapter 5) and for the acceptance estimation (Chapter 6) with PYTHIA (version 5.7) [22]. We use the following switches.

Primordial $k_\perp$ distribution in hadron

- `MSTP(91)=2` : Exponential, width given in PARP(92), upper cut-off in PARP(93).
- `PARP(92)=1.25`
- `PARP(93)=10.0`

Process Mode

- `MSEL =12 (11)`: $W^\pm$ (Z^0) production in the range,
  - $P_T^{W/Z} < 35$ GeV/c : Background estimation,
  - $P_T^{W} < 15$ GeV/c : Acceptance estimation.
- `MSEL = 14 (13)`: $W^\pm$ (Z^0) + jet production in the range,
  - $P_T^{W/Z} \geq 35$ GeV/c : Background estimation,
  - $P_T^{W} \geq 15$ GeV/c : Acceptance estimation.

⋆ `MSTP(43)=2`: Z^0 only (no γ^* generated) for Z process.

Appendix B

The CDF Collaboration

F. Abe,[17] H. Akimoto,[39] A. Akopian,[31] M. G. Albrow,[7] A. Amadon,[5] S. R. Amendolia,[27] D. Amidei,[20] J. Antos,[33] S. Aota,[37] G. Apollinari,[31] T. Arisawa,[39] T. Asakawa,[37] W. Ashmanskas,[5] M. Atac,[7] P. Azzi-Bacchetta,[25] N. Bacchetta,[25] S. Bagdasarov,[31] M. W. Bailey,[22] P. de Barbaro,[30] A. Barbaro-Galtieri,[18] V. E. Barnes,[29] B. A. Barnett,[15] M. Barone,[9] G. Bauer,[19] T. Baumann,[11] F. Bedeschi,[27] S. Behrends,[3] S. Belforte,[27] G. Bellettini,[27] J. Bellinger,[40] D. Benjamin,[35] J. Bensinger,[3] A. Beretvas,[7] J. P. Berge,[7] J. Berryhill,[5] S. Bertolucci,[9] S. Bettelli,[27] B. Bevensee,[26] A. Bhatti,[31] K. Biery,[7] C. Bigongiari,[27] M. Binkley,[7] D. Bisello,[25] R. E. Blair,[1] C. Blocker,[3] K. Bloom,[20] S. Blusk,[30] A. Bodek,[30] W. Bokhari,[26] G. Bolla,[29] Y. Bonushkin,[4] D. Bortoletto,[29] J. Boudreau,[28] L. Breccia,[2] C. Bromberg,[21] N. Bruner,[22] R. Brunetti,[2] E. Buckley-Geer,[7] H. S. Budd,[30] K. Burkett,[11] G. Busetto,[25] A. Byon-Wagner,[7] K. L. Byrum,[1] M. Campbell,[20] A. Caner,[27] W. Carithers,[18] D. Carlsmith,[40] J. Cassada,[30] A. Castro,[25] D. Cauz,[36] A. Cerri,[27] P. S. Chang,[33] P. T. Chang,[33] H. Y. Chao,[33] J. Chapman,[20] M. -T. Cheng,[33] M. Chertok,[34] G. Chiarelli,[27] C. N. Chiou,[33] F. Chlebana,[7] L. Christofek,[13] R. Cropp,[14] M. L. Chu,[33] S. Cihangir,[7] A. G. Clark,[10] M. Cobal,[27] E. Cocca,[27] M. Contreras,[5] J. Conway,[32] J. Cooper,[7] M. Cordelli,[9] D. Costanzo,[27] C. Couyoumtzelis,[10] D. Cronin-Hennessy,[6] R. Culbertson,[5]

D. Dagenhart,[38] T. Daniels,[19] F. DeJongh,[7] S. Dell'Agnello,[9] M. Dell'Orso,[27] R. Demina,[7] L. Demortier,[31] M. Deninno,[2] P. F. Derwent,[7] T. Devlin,[32] J. R. Dittmann,[6] S. Donati,[27] J. Done,[34] T. Dorigo,[25] N. Eddy,[13] K. Einsweiler,[18] J. E. Elias,[7] R. Ely,[18] E. Engels, Jr.,[28] W. Erdmann,[7] D. Errede,[13] S. Errede,[13] Q. Fan,[30] R. G. Feild,[41] Z. Feng,[15] C. Ferretti,[27] I. Fiori,[2] B. Flaugher,[7] G. W. Foster,[7] M. Franklin,[11] J. Freeman,[7] J. Friedman,[19] H. Frisch,[5] Y. Fukui,[17] S. Gadomski,[14] S. Galeotti,[27] M. Gallinaro,[26] O. Ganel,[35] M. Garcia-Sciveres,[18] A. F. Garfinkel,[29] C. Gay,[41] S. Geer,[7] D. W. Gerdes,[20] P. Giannetti,[27] N. Giokaris,[31] P. Giromini,[9] G. Giusti,[27] M. Gold,[22] A. Gordon,[11] A. T. Goshaw,[6] Y. Gotra,[28] K. Goulianos,[31] H. Grassmann,[36] C. Green,[29] L. Groer,[32] C. Grosso-Pilcher,[5] G. Guillian,[20] J. Guimaraes da Costa,[15] R. S. Guo,[33] C. Haber,[18] E. Hafen,[19] S. R. Hahn,[7] R. Hamilton,[11] T. Handa,[12] R. Handler,[40] W. Hao,[35] F. Happacher,[9] K. Hara,[37] A. D. Hardman,[29] R. M. Harris,[7] F. Hartmann,[16] J. Hauser,[4] E. Hayashi,[37] J. Heinrich,[26] A. Heiss,[16] B. Hinrichsen,[14] K. D. Hoffman,[29] C. Holck,[26] R. Hollebeek,[26] L. Holloway,[13] Z. Huang,[20] B. T. Huffman,[28] R. Hughes,[23] J. Huston,[21] J. Huth,[11] H. Ikeda,[37] M. Incagli,[27] J. Incandela,[7] G. Introzzi,[27] J. Iwai,[39] Y. Iwata,[12] E. James,[20] H. Jensen,[7] U. Joshi,[7] E. Kajfasz,[25] H. Kambara,[10] T. Kamon,[34] T. Kaneko,[37] K. Karr,[38] H. Kasha,[41] Y. Kato,[24] T. A. Keaffaber,[29] K. Kelley,[19] R. D. Kennedy,[7] R. Kephart,[7] D. Kestenbaum,[11] D. Khazins,[6] T. Kikuchi,[37] M. Kirk,[3] B. J. Kim,[27] H. S. Kim,[14] S. H. Kim,[37] Y. K. Kim,[18] L. Kirsch,[3] S. Klimenko,[8] D. Knoblauch,[16] P. Koehn,[23] A. Köngeter,[16] K. Kondo,[37] J. Konigsberg,[8] K. Kordas,[14] A. Korytov,[8] E. Kovacs,[1] W. Kowald,[6] J. Kroll,[26] M. Kruse,[30] S. E. Kuhlmann,[1] E. Kuns,[32] K. Kurino,[12] T. Kuwabara,[37] A. T. Laasanen,[29] S. Lami,[27] S. Lammel,[7] J. I. Lamoureux,[3] M. Lancaster,[18] M. Lanzoni,[27] G. Latino,[27] T. LeCompte,[1] S. Leone,[27] J. D. Lewis,[7] M. Lindgren,[4] T. M. Liss,[13] J. B. Liu,[30] Y. C. Liu,[33]

N. Lockyer,[26] O. Long,[26] M. Loreti,[25] D. Lucchesi,[27] P. Lukens,[7] S. Lusin,[40] J. Lys,[18] K. Maeshima,[7] P. Maksimovic,[11] M. Mangano,[27] M. Mariotti,[25] J. P. Marriner,[7] G. Martignon,[25] A. Martin,[41] J. A. J. Matthews,[22] P. Mazzanti,[2] K. McFarland,[30] P. McIntyre,[34] P. Melese,[31] M. Menguzzato,[25] A. Menzione,[27] E. Meschi,[27] S. Metzler,[26] C. Miao,[20] T. Miao,[7] G. Michail,[11] R. Miller,[21] H. Minato,[37] S. Miscetti,[9] M. Mishina,[17] S. Miyashita,[37] N. Moggi,[27] E. Moore,[22] Y. Morita,[17] A. Mukherjee,[7] T. Muller,[16] A. Munar,[27] P. Murat,[27] S. Murgia,[21] M. Musy,[36] H. Nakada,[37] T. Nakaya,[5] I. Nakano,[12] C. Nelson,[7] D. Neuberger,[16] C. Newman-Holmes,[7] C.-Y. P. Ngan,[19] H. Niu,[3] L. Nodulman,[1] A. Nomerotski,[8] S. H. Oh,[6] T. Ohmoto,[12] T. Ohsugi,[12] R. Oishi,[37] M. Okabe,[37] T. Okusawa,[24] J. Olsen,[40] C. Pagliarone,[27] R. Paoletti,[27] V. Papadimitriou,[35] S. P. Pappas,[41] N. Parashar,[27] A. Parri,[9] D. Partos,[3] J. Patrick,[7] G. Pauletta,[36] M. Paulini,[18] A. Perazzo,[27] L. Pescara,[25] M. D. Peters,[18] T. J. Phillips,[6] G. Piacentino,[27] M. Pillai,[30] K. T. Pitts,[7] R. Plunkett,[7] A. Pompos,[29] L. Pondrom,[40] J. Proudfoot,[1] F. Ptohos,[11] G. Punzi,[27] K. Ragan,[14] D. Reher,[18] M. Reischl,[16] A. Ribon,[25] F. Rimondi,[2] L. Ristori,[27] W. J. Robertson,[6] A. Robinson,[14] T. Rodrigo,[27] S. Rolli,[38] L. Rosenson,[19] R. Roser,[13] T. Saab,[14] W. K. Sakumoto,[30] D. Saltzberg,[4] A. Sansoni,[9] L. Santi,[36] H. Sato,[37] P. Schlabach,[7] E. E. Schmidt,[7] M. P. Schmidt,[41] A. Scott,[4] A. Scribano,[27] S. Segler,[7] S. Seidel,[22] Y. Seiya,[37] F. Semeria,[2] T. Shah,[19] M. D. Shapiro,[18] N. M. Shaw,[29] P. F. Shepard,[28] T. Shibayama,[37] M. Shimojima,[37] M. Shochet,[5] J. Siegrist,[18] A. Sill,[35] P. Sinervo,[14] P. Singh,[13] K. Sliwa,[38] C. Smith,[15] F. D. Snider,[15] J. Spalding,[7] T. Speer,[10] P. Sphicas,[19] F. Spinella,[27] M. Spiropulu,[11] L. Spiegel,[7] L. Stanco,[25] J. Steele,[40] A. Stefanini,[27] R. Ströhmer,[7a] J. Strologas,[13] F. Strumia, [10] D. Stuart,[7] K. Sumorok,[19] J. Suzuki,[37] T. Suzuki,[37] T. Takahashi,[24] T. Takano,[24] R. Takashima,[12] K. Takikawa,[37] M. Tanaka,[37]

B. Tannenbaum,[4] F. Tartarelli,[27] W. Taylor,[14] M. Tecchio,[20] P. K. Teng,[33] Y. Teramoto,[24] K. Terashi,[37] S. Tether,[19] D. Theriot,[7] T. L. Thomas,[22] R. Thurman-Keup,[1] M. Timko,[38] P. Tipton,[30] A. Titov,[31] S. Tkaczyk,[7] D. Toback,[5] K. Tollefson,[30] A. Tollestrup,[7] H. Toyoda,[24] W. Trischuk,[14] J. F. de Troconiz,[11] S. Truitt,[20] J. Tseng,[19] N. Turini,[27] T. Uchida,[37] F. Ukegawa,[26] J. Valls,[32] S. C. van den Brink,[15] S. Vejcik, III,[20] G. Velev,[27] I. Volobouev,[18] R. Vidal,[7] R. Vilar,[7a] D. Vucinic,[19] R. G. Wagner,[1] R. L. Wagner,[7] J. Wahl,[5] N. B. Wallace,[27] A. M. Walsh,[32] C. Wang,[6] C. H. Wang,[33] M. J. Wang,[33] A. Warburton,[14] T. Watanabe,[37] T. Watts,[32] R. Webb,[34] C. Wei,[6] H. Wenzel,[16] W. C. Wester, III,[7] A. B. Wicklund,[1] E. Wicklund,[7] R. Wilkinson,[26] H. H. Williams,[26] P. Wilson,[7] B. L. Winer,[23] D. Winn,[20] D. Wolinski,[20] J. Wolinski,[21] S. Worm,[22] X. Wu,[10] J. Wyss,[27] A. Yagil,[7] W. Yao,[18] K. Yasuoka,[37] G. P. Yeh,[7] P. Yeh,[33] J. Yoh,[7] C. Yosef,[21] T. Yoshida,[24] I. Yu,[7] A. Zanetti,[36] F. Zetti,[27] and S. Zucchelli[2]

[1] *Argonne National Laboratory, Argonne, Illinois 60439*

[2] *Istituto Nazionale di Fisica Nucleare, University of Bologna, I-40127 Bologna, Italy*

[3] *Brandeis University, Waltham, Massachusetts 02254*

[4] *University of California at Los Angeles, Los Angeles, California 90024*

[5] *University of Chicago, Chicago, Illinois 60637*

[6] *Duke University, Durham, North Carolina 27708*

[7] *Fermi National Accelerator Laboratory, Batavia, Illinois 60510*

[8] *University of Florida, Gainesville, Florida 32611*

[9] *Laboratori Nazionali di Frascati, Istituto Nazionale di Fisica Nucleare, I-00044 Frascati, Italy*

[10] *University of Geneva, CH-1211 Geneva 4, Switzerland*

[11] *Harvard University, Cambridge, Massachusetts 02138*

[12] *Hiroshima University, Higashi-Hiroshima 724, Japan*

[13] *University of Illinois, Urbana, Illinois 61801*

[14] *Institute of Particle Physics, McGill University, Montreal H3A 2T8, and University of Toronto,*

Toronto M5S 1A7, Canada

[15] The Johns Hopkins University, Baltimore, Maryland 21218

[16] Institut für Experimentelle Kernphysik, Universität Karlsruhe, 76128 Karlsruhe, Germany

[17] National Laboratory for High Energy Physics (KEK), Tsukuba, Ibaraki 305, Japan

[18] Ernest Orlando Lawrence Berkeley National Laboratory, Berkeley, California 94720

[19] Massachusetts Institute of Technology, Cambridge, Massachusetts 02139

[20] University of Michigan, Ann Arbor, Michigan 48109

[21] Michigan State University, East Lansing, Michigan 48824

[22] University of New Mexico, Albuquerque, New Mexico 87131

[23] The Ohio State University, Columbus, Ohio 43210

[24] Osaka City University, Osaka 588, Japan

[25] Universita di Padova, Istituto Nazionale di Fisica Nucleare, Sezione di Padova, I-35131 Padova, Italy

[26] University of Pennsylvania, Philadelphia, Pennsylvania 19104

[27] Istituto Nazionale di Fisica Nucleare, University and Scuola Normale Superiore of Pisa, I-56100 Pisa, Italy

[28] University of Pittsburgh, Pittsburgh, Pennsylvania 15260

[29] Purdue University, West Lafayette, Indiana 47907

[30] University of Rochester, Rochester, New York 14627

[31] Rockefeller University, New York, New York 10021

[32] Rutgers University, Piscataway, New Jersey 08855

[33] Academia Sinica, Taipei, Taiwan 11530, Republic of China

[34] Texas A&M University, College Station, Texas 77843

[35] Texas Tech University, Lubbock, Texas 79409

[36] Istituto Nazionale di Fisica Nucleare, University of Trieste/ Udine, Italy

[37] University of Tsukuba, Tsukuba, Ibaraki 305, Japan

[38] Tufts University, Medford, Massachusetts 02155

[39] Waseda University, Tokyo 169, Japan

[40] *University of Wisconsin, Madison, Wisconsin 53706*

[41] *Yale University, New Haven, Connecticut 06520*

Bibliography

[1] F. Abe, *et al.*, Phys. Rev. Lett. **79**, 4760 (1997).

[2] R.K. Ellis, W. J. Stirling and B.R. Webber, *QCD and Collider Physics*, Cambridge University Press, (1996)

[3] P. Arnold and M.H. Reno, Nucl. Phys. **B319**,37 (1989).

[4] J. Collins and D. Soper, Nucl. Phys. **B193** 381, (1981); Erratum **B213** 545 (1983), **B197** 446 (1982).

[5] J. Collins, D. Soper, G. Sterman, Nucl Phys. **B250** 199 (1985).

[6] P.B. Arnold and R.P. Kauffman, Nucl. Phys. **B349** 381 (1991).

[7] G.A. Ladinsky and C.-P. Yuan, Phys. Rev. **D50** 4239 (1994).

[8] R.K. Ellis and S. Veseli, Nucl. Phys. **B511**, 649 (1998).

[9] A.D. Martin, R.G. Roberts and W.J. Stirling, Phys. lett. **B387**, 419, 1996.

[10] C. Albajar *et al.* (UA1 Collaboration), Z. Phys. **C44**, 15 (1989)

[11] J. Alitti *et al.*, (UA2 Collaboration), Z. Phys. **C47**, 523 (1990).

[12] F. Abe *et al.*, Phys. Rev. Lett. **66**, 2951 (1991).

[13] B. Abbott *et al.*, (DØ Collaboration), Phys. Rev. Lett. **80**, 5498 (1998).

[14] F. Abe *et al.* (CDF collaboration), Nucl. Instr. and Meth. **A271** (1988) 387.

[15] K. Yasuoka *et al.*, Nucl. Instr. and Meth. **A267** (1988) 315.

[16] F. Abe *et al.*, Phys. Rev. **D45**, 1448 (1992).

[17] B. Flaugher, *New Jet Correction Function QDJSCO 2.0*, CDF internal note 1513.

[18] N. Eddy, *New Relative Jet Corrections for Run 1A and Run 1B Data*, CDF internal note 3534.

[19] D. Cronin-Hennessy *et all.*, *The Missing Transverse Energy Correction*, CDF internal note 4085.

[20] R.G. Wagner *et al.*, *The Missing E_T correction for the Run 1 $W/Z+\gamma$ Analysis*, CDF internal note 4193.

[21] D. Cronin-Hennessy. *QCD Backgrounds to $W+\geq n$ Jets*, CDF internal note 4087.

[22] T. Sjostrand, *PYTHIA 5.7 and JETSET 7.4: Physics and Manual*, Comput. Phys. Commun., (1995).

[23] E. Barberio and Z Was, *" PHOTOS - A universal Monte Carlo for QED radiative corrections: version 2.0"*, Comput. Phys. Commun. **79**, 291 (1994).

[24] M. Shaprio *et al.*, *"A User's Guide to QFL"*, CDF internal note 1810.

[25] *"The Review of Particle Physics"*, Phys. Rev. **D54**, 1 (1996).

[26] F. Abe *et al.*, Phys. Rev. **D52**, 2624 (1995).

[27] H.L. Lai *et al.*, Phys. Rev. **D55**, 1280 (1997).

[28] A.D. Martin, R.G. Roberts, W.J. Stirling, Phys. Lett. **B354**, 155 (1995)

[29] B. L. Winer, *The W Boson Transverse Momentum Spectrum in Proton-Antiproton Collisions at* $\sqrt{s} = 1.8$ *TeV*, Ph. D. Thesis, Lawrence Berkeley Laboratory, (1991)